Visualisation of Chemistry in Flow

by

Jan Novak

A thesis submitted to
The University of Birmingham
For the degree of
DOCTOR OF PHILOSOPHY

School of Chemistry
College of Engineering and Physical Sciences
The University of Birmingham
July 2010

Abstract

This research project investigated the pattern-producing Belousov-Zhabotinsky (BZ) reaction under flow using a combination of optical and magnetic resonance (MRI) imaging techniques. The coupling between reaction-diffusion and advection was studied in three distinct systems.

Stationary flow-distributed oscillation (FDO) patterns, previously only observed in packed bed reactors, were produced in alternative flow fields for the first time. The two systems studied have allowed greater insight into the structure, dynamics and stability of the patterns. Plug-like flow was produced with an agar gelling agent and in a vortex flow reactor (VFR). The agar system allowed the production of FDO patterns in the absence of a packing material and could be forced by a periodic change in reaction temperature. Synchronisation was found in space-time but not time. This was in contrast to previous investigations, where periodic illumination resulted in the observation of synchronous behaviour. The VFR provided a flow field which was able to produce stationary and travelling patterns. The complex structure of the stationary bands was explained by the flow, in which Taylor vortices translate axially up the tube in an approximation of plug flow. The rotation rate of the inner cylinder was identified as a new parameter for control of both the stability and wavelength of FDO patterns.

Optical imaging was able to probe the bulk behaviour of propagating waves through three-dimensional Taylor vortices but was unable to probe the wave propagation mechanisms. It was found however, that magnetic resonance imaging was able to visualise the behaviour of the chemical waves within the Couette cell in order to elucidate the wave behaviour. In conjunction with this MR velocity and diffusion imaging were able to characterise the flow within the Taylor vortices. The combination of these two methods uniquely allowed the behaviour of these travelling waves to be explained in terms of the flow within the system.

For Mom and Dad

Acknowledgements

First and foremost I would like to thank my supervisor Melanie Britton, who gave me the opportunity for this research. I would also like to thank her for the constant support and advice throughout the course of my PhD.

I would like to thank my parents for their supporting both financially and emotionally through my undergraduate degree, enabling me to study towards this point, not to mention their continued support to this day.

The work in this thesis has also been greatly aided by the help of our collaborators: Mark Wilson, Barnaby Thompson and Annette Taylor.

I would like to thank everyone past and present in the Britton group for all the fun times had during the course of my PhD. Dan, Nicola, Heather, and Andre and all made my time at Birmingham a fruitful and enjoyable experience. A special thanks must go to Antoine Vallatos for the insightful conversations with regards to the work in this thesis. I would like to thank everyone from the second and fourth floors over the past four years, apologies if I have missed anyone: Bene, Bav, Jean-Louis, Tom, Andy B, Andy L, Ad, Christina, Simon, Kousik, Smale, Sarah T, Claire, Emma, Oliver, Graham, Maryjane, Ian, Roy, Josephine, Trevor, Johanna, Lasse, Shamim, Sarah H, Fabrice and Jackie. I would like to thank the support staff at the university including Steve the glassblower, Tony, Neil and Stuart whose tireless work have made the experiments conducted in this thesis possible. I would also like to thanks Andy Sederman for the velocity imaging sequence. Last, but not least, I would like to thank my fiancé Hannah who has supported me throughout my PhD.

List of Figures

List of Abbreviations

AOT – aerosol OT (sodium bis(2–ethylyhexyl) sulfosuccinate)

BZ – Belousov-Zhabotinsky

CPMG – Carr-Purcell-Meiboom-Gill

CSTR – Continuously-Stirred Tank Reactor

FDO – Flow-Distributed Oscillations

FDS – Flow-Distributed Structures

FID – Free Induction Decay

FKN – Field-Körös-Noyes

MR(I) – Magnetic Resonance (Imaging)

NMR – Nuclear Magnetic Resonance

PGSE – Pulse Gradient Spin Echo

RARE – Rapid Acquisition with Relaxation Enhancement

RDA – Reaction-Diffusion-Advection

r.f. – radiofrequency

TV – Taylor Vortices

T_1IR – T_1 Inversion Recovery

VFR – Vortex Flow Reactor

Contents

1. Chapter 1 Introduction

1.1. Introduction to Chemical Patterns

Self-organised patterns are found throughout the natural world[1]. Examples include: electrical impulses that control the beating of the heart[2], tiger stripes[1], plankton blooms in the ocean[3] and spiral galaxies[4]. The Belousov-Zhabotinsky (BZ) reaction[5] is a man-made system which under various experimental conditions has been shown to produce a wide range of patterns. Although the underlying mechanisms may differ, patterns in the BZ reaction have been compared to those found in nature. The motivation for studying reactions of this type is provided not only by the desire to understand the mechanisms behind the chemical process, but to further understand the immensely complicated pattern-producing processes in nature.

1.2. Non-Linear Chemistry

1.2.1. Feedback and Autocatalysis

Chemical reactions that show oscillatory and pattern-producing behaviour will tend to exhibit some sort of feedback in their kinetics. Chemical feedback is defined as: the concentration of a species affects the production rate of the species. Positive feedback occurs when an increase in concentration of a species, increases it's rate of production. A schematic representation example of quadratic autocatalysis (positive feedback) is shown in eq 1.1. In this example, the reaction between the species A and B produces two species B.

$$A + B \rightarrow 2B \qquad \text{(eq 1.1)}$$

A classic example of autocatalysis is the Landolt Clock Reaction[6]. In this reaction there is a long induction period followed by a rapid acceleration of the reaction rate. Clock reactions reach equilibrium shortly after the rapid increase in the reaction rate. The resetting of a clock reaction can induce oscillatory behaviour.

Oscillatory reactions and their pattern-producing properties have been the subject of many research papers, conferences and textbooks. A brief overview of the underlying principles will be outlined here. For a more in-depth analysis please refer to one of the recommended textbooks[6, 7].

1.2.2. History of the Belousov-Zhabotinsky Reaction

The original observation of oscillations in a chemical reaction was made by Boris Belousov[8]. Belousov was a biochemist in search of an analogue of the Krebs cycle[9], which forms part of the respiratory process in cells. For this purpose he used a combination of acidified bromate, citric acid and cerium ions. It was noted that over the period of an hour, there was a periodic change in colour from yellow to colourless, while simultaneously producing carbon dioxide. He proceeded to study this reaction with vigour, investigating the effect of temperature and acidity on the period of the oscillations. Attempts to publish his findings were rebuked, with referees citing the impossibility of the observations. The only publication of this work

by Belousov was an obscure symposium abstract in 1959, up to nine years after the first discovery of the reaction[10].

In 1964, Anatol M. Zhabotinsky published an analysis of Belousov's reaction[11], replacing citric acid with malonic acid and replacing the cerium catalyst with iron-containing ferroin. These changes were key, allowing clearer observation of the longer-lasting oscillations. This reaction, now known as the Belousov-Zhabotinsky reaction, has spawned it's own diverse and interesting field. The tragedy of this story is that Belousov never received the recognition for his endeavours. In 1970, ten years after Belousov's death, he was jointly awarded the Lenin prize, along with Zhabotinsky, V. I. Krinsky and G. R. Ivansky in recognition of the importance of his discovery. A full written account of this story was written by A. T. Winfree[12].

1.2.3. Mechanism of the Belousov-Zhabotinsky Reaction

The chemical makeup of the Belousov-Zhabotinsky reaction prior to the onset of oscillations is relatively simple. The system consists of an aqueous solution of bromate ions, sulphuric acid, malonic acid and a metal, or metal-containing catalyst (e.g. iron-containing ferroin). The mechanism of the BZ reaction is highly complex involving at least 30 different chemical species. It can, however, be understood in terms of the Field-Körös-Noyes (FKN) mechanism, which is a simplified mechanistic representation of the reaction[13]. The FKN mechanism divides the reaction into 6 steps (not included here), which are in turn, compiled into 3 processes. This breakdown allows the oscillatory nature of the reaction to be easily explained.

$BrO_3^- + 2Br^- + 3H^+ \rightarrow 3HOBr$ Process A

Process A is the induction period, during which Br^- ions are removed. The Br^- is the inhibitor species in the BZ reaction. This initial induction period is the stage prior to the onset of oscillations.

$BrO_3^- + HBrO_2 + 2M_{red} + 3H^+ \rightarrow 2HBrO_2 + 2M_{ox} + H_2O$ Process B

Process B is the feedback step, which is triggered at a critically low concentration of Br^-. Key to process B is the activator species ($HBrO_2$). Process B involves the production of two $HBrO_2$ molecules from an initial one. The actual steps involved are much more complex but the overall stoichiometry shows autocatalysis. The metal catalyst is also oxidised in process B. The metal oxidation is not only essential for the mechanism, it is also important for observation of oscillations in the system, which is addressed in more detail below.

Together, processes A and B combine to produce a clock reaction. An additional step to reset the clock results in a reaction that can oscillate between two states. To reset the reaction, the following conditions need to be met: (i) Br^- concentration needs to increase to a level high enough to switch the positive feedback process off and (ii) the metal catalyst is reduced back to the original state.

$2M_{ox} + MA + BrMA \rightarrow fBr^- + 2M_{red}$ + other products Process C

Process C is the negative feedback step, which resets the clock. The stoichiometric factor, f, is used for modelling the reaction and can be varied depending on the sophistication of the study[6]. After process C, process A once again takes over and the cycle repeats. This chain of events can occur many times until the system reaches an equilibrium state.

1.2.4. Chemical Pattern Formation

As well as exhibiting oscillatory behaviour in a well-stirred batch reactor, the BZ reaction can produce spatial oscillations, i.e. chemical patterns. In general, among other reasons, chemical reactions are well stirred to minimise chemical concentration gradients. If a reacting solution is unstirred, however, localised regions of chemical inhomogeneity arise. In reactions that exhibit autocatalytic behaviour, the localised regions of different chemical composition can become reaction hotspots or excitation points. At these points, production of autocatalytic species can massively increase. The autocatalytic species can then be transported from this excitation point to another region by diffusive processes. The combination of chemical and diffusive processes results in a spatial spread of the reaction (reaction-diffusion systems).

In a clock reaction, the coupling of the autocatalysis and diffusion results in a chemical front, which propagates from the excitation point. This front propagates through the solution until the reaction solution has been completely consumed by the final products, i.e. chemical equilibrium. The propagation velocity of the reaction front is determined by both the chemical reaction rate and the magnitude of the diffusion.

Excitation points form in oscillatory reactions in exactly the same way as clock reactions. The chemistry in an oscillatory reaction, however, produces a different spatially-resolved chemical concentration profile. For example, in the BZ reaction, Process C facilitates the return to a pre-oscillation state which is translated to the chemical front. The front no longer consumes the reaction vessel but has a finite width due to the return to the pre-oscillation state. This spatial structure is referred to as a chemical wave. There is a sharp leading front to the wave with a slow return to the pre-oscillation state. The solution through which the reaction wave propagated then enters a refractory period and cannot immediately oscillate again. From a single excitation point, multiple waves can be produced.

When an oscillatory reaction such as the BZ reaction is placed in a two-dimensional reactor, such as a Petri dish, a rich variety of patterns can be observed from multiple excitation points. An example of patterns produced by the BZ reaction in a Petri dish is shown in Figure 1.1[7, 14].

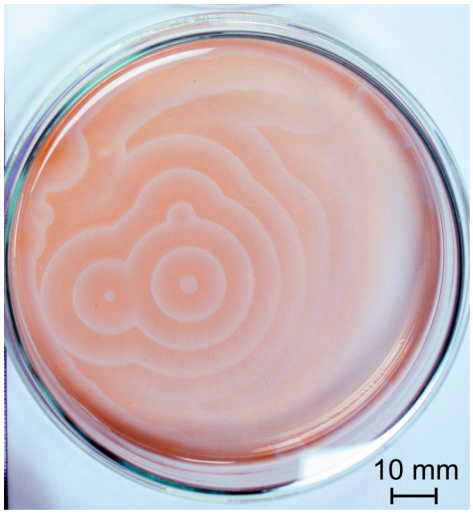

Figure 1.1 Optical image showing patterns formed by the ferroin-catalysed Belousov-Zhabotinsky reaction in a Petri dish. The blue and red regions indicate the presence of Fe^{3+} and Fe^{2+} respectively.

1.2.4.1. Stationary Patterns

Alan Turing [15] first proposed the potential existence of stationary patterns in a reaction-diffusion system in his 1952 paper entitled 'The Chemical Basis of Morphogenesis'. Turing was a mathematician who developed an interest in biological processes. In order to further understand the process of morphogenesis, he described a system which could produce stationary patterns from an initially homogeneous chemical system. The system hypothesised by Turing was very simple, consisting of an activator (autocatalytic) and an inhibitor species. In Turing's system the activator and inhibitor species diffuse at different rates through the reaction medium. Specifically, the inhibitor must diffuse more rapidly that the activator. The range of influence of the species differs significantly with the diffusivity. The activator and inhibitor then dominate distinct spatial regions, producing stationary patterns.

Turing patterns were first experimentally realised by De Kepper and colleagues in 1990 using the CIMA reaction[16]. Another system has been developed recently using a microemulsion made with water, octane and a surfactant (AOT)[17]. Stationary concentration patterns have also been produced via a non-Turing mechanism under flow. These patterns have been termed flow-distributed oscillations[18], and will be explained below.

1.2.5. Measurements of Chemical Oscillations and Patterns

A variety of methods can be employed to measure and visualise both the oscillations and patterns produced in the BZ reaction. A brief summary of the relevant methods for this thesis will be provided below. All of the investigations in the following chapters use the metal catalyst, either directly or indirectly to indicate chemical oscillations. Other methods have been employed previously for which a more in depth analysis can be found in one of the referenced textbooks[6, 7].

1.2.5.1. Potentiometric Methods

Oscillations in the well-stirred BZ reaction are commonly measured using potentiometry. This involves measuring the potential difference of the reacting solution using a Pt-combination electrode. This method can follow the changes in oxidative state of the metal catalyst, against a reference, over time. An example of a potentiometric experiment is shown in Figure 1.2, which follows oscillations in the ferroin-catalysed BZ reaction.

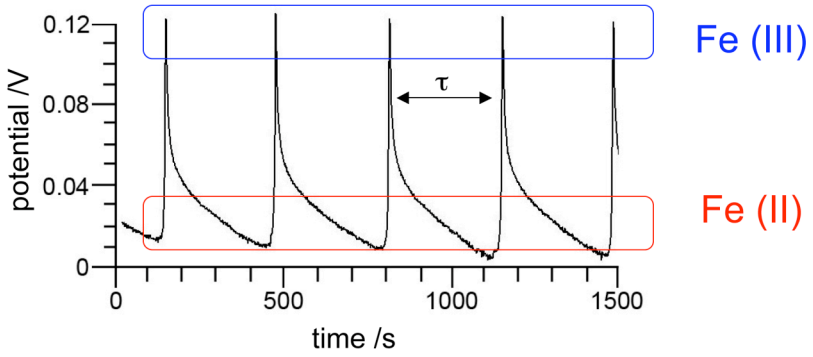

Figure 1.2 A plot showing temporal oscillations in the ferroin-catalysed Belousov-Zhabotinsky reaction observed over time using a Pt-combination electrode. The periodic increase in potential indicates a switch from red Fe^{2+} to blue Fe^{3+}. τ is the period between oscillations.

Two key parameters can be extracted from the potentiometric measurements of the oscillations in Figure 1.2. The period between oscillations, τ, is given by the time between peaks. The amplitude of the oscillation peaks indicates the conversion ratio between the two oxidation states of the metal catalyst.

1.2.5.2. Optical Methods

If the metal catalyst exhibits a colour change between the two oxidation states, optical methods can be used to follow both oscillations and patterns in the BZ reaction. This can be achieved directly[5] or indirectly via spectrophotometric measurements[19]. It was Belousov who first noticed the oscillations in the BZ reaction using cerium as a catalyst/indicator[8]. However, the Ce^{3+}(colourless)/Ce^{4+}(yellow) redox couple has relatively poor colour contrast. Ferroin is widely used as the catalyst for the BZ reaction

when employing optical methods. This is due to the excellent colour contrast between the two oxidation states[5], in which the metal centre in ferroin switches between ferroin (Fe^{2+}) which is deep red colour to ferriin (Fe^{3+}) which is vivid blue. Another catalyst commonly used is $Ru(bipy)_3$ (green/orange colour change) but the optical contrast is inferior when compared to ferroin.

1.2.5.3. Magnetic Resonance Methods

Hansen and Rouff[20], and more recently Binks[21], have shown that oscillations in the BZ reaction can be monitored by NMR techniques. In both studies, the relaxation times of excited protons were used to monitor the chemical oscillations. Magnetic resonance imaging techniques have been exploited for visualisation of patterns in the BZ reaction[22-30]. These techniques allow measurements of three dimensional and optically opaque systems. A more comprehensive review of the techniques involved will be given below.

1.3. Synchronisation

Pattern-producing systems, such as those studied in this thesis, have previously been subjected to external forcing parameters such as light[31] and temperature. Recently, there has been increased interest in the coupling between non-linear chemical oscillators and imposed external oscillators to induce synchronous behaviour[32]. Synchronous behaviour has been studied in numerous biological and physical science systems. The phenomenon is observed in situations as varied as the menstruation cycles of groups of

females[33], electronics[34] and the rhythmic clapping of hands in a round of applause[35]. A brief description of the relevant areas of the field will be given here. For further information the text by Pikovsky, Rosenblum and Kurths is highly recommended[36].

Synchronisation is defined as the adjustment of the rhythm of two oscillators due to a weak interaction. It is important that the interaction between the two oscillators is weak; a strong interaction would result in one oscillator driving the other. A historically significant example of synchronisation between oscillators is two pendulums supported by a common beam, which was the first reported occurrence of the behaviour by Christiaan Huygens[37]. A schematic diagram of the experiment is shown in Figure 1.3. This figure shows how the motion of two pendulums couple through the motion (vibrational or motional) of the common supporting beam. This common beam allows the frequency at which the two pendulums move to be locked (i.e. they move at the same rate). In conjunction with the frequency locking, the phase of the pendulums can also be locked (i.e. they are moving in the same direction). Figure 1.3 (a) shows two pendulums that are synchronised in phase and (b) shows two pendulums synchronised out of phase.

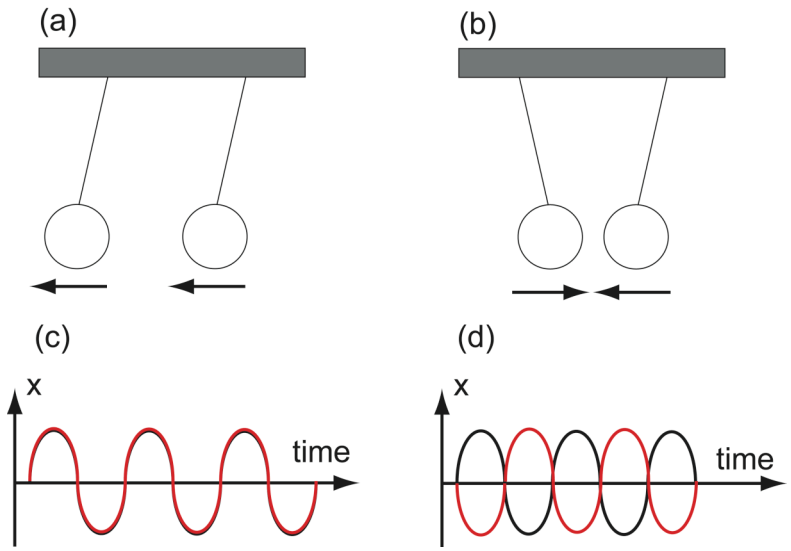

Figure 1.3 Schematic diagram showing synchronisation of two frequency-locked pendulums attached to a common beam. (a) shows the motion of two pendulums in phase and (b) shows the motion of two pendulums out of phase. (c) and (d) are the space-time plots for (a) and (b) respectively.

The coupling between pendulums is a simple example of the synchronisation of two periodic oscillators. Another type of synchronisation can occur when a periodic oscillator can be influenced by an external periodic force. This type of relationship is unidirectional as only one of the oscillators is influential over the other. An example of this is biological clocks that govern the circadian rhythm of cells in organisms. Petrov *et al*.[38] have harnessed this principle to periodically force the light sensitive BZ reaction by illumination. They found that the periodicity of the forcing parameter dramatically changed the period of the reaction and hence the pattern formation.

A Lissajous[32] plot is a graphical representation of the observable oscillator vs. external force. This can provide an insight into both the phase and frequency relationship between the oscillators. If the frequencies of the

oscillators are locked, the diagram will be a closed loop as shown in Figure 1.4. If the frequencies are not locked, given enough time, the diagram would fill the entire plot. The phase shift between the synchronous pair also be analysed by the Lissajous plot. Figure 1.4 (a) shows a pair almost in phase and (b) shows a pair in perfect anti-phase. An oscillating pair perfectly in phase results in a Lissajous plot that reduces to a single line

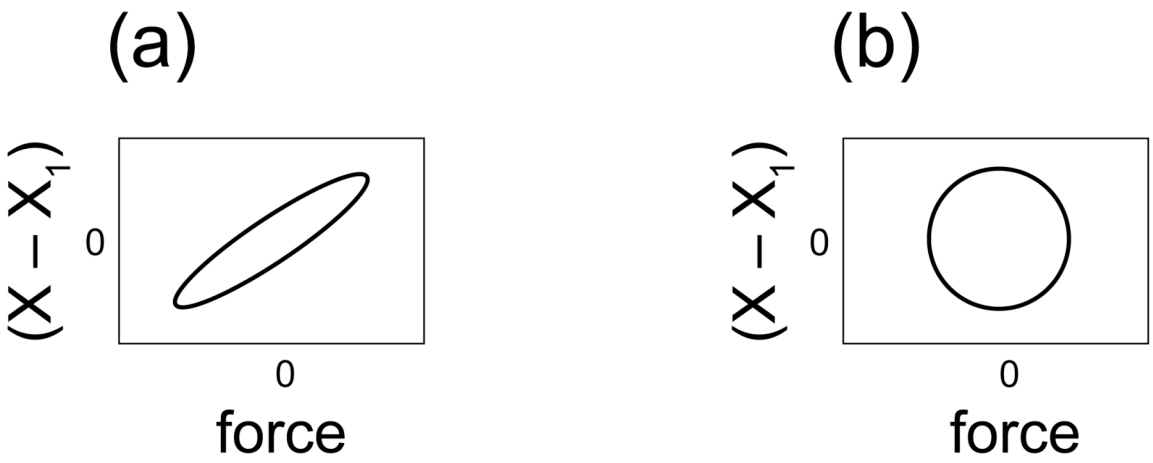

Figure 1.4 Lissajous plots of two frequency locked oscillators that are coupled and the phase shift is constant. (a) The behaviour of two oscillators that are almost in phase. (b) The behaviour of two oscillators that are out of phase.

1.4. Non-linear Chemical Systems Under Flow

Section 1.2.4 discussed the coupling of reaction and diffusion to produce both stationary and travelling waves in oscillatory chemical systems. The complexity of these systems can be further enhanced when coupled to flow. Under the influence of flow, these reactions are referred to as reaction-diffusion-advection (RDA) systems. RDA systems are of particular interest due to the shared similarities with biological and ecological systems. RDA

systems vary from the segmentation of cells during morphogenesis[39], to plankton blooms transported by vortex flow in the ocean[3]. The aerial picture shown in Figure 1.5 shows a plankton bloom being transported by vortex flow in the ocean.

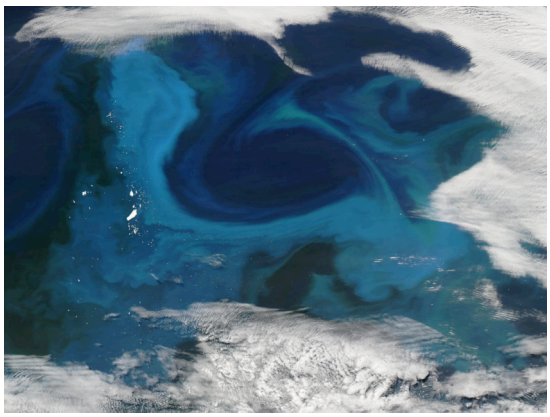

Figure 1.5 An aerial photograph showing a phytoplanckton bloom in the Southern Ocean taken from a NASA satellite[40].

1.4.1. Flow-Distributed Oscillations

Flow-distributed oscillations (FDO), sometimes referred to as flow-distributed structures (FDS) are a specific example of an RDA system. This system was first postulated by Kuznetsov[41] and subsequently proven experimentally by Kaern and Menzinger[18]. FDO patterns provide an alternative mechanism for the formation of stationary chemical patterns to Turing patterns. Unlike Turing patterns, FDOs do not require a difference in diffusivity of the reactants.

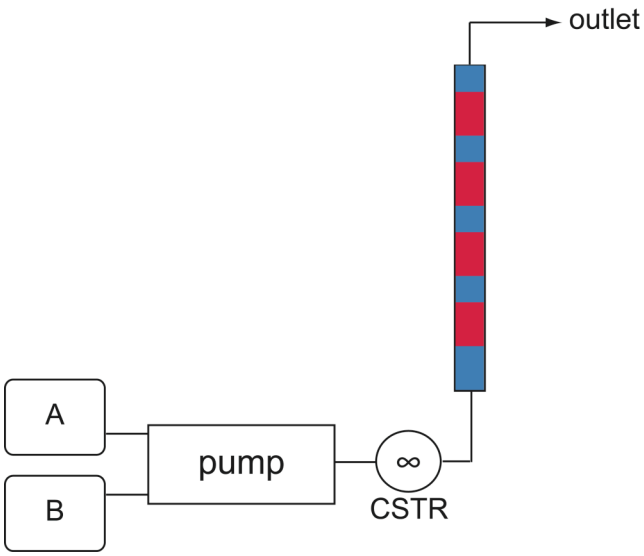

Figure 1.6 Schematic diagram showing the experimental setup used for the production of FDO patterns. Stock solutions A and B are pumped into a CSTR and passed via capillary into a plug flow reactor. This example shows the ferroin-catalysed BZ reaction which switches between a red a blue colour.

The experimental setup for the formation of the FDO patterns is shown in Figure 1.6. The BZ reactants were separated into two stock solutions, which allowed the reaction to occur only upon mixing. These stock solutions are pumped into a continuously-stirred tank reactor (CSTR) with a small volume. The homogenised reaction solution is then rapidly transported to the reaction tube. Once in the tube, the reactants flow up the tube, forming chemical concentration bands. A number of conditions permit the formation of stationary FDO patterns:

(i) The chemical system used for the production of the patterns needs to oscillate in a well-stirred closed system.

(ii) The reaction needs have a constantly-forced boundary condition (i.e. the reaction must be permanently in the same phase when entering the reaction tube). Experimentally, this is achieved by a small

CSTR and fast transport of the reaction mixture from the CSTR to the reaction tube. Failure to meet this condition results in travelling waves

(iii) The flow within the reaction tube needs to adopt a plug flow profile. A plug flow profile is where the velocity of a fluid is constant across the width of a pipe shown in Figure 1.7 (b). Plug flow is markedly different to the flow profile of a Newtonian liquid, such as water passing through a pipe, which adopts a Poiseuille flow profile (Figure 1.7(a)). Plug flow ensures that the phase of the reaction is uniform across the annulus of the reactor.

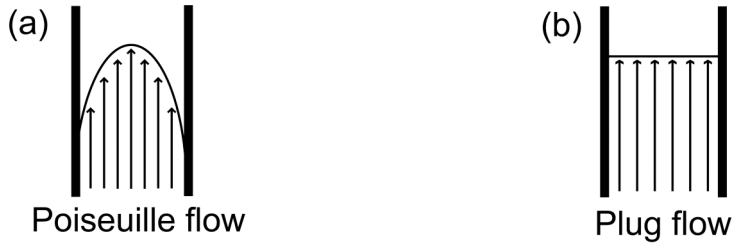

Figure 1.7 Schematic diagram showing velocities of fluid though a pipe for a Poiseuille flow profile and (b) plug flow through a pipe.

Kaern and Menzinger[18] previously used a kinematic description to describe the pattern-producing behaviour of the FDO patterns. This model describes a spatial distribution of temporal oscillations through the reaction tube. This results in a system whereby temporal oscillations can be observed through space. Using this kinematic description, the wavelength of the stationary FDO patterns can be described by eq 1.2, where λ is the wavelength, τ is the period between oscillations and v is the linear velocity of the fluid.

$$\lambda = v\tau \qquad \text{(eq 1.2)}$$

A schematic representation of the formation of stationary FDO patterns is shown in Figure 1.8. The fluid packet, p1 can be followed through the reaction tube. The packet enters the tube in one state of the reaction, displayed as red. The third time frame shows that p1 has switched to the other state (blue). The fourth time frame shows a return to the red state for p1. This behaviour continues as the fluid packet travels up the reaction tube. All of the fluid packets switch state at the same point within the reaction tube, resulting in stationary bands.

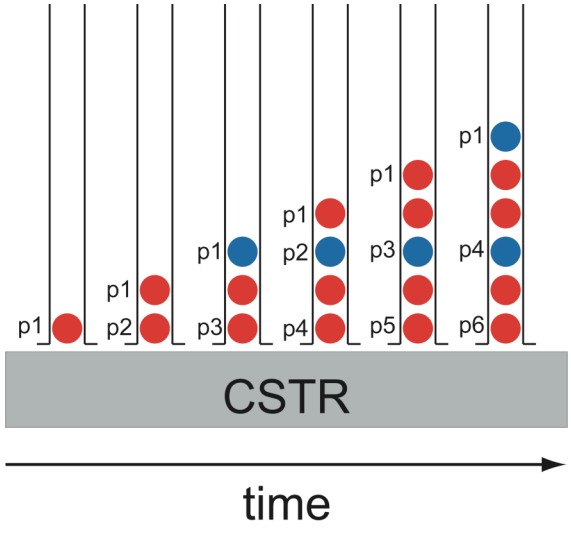

Figure 1.8 Schematic diagram to show the formation of stationary FDO patterns as the tube fills with reactants. The diagram shows the reaction tube with 6 frames at sequential time points. The red and blue spheres represent fluid packets in two different reaction states.

The method used by Kaern and Menzinger to describe stationary FDO patterns is useful but inherently flawed[42]. It has been shown, both

theoretically[42] and experimentally[43], that the model breaks down at the lowest fluid flow rates. . A rich variety of non-stationary patterns have been observed at these lower flow rates where the diffusive transport is comparable to flow within the system[43]. The model also fails to describe the initial formation of experimentally-produced FDO patterns.

Diffusion effects in the reaction tube can result in the mixing of adjacent fluid packets. This mixing induces a modulation of the steady state position of the FDO patterns. This modulation in the position of patterns is not described by eq 1.2

The formation of FDO patterns occurs via a mechanism termed wavesplitting[44]. Wavesplitting involves the formation of an excitation point from which the chemical bands propagate. The position of the excitation point is predicted by eq 1.2[44]. A band is produced at this excitation point which elongates and then splits into two distinct waves. One wave travels up, propelled by the flow, out of the reaction tube. The other wave propagates downwards, to settle at a stationary position slightly below the predicted wavelength. This discrepancy is accounted for by the diffusive mixing between adjacent fluid packets, not included in eq 1.3. The model used by Kaern and Menzinger cannot describe the wavesplitting. In this simple model, the settling wave would be travelling backwards in time[44].

All of the previous experimental studies of stationary FDO patterns have taken place in a packed bed reactor (PBR)[18, 30, 43-48]. An example of FDO patterns produced in a packed bed reactor is shown in Figure 1.9.

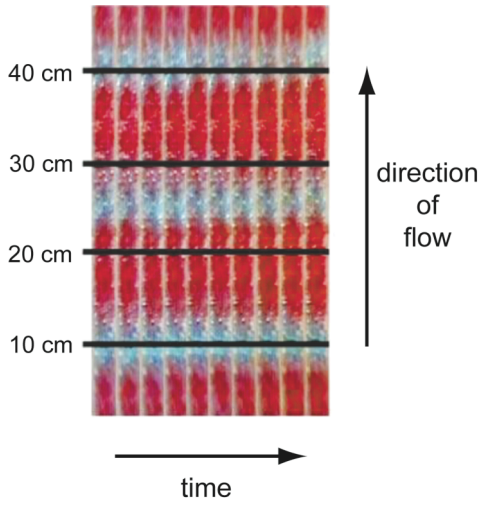

Figure 1.9 A series of optical images showing FDO patterns produced using the ferroin-catalysed BZ reaction pumped through a packed bed reactor. The figure is taken from the paper: Scaling and dynamics in 'flow distributed oscillation patterns' in the Belousov-Zhabotinsky reaction by Bamforth *et al.* [44]. The figure has been reproduced with the permission of the Royal Society of Chemistry.

A PBR is a tubular reactor with packing material (e.g. glass beads) throughout the bore. PBRs promote plug flow by breaking up the Poiseuille flow normally associated with Newtonian fluid flow through a pipe reactor. However NMR velocity imaging [30, 49, 50] has shown the flow to consist of a combination of fast-flowing channels and stagnant pockets. When the FDO patterns are produced in PBR, the flow may alter the observed chemistry. The stagnant pockets have the potential to oscillate independently and, through diffusion, alter the wavelength of the patterns. The fast-flowing channels also have the potential to alter the wavelength by increasing axial mixing between fluid packets.

Most of the investigations into flow-distributed oscillations use optical measurements to observe the temporal behaviour of the patterns. Optical imaging provides only a topographical view of the reaction tube with no insight into the three-dimensional structure. This problem was overcome by Britton *et al*.[30], who used magnetic resonance imaging (MRI) to investigate FDO patterns produced with the Mn-catalysed BZ reaction in a PBR. MRI allowed the three-dimensional structure of the FDO patterns to be imaged. They showed that the patterns had a canonical shape, which was not obvious from the previous investigations using optical imaging. The shape was then related to NMR fluid velocity measurements within the PBR. The methodology involved in both the chemical wave and velocity imaging is described below.

1.4.2. Propagation of Travelling Waves Through Vortices

Reaction-diffusion-advection systems have not been limited to the investigation of FDO patterns in PBRs. A number of other systems have been studied including front propagation in Poiseuille[51] and turbulent flows[52]. Solomon's group have extensively studied the propagation of chemical waves through vortex flows[53-56] using optical imaging. Similar experiments have also been conducted by Pocheau and Harambat[57] using a clock reaction to produce fronts. The investigated vortex flow is created using magnetohydrodynamic methods[57]. A thin layer of high ionic strength solution is used to create the vortices which also has a potential passed across it to make it more magnetically susceptible. The vortex flow is induced by a series of magnets rotating beneath the solution layer. An example of the experiments conducted by Solomon is shown in Figure 1.10[55]. In this figure,

the $Ru(bipy)_3$ catalysed BZ reaction is initiated and allowed to propagate through the linear array of vortices. The reaction waves were transported around the perimeter of the vortex cell by the circular fluid motion. The wave is transported to the next cell by diffusion across the boundary (there is minimal flow between vortex pairs). The boundary is known as the separatrix. This process continues with a reaction wave passing through the vortex cell from left to right in the figure.

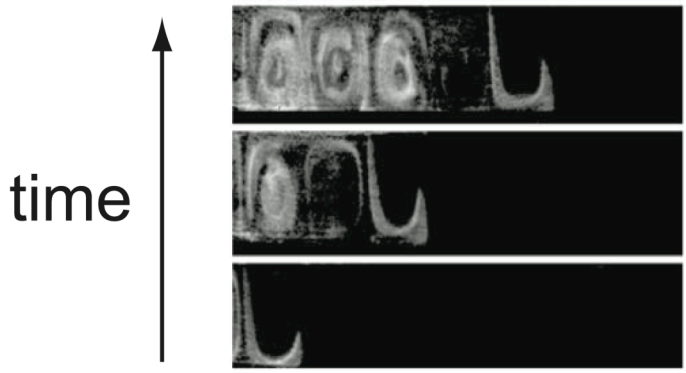

Figure 1.10 A series of optical images showing propagation of the $Ru(bipy)_3$-catalysed BZ reaction waves through a chain of vortices[55]. The $Ru(bipy)_3$-catalysed system has the advantage that the chemistry can be controlled by light so the reaction can be inhibited and initiated by illumination.

Analysis of this system has shown synchronisation between the rotation of the fluid and the natural period of the chemical waves[54]. Solomon showed that the number of vortex turns can be locked to the number of vortices through which the chemical waves propagate (mode-locking). The vortex setup has also been extended to two dimensions by using arrays of magnets beneath the solution[58]. In doing so, two-dimensional structures such as propagating waves and spirals have been observed.

The experiments showed that non-linear chemistry can propagate through a chain of vortices. The experiments are limited, however, to pseudo two-dimensional systems. Pocheau and Harambat, for example, used a fluid depth of 3 mm. The system also has the potential passed across it, which affects the dynamics of the BZ pattern formation[59]. The study by Pocheau and Harambat discussed the effect of the current on the front propagation[57]. They showed that the front velocity is modulated by the increased current density necessary for the creation of the vortex flow.

1.4.2.1. Couette Flow

Taylor vortices, produced in a cylindrical Couette cell, provide an alternative method of producing vortices without the need for magnetohydrodynamic methods. A diagram of the couette cell setup is shown in Figure 1.11. The cell consists of an outer cylinder (with an inner radius, r_o) with an inner cylinder (outer radius r_i) within it. In between these two cylinders (the annulus) is the fluid. For this study, only the inner cylinder will be rotated and the outer cylinder will remain stationary.

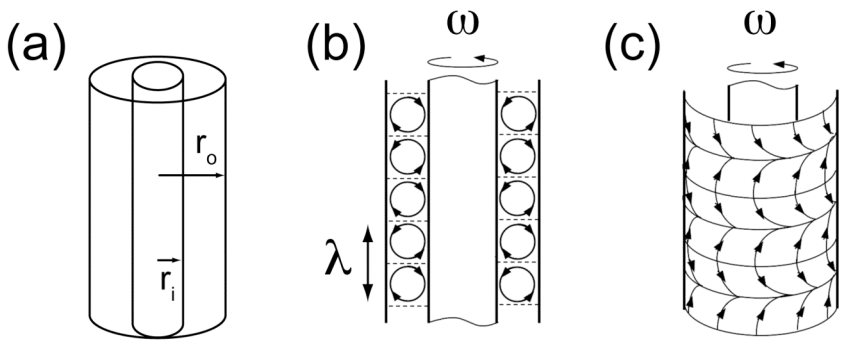

Figure 1.11 Schematic diagram of Taylor-Couette apparatus. (a) is the Couette cell where ω is the rotation rate, r_i is the radius of the inner cylinder and r_o is the inner radius of the outer cylinder. (b) Shows a two-dimensional representation of the Taylor vortices where λ is the wavelength of a pair of vortices. (c) Shows the shape of the torroidal vortices in three-dimensions.

The Couette flow system was first developed for the study of viscous fluids under shear. At low rotation speeds, the fluid in the Couette cell annulus follows normal laminar flow with the fastest fluid flow found at the inner cylinder and the lowest velocity found at the outer cylinder[60]. It is, however, at higher inner rotation rates where the Taylor-Couette flow becomes interesting[61]. Above a certain critical inner rotation rate, instability-induced patterns appear throughout the Couette cell. In the first instance, the patterns take the form of pairs of torroidal laminar-flow counter-rotating vortices stacked along the length of the Couette cell as shown in Figure 1.11 (a) and (b). Further types of instabilities are observed at higher inner rotation rates[1] but are beyond the scope of this thesis.

1.4.2.2. Vortex Flow Reactors

The addition of axial flow to the Couette cell increases the complexity of the pattern-producing behaviour[62]. This type of reactor has been termed a vortex flow reactor (VFR). Different flow regimes such as helical vortex flow have been observed. For this study, only laminar Taylor vortex flow will be investigated. The extended range of flow patterns has been reported elsewhere[63-65]. The superimposed axial fluid motion stabilises the flow instabilities[66]. This stabilisation increases the critical rotation rate required for the formation of Taylor vortices.

When the VFR is in the laminar Taylor vortex regime, the torroidal vortex pairs can drift upwards in an approximation of a plug flow[67]. The vortices are forced to translate up the tube by the axial flow. This particular flow pattern is referred to as progressive Taylor vortices (PTV)[62].

There is still open debate in the literature about the exact nature of this flow field. It was assumed by Kataoka[67] that the linear velocity (v) of fluid and the drift velocity (v_d) of the Taylor vortices were equal for a fairly large range of experimental parameters. This has subsequently been proven to be an over-simplification and regimes where the drift velocity of the vortices is both faster[68] ($v_d > v$) and slower[69] ($v_d < v$) have been shown. For the case where $v_d < v$, the position of the vortices was seen to be stabilised, resulting in them moving slower than the linear velocity. For this to happen, the fluid must be transported either through or around the vortices. The majority of models produced for this flow system have assumed a by-pass flow where the fluid is transported around the vortices but this mechanism has not been experimentally proven. This by-pass flow represents a deviation from plug

flow because the axial mixing is increased. Additionally, for an approximation of plug-like flow to be maintained in a VFR, the flow must remain in the steady vortex regime. In the subsequent wavy vortex regime, inter-vortex mixing is too high to approximate plug flow[70, 71].

Giordano *et al*.[69, 72] showed at either end of the VFR the flow is altered by the boundary conditions. The vortices at the inlet were shown to be larger due to the inflow of the fluid. Equally, the vortices at the top of the reactor were shown to be smaller due to the outflow of the fluid.

The wavelength of the vortices has been shown to be dependent on the rotation rate of the inner cylinder. Lueptow[62] reported a decrease in the wavelength for increased rotation rates of the inner cylinder, which was explained by a compression of vortices within a pair. For this, the separatrix between the pairs become larger but the overall wavelength of the vortex pairs is reduced.

The secondary flow in VFRs has been harnessed for industrial applications[69], such as polymerisation reactions where a less destructive stirring method is desirable.

1.5. Magnetic Resonance

Magnetic resonance in a chemical context is usually associated with structural determination of molecules using spectroscopy. In conjunction with this magnetic resonance imaging (MRI) is used primarily as a medical diagnosis tool. However, MRI is also used throughout the physical sciences. Chemical engineers use MRI velocity measurements to observe hydrodynamics in flow reactors[73, 74], and oil companies use MRI to image rock formations in order to deduce viability of drilling sites[75]. More recently, MR methods have been used to investigate non-linear chemistry and pattern formation with and without flow[29, 30, 48, 76-78].

1.5.1. Theory

A brief outline of the basic theory behind of NMR and MRI will be given here, for a more in depth discussion please refer to the excellent textbooks on the subject[79-81]. A fundamental property of a magnetic nucleus is spin, I. This is a property of an element and is determined by the number of unpaired nucleons. Spin can therefore be an integer or half integer. An atom with spin I, has an angular momentum, J, defined in eq 1.3 were h is Planck's constant.

$$J = \frac{\{I(I+1)\}^{1/2}\mathrm{h}}{2\pi} \qquad \text{(eq 1.3)}$$

For an atom with spin I, there are $2I$+1 possible orientations relative to an axis. For example, ^{1}H has spin 1/2 and can therefore adopt two possible

orientations. The proton will be the only nucleus considered for this study. The two spin states (m = 1/2 and m = –1/2) in the proton are degenerate, i.e. have the same energies. This degeneracy is removed, however, when the nucleus is placed in a magnetic field. This is due to an interaction between the magnetic moments and the imposed field. It is this splitting of the energy states that makes NMR experiments possible. When placed in a strong magnetic field, the two spin states of a proton are orientated along the direction of the field, $\boldsymbol{B_0}$. Figure 1.12 shows the splitting of degenerate orbitals in a magnetic field. The difference in populations of the two energy levels is extremely small at thermal equilibrium and is given by the Boltzman distribution[82]. The magnitude of the splitting, ΔE, is given in eq 1.4 where γ is the gyromagnetic ratio of the particular nucleus.

.

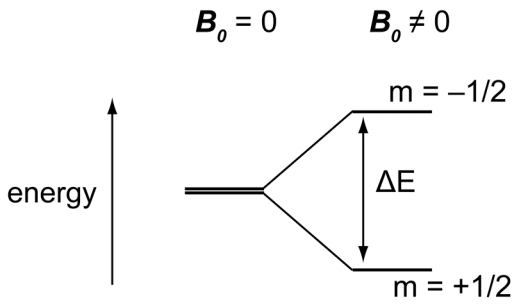

Figure 1.12 Energy level diagram showing the splitting of degenerate ^{1}H orbitals in a magnetic field.

$$\Delta E = \frac{\gamma \boldsymbol{B_0} h}{2\pi} \qquad \text{(eq 1.4)}$$

The spins precess about the direction of the magnetic field due to a torque exerted on the magnetic moment by the $\boldsymbol{B_0}$ field. Precession occurs at the Larmor frequency, ω (eq 1.5 and Figure 1.13).

$$\omega = \frac{\gamma \boldsymbol{B}}{2\pi} \qquad \text{(eq 1.5)}$$

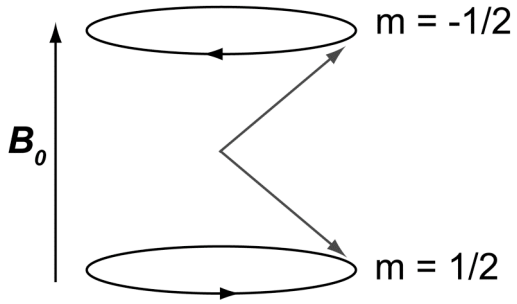

Figure 1.13 Schematic diagram of Larmor precession about magnetic field $\boldsymbol{B_0}$.

NMR experiments observe the behaviour of multiple nuclear spins. The summation of the spin vectors within a sample is referred to as the bulk magnetisation vector, **M**.

1.5.2. Radio Frequency Pulses

Signal in NMR experiments occurs when **M** precesses orthogonally to the magnetic field. The precession results in an oscillating current produced in the receiver coils. For this to occur, **M** needs to be manipulated. This is achieved by the application of radiofrequency (r.f.) pulses, which induces a

transition between spin states. The degree to which the magnetisation is deflected (tip angle, θ) is dependent on the amplitude and duration of the r.f. pulse. The simplest example of this manipulation is an orthogonal 90˚ pulse that rotates the vector into the *xy*-plane. A 90˚ r.f. pulse in the *y*-direction will rotate the bulk magnetisation vector from the *z*-axis to the *x*-axis as shown in Figure 1.14. The vector then precesses at the Larmor frequency in the *xy*-plane, producing a free induction decay (FID). The FID signal reduces over time due to spin relaxation processes explained below. A Fourier transform of the FID to produces a spectrum.

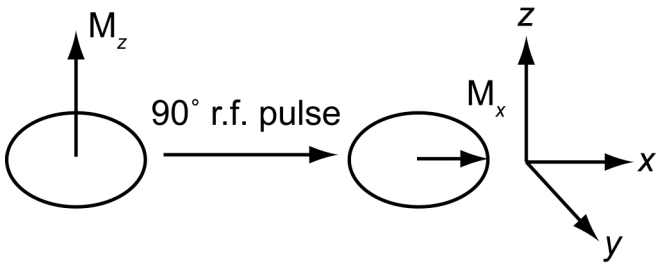

Figure 1.14 Schematic diagram showing a 90˚ r.f pulse rotating the bulk magnetisation vector, **M**, from the *z*-axis to the *xy* plane.

At equilibrium, the **M** resides along the magnetic field and is called the equilibrium magnetisation vector, $\mathbf{M_0}$.

1.5.3. The Rotating Frame of Reference

A rotating reference frame is a useful tool when describing the behaviour of spins in the *xy*-plane. The reference frame rotates at the Larmor frequency. When this is the case, the system is referred to as on-resonance, which allows deviations from the Larmor frequency to be easily explained.

The rotating frame of reference is particularly useful when describing T_2 relaxation in section 1.5.4.2.

1.5.4. Spin Relaxation

1.5.4.1. T_1 Relaxation

After a 90° pulse, the bulk magnetisation vector resides in the *xy*-plane. The return of the vector to the equilibrium value, $\mathbf{M_0}$ is referred to as T_1 relaxation, where T_1 is the time constant. The rate of T_1 relaxation is dependent on local fluctuations in the magnetic field. The most important contribution to the local magnetic field, with regards to T_1 relaxation, is dipolar coupling. If spins within a sphere of influence oscillate at the Larmor frequency, radiationless transitions between spin states can occur. These effects facilitate the return to thermal equilibrium. T_1 relaxation is an exponential decay process described by eq 1.6.

$$\mathbf{M_z} = \mathbf{M_0}(1 - e^{(-t/T_1)}) \qquad \text{(eq 1.6)}$$

Measurement of T_1 relaxation times can be achieved using an inversion recovery experiment. The pulse sequence for the inversion recovery experiment is shown in Figure 1.15. In the experiment the bulk magnetisation vector is inverted by the 180° pulse so that it resides along the negative *z*-axis. After a time delay, τ, some of the magnetization has reverted to the positive *z*-axis. Following τ, a 90° pulse rotates the magnetisation onto the *y*-axis. The resulting (FID) is then recorded, which is Fourier transformed to

produce a spectrum. Peak intensities from this spectrum are proportional to $\mathbf{M_z}$. The experiment is repeated at multiple τ values with the resulting intensity decay fitted to eq 1.6 to give the time constant T_1.

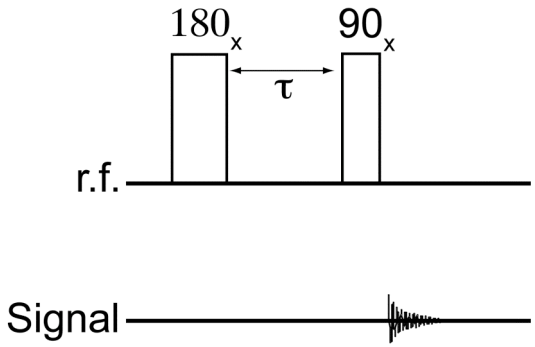

Figure 1.15 Schematic diagram of the pulse sequence for a T_1 inversion recovery experiment.

1.5.4.2. T_2 Relaxation

T_2 or spin-spin, is the relaxation of spins in the transverse plane. This occurs when spins lose phase coherence in the *xy*-plane (some move faster and some move slower than the Larmor frequency). Following a 90˚ pulse, the bulk magnetisation vector resides in the *xy*-plane with all spins precessing at the Larmor frequency. The phase coherency can only be maintained if all spins experience exactly the same magnetic field. Local magnetic fields of varying strength will induce a range of precession frequencies, removing phase coherence. This loss in phase coherence is an exponential process described by eq 1.7.

$$\mathbf{M}_{x,y} = \mathbf{M}_0 e^{(-t/T_2)} \qquad \text{(eq 1.7)}$$

Spin echoes can be used for the measurement of transverse relaxation[83]. The pulse sequence for the Hahn experiment is shown in Figure 1.16 (a), and the behaviour of **M** is shown in Figure 1.16 (b). A 90˚ r.f. pulse is used to rotate the spins into the *xy*-plane. The spins begin to dephase due to localised inhomogeneous magnetic fields, some precessing faster and some slower. After time, τ, the spins are inverted by a 180˚ r.f. pulse. The spins then rotate within the rotating frame in the opposite direction. Because of this, the spins rephase and regain the previously lost phase coherence. The time delay between the 90˚ and the 180˚ pulse is incrementally increased with the decay of the echo intensity fitted to eq 1.7.

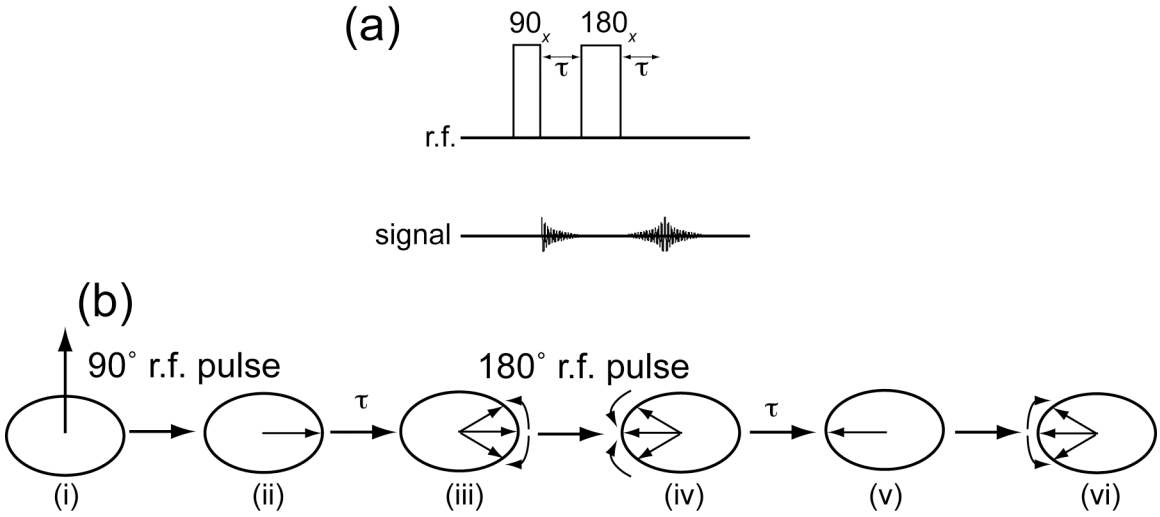

Figure 1.16 Schematic diagram showing (a) A spin echo pulse sequence (b) The manipulation of the spins during a Hahn echo pulse sequence[83]. (i)-(ii) A 90˚ pulse rotates the bulk magnetisation vector into the *xy*-plane. (iii) The spins begin to lose phase coherency. (iv) A 180˚ pulse 'flips' the spins, which begin to refocus as shown in (v). (vi) shows the spins beginning to, once again, lose phase coherency.

The spin echo experiment is, however, sensitive to magnetic field inhomogeneities. If spins diffuse to a region with a slightly different magnetic field, they cannot be fully refocused by the 180° pulse. As a result, T_2* is measured instead of T_2. T_2* is the measured relaxation time in the presence of significant local field inhomogeneities, resulting in a significantly shorter relaxation time than the real T_2. This behaviour is explained by eq 1.8.

$$\frac{1}{T_2^*} = \frac{1}{T_{2(\Delta B_0)}} + \frac{1}{T_2} \qquad \text{(eq. 1.8)}$$

For measurements of T_2 as opposed to T_2*, the spins need to be refocused on a timescale where diffusion effects are minimal. The Carr-Purcell-Meiboom-Gill (CPMG) experiment[83, 84] (Figure 1.17) repeats the 180° pulse *n* times, acquiring an echo each time and then fitting the decay of the echoes to eq 1.7 to obtain T_2.

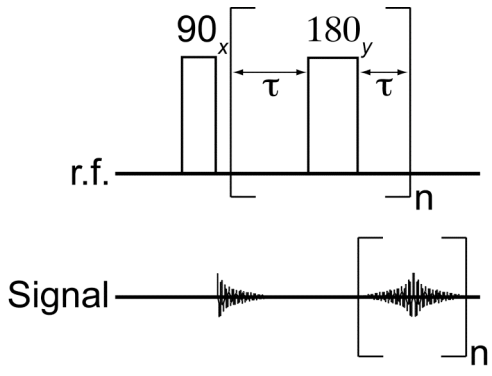

Figure 1.17 Schematic diagram showing the Carr-Purcell-Meiboom-Gill (CPMG) pulse sequence. The pulse sequence is based on the Hahn echo experiment with the 180° pulse repeated n times with n echoes acquired.

1.5.5. Magnetic Resonance Imaging

To produce an image, the NMR signal needs to be made spatially dependent. This is achieved by using magnetic field gradients. The gradients are produced by coils through which a current is passed to induce precise local magnetic field. The magnetic field gradient strengths in the *x*, *y* and *z* directions are given by eq 1.9 - 1.11.

$$\boldsymbol{G}_x = \frac{\mathrm{d}\boldsymbol{B}_z}{\mathrm{d}x} \qquad \text{(eq 1.9)}$$

$$\boldsymbol{G}_y = \frac{\mathrm{d}\boldsymbol{B}_z}{\mathrm{d}y} \qquad \text{(eq 1.10)}$$

$$\boldsymbol{G}_z = \frac{\mathrm{d}\boldsymbol{B}_z}{\mathrm{d}z} \qquad \text{(eq 1.11)}$$

By applying the magnetic field gradient, the Larmor frequency at position $\boldsymbol{r}$, becomes dependent on $\boldsymbol{G}$. eq 1.2, where $\boldsymbol{G}$ is the pulsed field gradient component parallel to $\boldsymbol{B_0}$.

$$\omega(\boldsymbol{r}) = \gamma \boldsymbol{B_0} + \gamma \boldsymbol{G} \bullet \boldsymbol{r} \qquad \text{(eq 1.12)}$$

The region that now has a position-dependent frequency contains multiple spins and is referred to as a spin packet. Gradients can also be applied in two and three directions for two and three-dimensional imaging respectively. The application of gradients result in an attenuation of the signal; for this reason imaging experiments generally use echoes. This is due to twice as much signal produced in for an echo compared to an FID.

1.5.5.1. Frequency and Phase Encoding

Two methods are typically used to encode the spatial information in MRI: frequency and phase encoding. As mentioned above, when a gradient is applied, the signal has a position-dependent frequency. Frequency encoding involves a gradient which is switched on during an acquisition and the signal is acquired at fixed time intervals. The data is then Fourier transformed producing a spatially dependent intensity plot using eq 1.9. The signal intensity is proportional to the number of spins at a particular frequency. For a one-dimensional frequency encoded experiment, a one-dimensional profile of signal intensity is produced. An example of frequency encoding of two tubes of water is shown in Figure 1.18.

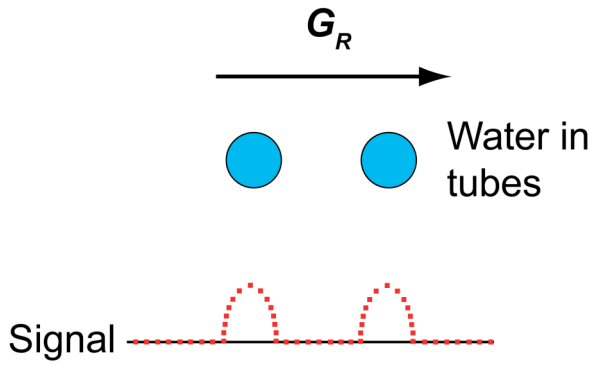

Figure 1.18 Schematic diagram showing a one-dimensional frequency-encoded imaging of two tubes of water.

Phase encoding uses a gradient pulse, which is switched, on then off, prior to signal acquisition. As the magnetic field gradients are applied linearly across the chosen axis, a helix of phase is wound (Figure 1.19). The spins are 'released' by switching the gradients off before the acquisition, giving them

a position-dependent phase. These two methods can be used in conjunction to produce two and three-dimensional images.

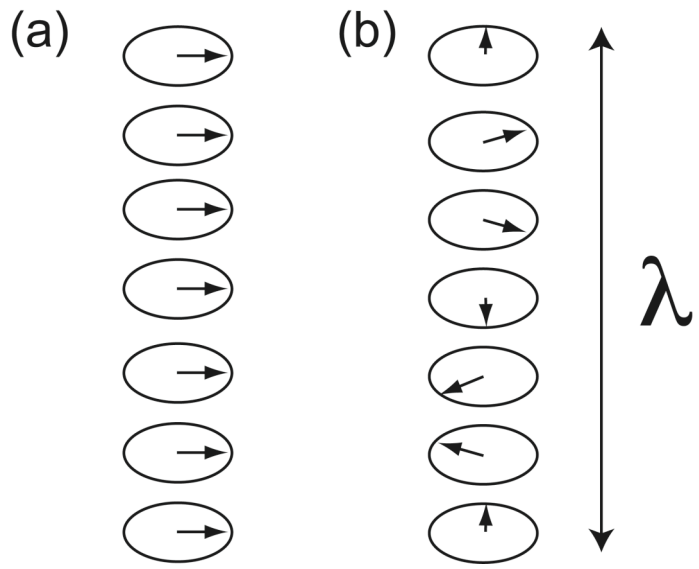

Figure 1.19 Schematic diagram showing the phase of spin packets following a 90˚ pulse; (a) No applied magnetic field gradient, all spin packets are in phase, (b) A magnetic field gradient has been applied to the system inducing a position-dependent helix of phase. λ is the wavelength of the helix of phase.

1.5.5.2. Slice Selection

Two-dimensional MR images are produced using a technique termed slice selection. Slice selection is the excitation of a two-dimensional plane through a sample using a frequency-selective soft r.f. pulse. The bandwidth of frequencies excited by an r.f. pulse is inversely proportional to the duration of that pulse. A soft pulse is one of long duration that excites a narrow band of frequencies. Gradients can be used to create a narrow slice of the sample whose frequency can be selectively excited by the soft pulse. The exact

position of the slice can be set when the system is on resonance. A diagrammatic representation of slice selection for both horizontal and vertical slices is shown in Figure 1.20 (a) and (b) respectively. Multiple slices can then be excited sequentially in different spatial positions, followed by reconstruction to produce a three-dimensional image of the sample.

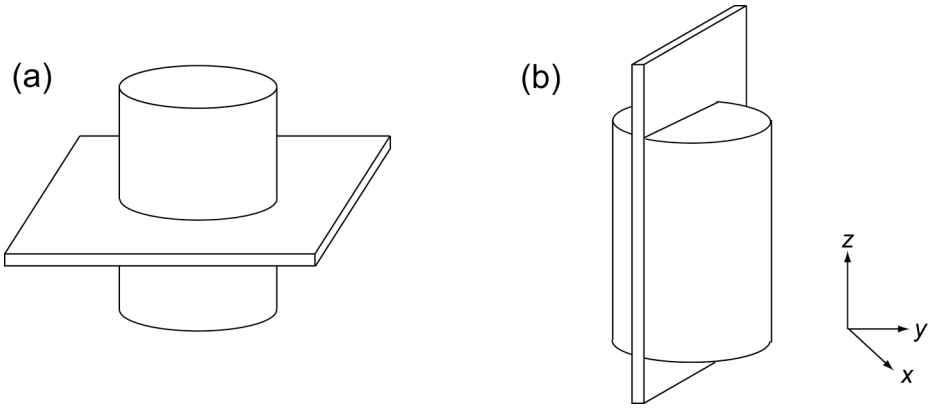

Figure 1.20 Schematic diagram showing slice selection of a cylindrical sample. (a) Shows a horizontal slice and (b) shows a vertical slice.

1.5.5.3. *k*-space

Once a slice has been selectively excited, the data is stored in a construction known as ***k***-space. ***k***-space is the inverse of normal space (a Fourier relationship) and is defined by eq 1.15.

$$\boldsymbol{k} = \frac{\gamma \boldsymbol{G} t}{2\pi} \qquad \text{(eq 1.15)}$$

The wavelength, λ, of the wound helix of phase is equal to $\boldsymbol{k}^{-1}$ (Figure 1.19). For spatial information to be obtained ***k***-space needs to be traversed

though time (frequency encoding) or gradient strength (phase encoding). The direction through which ***k***-space is traversed is defined by the direction of the gradient.

In MRI the construction of a ***k***-space raster is essential. A typical ***k***-space raster for a 2-dimensional 8 × 8 matrix using cartesian coordinates is shown in Figure 1.21. Position in the raster is defined by the strength of the gradient in the phase direction and the time delay in the read (frequency) direction. The initial phase before either the read or the phase gradients are applied is the origin of ***k***-space and corresponds to $\boldsymbol{k}_x = \boldsymbol{k}_y = 0$.

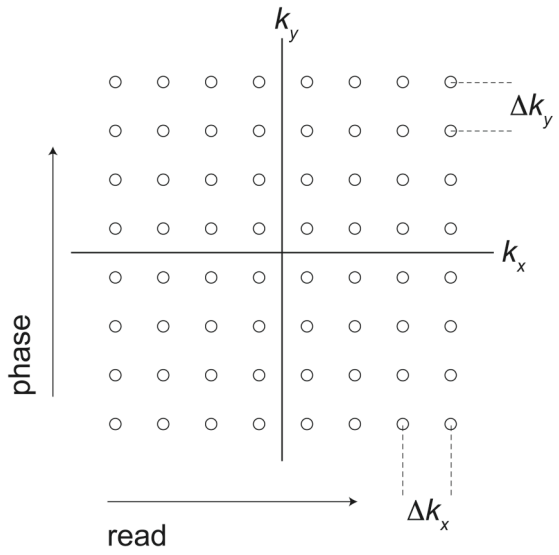

Figure 1.21 Schematic diagram of a ***k***-space raster for a 8 x 8 matrix selected about the *z*-axis. The *x* and *y*-gradients are responsible for the frequency and phase encoding respectively.

The ***k***-space raster can be traversed by applying a particular phase encoding gradient, then applying a read encoding gradient, acquiring data over time. Figure 1.22 shows how ***k***-space can be traversed using a combination of read and phase gradients. Note the negative precursor read

gradient in Figure 1.22, which is used so negative ***k***-space data can be sampled. This method also minimises the effects of switching times for gradient pulses. Other methods can be employed for traversing ***k***-space but will only be acquired in lines for this thesis.

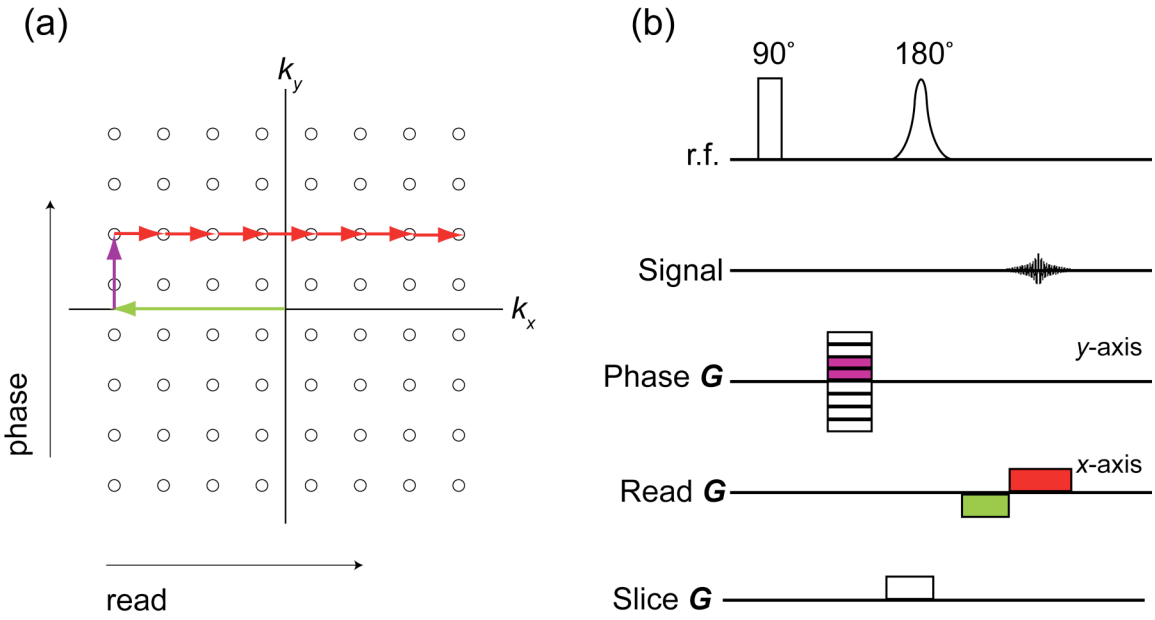

Figure 1.22 Schematic diagram of (a) ***k***-space sample using a combination of read and phase encoding gradients. The timing of the radiofrequency and the gradient pulses are shown in the pulse sequence (b).

1.5.5.4. Experiment Time

MRI experiment times are determined by the experimental parameters. When deciding upon parameters for an imaging experiment, a simple 'rule of thumb' calculation can be used to determine an approximate, but fairly accurate experiment time. E.q. 1.16 shows the approximate experiment time where n_{PE} is the number of phase encoding pixels, T_R is the recovery time and n_{REP} is the number of image repetitions.

$$\text{Experiment time} = n_{PE} \times T_R \times n_{REP} \qquad \text{(eq 1.16)}$$

1.5.5.5. Image Contrast

The purpose of MR imaging is to distinguish between regions of different composition or physical environment. An example of this is shown in Figure 1.23 where an okra has been imaged.

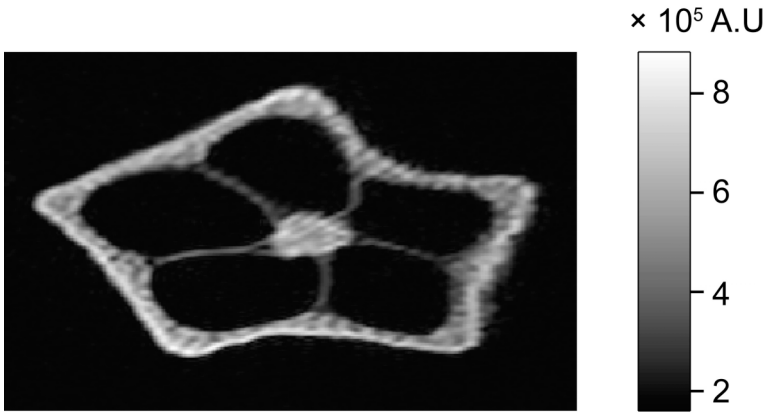

Figure 1.23 A Horizontal MR image of an okra. The bright areas show the highest signal intensity in the sample. The waxy skin seems to have higher signal intensity which could be due to increased spin density. The field of view is 1 cm (vertical) × 1.5 (horizontal).

Areas of differing composition within the okra sample can lead to a variation in signal between pixels. There are four methods through which contrast can be achieved in MR imaging:

(i) Relaxation times

(ii) Spin density

(iii) Chemical shift

(iv) Motional contrast

(i) Relaxation times: Pulse program timings can be adapted to produce relaxation time contrast. The echo time can be adjusted so that it is comparable to T_2 times. The signal then becomes attenuated by a factor of $\exp(-T_E/T_2)$. To ensure there is no T_1-weighting of the image contrast, the repetition time between excitations needs to be significantly longer than T_1. In a T_2–weighted image, the bright regions represent regions with high relaxation times where the signal has not died away.

Fine-tuning the repetition time between excitations can produce T_1-weighted images. This is achieved if the repetition time between excitations is comparable to T_1. Regions of high signal intensity in a T_1-weighted image have relatively short T_1 relaxation times, as the magnetisation has fully relaxed in time for the next excitation.

(ii) Spin density: If a region of a sample has a larger number of excited spins, the region will have higher signal intensity. Images produced using spin density contrast are sometimes referred to as spin density maps. For a spin density map to have no relaxation time contrast, it is necessary for echo times to be shorter than T_2 and repetition times to be significantly longer (5×) than T_1.

(iii) Chemical shift: The concept behind chemical shift contrast is similar to slice selection, discussed previously. Specific regions of a sample may have a particular chemical shift. These regions can be selectively excited

using a long r.f. pulse which excites a narrow spectral region. The resultant image would only show signal from the regions with the excited chemical shift.

(iv) Motional contrast: Motional contrast is particularly useful for this thesis and will be described in greater detail below. This involves the use of a pulse gradient spin echo sequence (PGSE)[85], combined with imaging gradients to produce a map of velocities and/or diffusion coefficients. With this method, pixel intensity is defined by the magnitude of either the diffusive or coherent motion.

1.5.5.6. RARE imaging

Dynamic systems, such as pattern-producing chemical reactions, sometimes require fast imaging sequences in order to characterise the spatio-temporal behaviour of the systems[30]. This can be achieved by reducing the repetition time between excitations but would still be limited by the number of phase pixels in the image. Other pulse sequences have been designed to reduce imaging time, one such sequence is the **R**apid **A**cquisition with **R**elaxation **E**nhancement (RARE)[86]. The RARE pulse sequence is based on a spin echo imaging sequence and is shown in Figure 1.24. Rather than acquiring a single echo per excitation, multiple echoes are collected, thus reducing the experiment time (eq.1.17).

$$\text{Experiment time} = \left(\frac{n_{PE}}{\text{RARE factor}} \right) \times T_R \times n_{REP} \qquad \text{(eq 1.17)}$$

The number of echoes acquired per excitation is also referred to as the RARE factor. The reduced imaging time is offset by a reduction in the signal-to-noise ratio[86] when the T_2 times are short. Each echo acquisition experiences a different attenuation due to T_2 relaxation effects, therefore increasing the RARE factor leads to a greater T_2 image contrast.

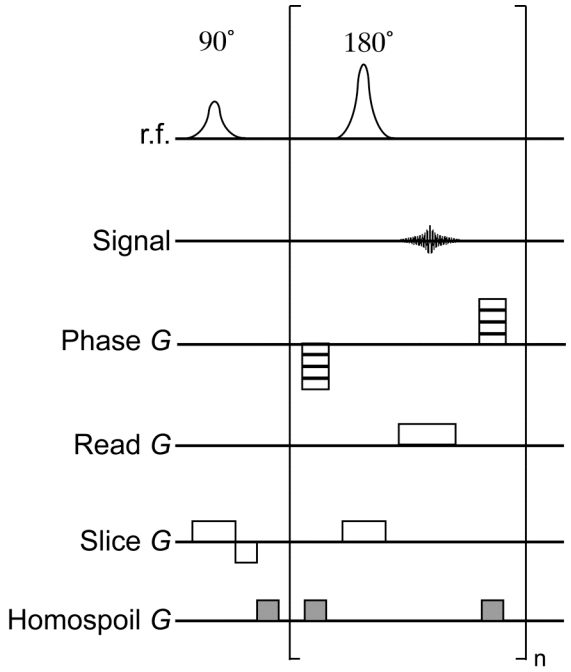

Figure 1.24 Schematic diagram showing a RARE imaging pulse sequence. This pulse sequence is based on the spin echo imaging sequence, except n echoes are collected for each 90˚ r.f. excitation.

1.5.5.7. Magnetic Resonance Imaging of Chemical Patterns

MRI has recently been used for the detection of patterns in the BZ reaction[22-30]. Examples include the measurement of wave velocities[87], three dimensional imaging of spiral waves[22] and the observation of chemical waves in packed bed[30]. MRI has also been shown to produce spatially-resolved

maps of the concentrations of the Mn^{2+} and Mn^{3+} oxidation states catalyst in an analogue of the BZ reaction[29].

Ferroin has already been shown to be a good optical contrast agent, however, visualisation using MRI cannot be achieved using this catalyst/indicator. It is believed to be impossible due to the formation of Fe^{2+} and Fe^{3+} ions, which dominate the relaxation times of the water molecules[24]. These ions are produced as a result of the acid instability of both ferriin and ferroin. Manganese has primarily been used as a contrast agent/catalyst for the detection of oscillations and waves in the BZ reaction[20, 23, 24, 26-28] when using MRI. Water protons surrounding Mn^{2+} have a much shorter relaxation times (both T_1 and T_2) than those surrounding the Mn^{3+} ion. This reduction in the relaxation times of the water is due to the large number of unpaired electrons in Mn. This is in conjunction with the rapid exchange of coordinated water molecules with bulk water.

1.5.5.8. Pulse Gradient Spin Echo (PGSE) Sequence

The understanding of RDA systems is reliant on a complete knowledge of the chemistry, the diffusion coefficients and the fluid velocity. It has already been discussed above that BZ chemistry can be investigated using MRI. MR methods also allow the diffusion coefficients and the fluid velocity to be directly measured.

Displacement of molecules under the influence of magnetic field gradients result in a phase spread of transverse magnetisation. This spreading can be detrimental and can cause loss of signal and artefacts in imaging experiments[88]. The phase difference can, however, be used to

study molecular motion. Echoes are extremely sensitive to molecular motion such as diffusion and flow. The CPMG experiment (explained above) persistently refocusses the transverse magnetisation to remove diffusive effects. The pulse gradient spin echo (PGSE) pulse sequence utilises spin echoes to measure translational motion of molecules[85]. The pulse sequence timings are shown in Figure 1.25.

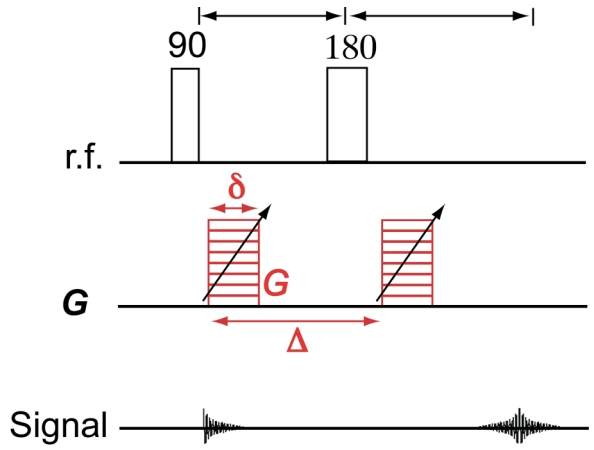

Figure 1.25 Schematic diagram of the PGSE pulse sequence. A 90˚ pulse deflects the bulk magnetisation vector into the *xy*-plane. A helix of phase is then wound using an initial PGSE gradient pulse of duration, δ, and strength, ***G***. A 180˚ pulse refocuses the bulk magnetisation vector. A second PGSE gradient pulse to unwinds the helix wound by the first pulse. Any molecular motion will be detected in the echo.

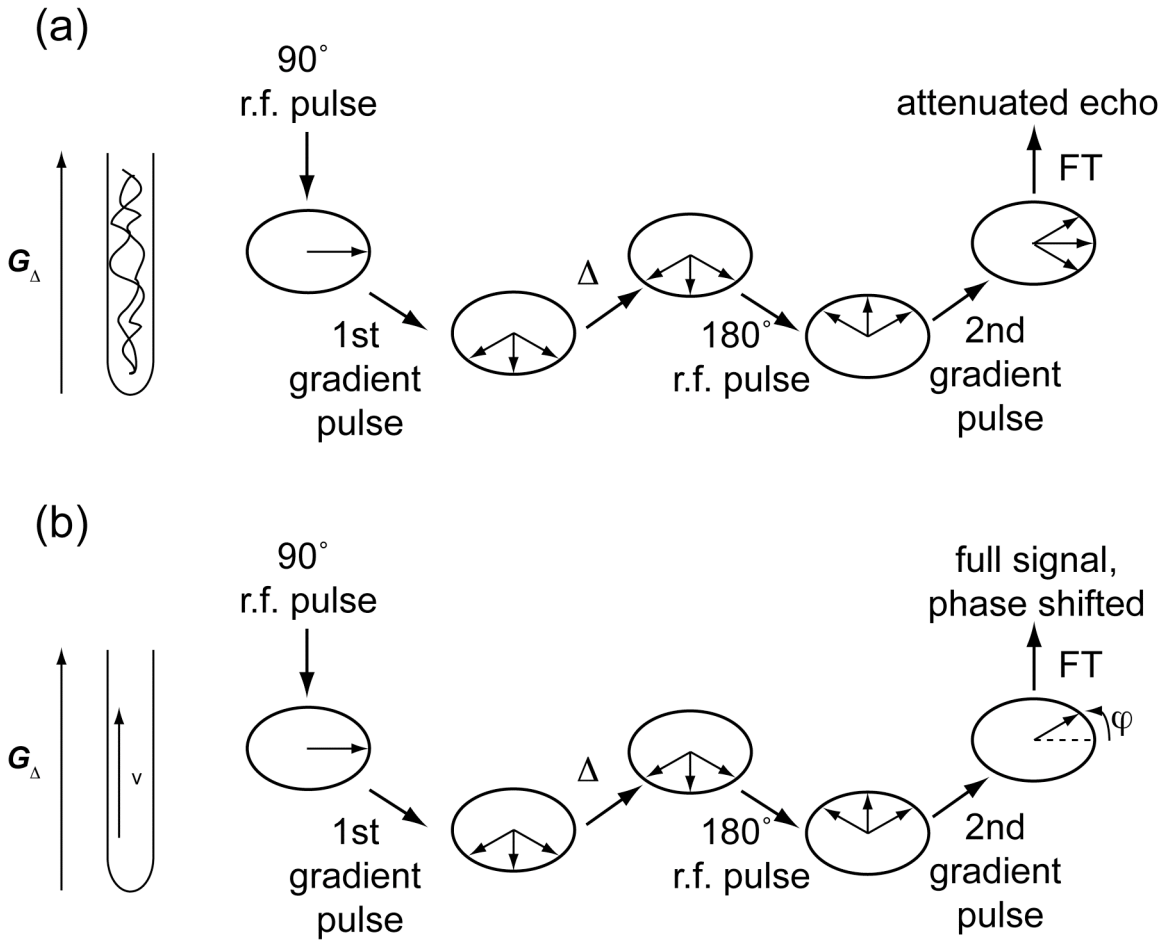

Figure 1.26 Schematic diagram showing the behaviour of spins during a PGSE experiment. (a) Shows the behaviour of the spins in the presence of diffusion and (b) shows the behaviour of the spins in the presence of coherent fluid motion (flow).

Figure 1.26 shows the behaviour of spins during a PGSE experiment in the presence of (a) molecular diffusion and (b) flow. The 90˚ r.f. pulse rotates **M** into the transverse plane. A helix of phase is wound by a gradient pulse with duration, δ and strength, **G**. A 180˚ pulse flips the spins to produce an echo. After a time period, Δ, after the initial gradient pulse, another gradient pulse is used to unwind the helix previously wound by the first gradient pulse.

Any random displacement of molecules (Figure 1.26 (a)) within the experiment window (Δ) results in a spread of the phases of the spins. As a result of this spread, the amplitude of the echo is attenuated. This attenuated signal can be related to the diffusion coefficient using the Stejskal-Tanner equation (eq 1.7)[85], where D is the diffusion coefficient.

$$a_{\Delta}/a_0 = \exp\left\{-\gamma^2 \mathbf{G}^2 \delta^2 D\left(\Delta - \delta/3\right)\right\} \qquad \text{(eq 1.17)}$$

Any coherent motion during Δ, results in a translation of the spins in the direction of the flow. The phase shift induced by the flow (Figure 1.26 (b)) can be related to the fluid velocity by e.q. 1.18 where φ is the phase shift in degrees.

$$\varphi = \frac{\Delta \mathbf{G} \gamma v \delta}{2\pi} \times 360 \qquad \text{(eq 1.18)}$$

The gradient strength can be incrementally increased to produce a plot of gradient strength against echo attenuation[88]. This data can then be Fourier transformed to produce a propagator (Figure 1.27). The width of this propagator is related to the diffusion coefficient and the offset is related to the velocity of the fluid. Δ can also be varied but problems can arise due to relaxation effects at longer Δ values.

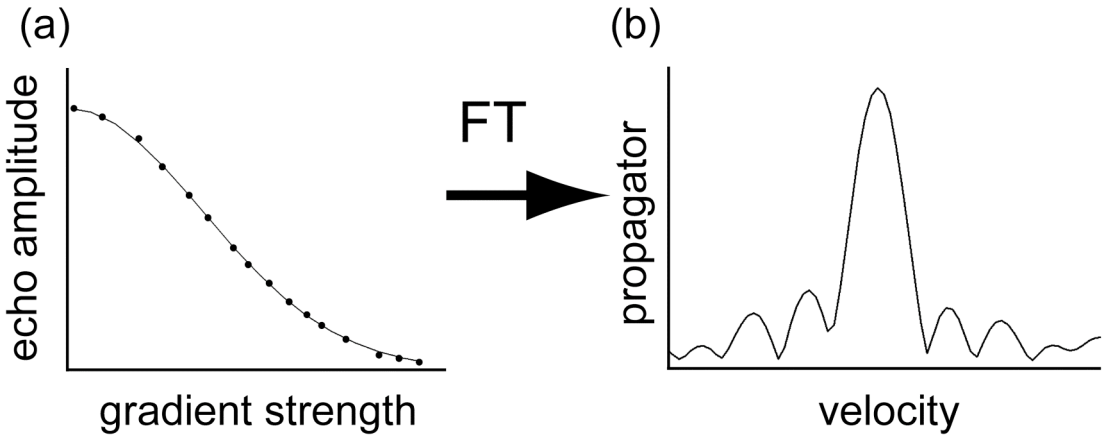

Figure 1.27 (a) Plot of echo attenuation against gradient strength. A Fourier transform is applied to resulting in a propagator (b).

1.5.5.9. NMR Velocity and Diffusion Imaging

By integrating a pair of PGSE gradients with a spin echo imaging experiment, it is possible to produce a spatially resolved map of both velocities and diffusion coefficients[89].

A velocity and diffusion imaging pulse sequence is shown in Figure 1.28. Slice selection occurs during the 180˚ pulse. This imaging sequence allows the simultaneous measurement of both velocity and diffusion via propagator analysis for each pixel. MR velocity imaging has previously been used to visualise Taylor vortex flow in a Couette cell[90].

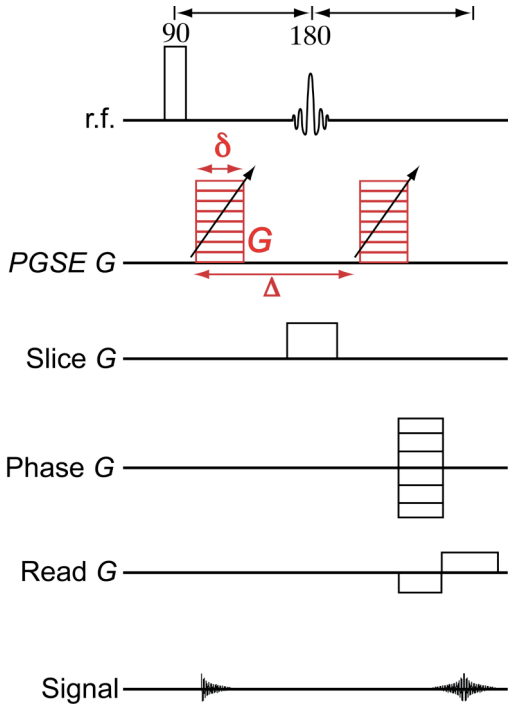

Figure 1.28 Schematic diagram of the Velocity imaging pulse sequence. This sequence is the combination of PGSE and a spin echo imaging sequence. The PGSE gradient pair is intersected by a soft 180˚ r.f. pulse which is used to selectively excite a single slice of the sample. A combination of frequency and phase encoding is then used to spatially encode the velocity or diffusion-weighted data.

1.6. References

[1] P. Ball, *The self-made tapestry : pattern formation in nature*, Oxford University Press, Oxford [England] ; New York, **1999**.

[2] J. M. Davidenko, A. V. Pertsov, R. Salomonsz, W. Baxter, J. Jalife, *Nature* **1992**, *355*, 349.

[3] E. Hernandez-Garcia, C. Lopez, *Ecological Complexity* **2004**, *1*, 253.

[4] L. S. Schulman, P. E. Seiden, *Science* **1986**, *233*, 425.

[5] A. N. Zaikin, Zhabotin.Am, *Nature* **1970**, *225*, 535.

[6] S. K. Scott, *Oscillations, Waves and Chaos in Chemical Kinetics*, Oxford Science Publications, Oxford, **1994**.

[7] J. A. P. Irving R Epstein, **1998**.

[8] B. P. Belousov, in *USSR Academy of Sciences Institute of Applied Physics* (Ed.: M. T. Grechvoa), **1951**.

[9] N. A. Campbell, *Biology*, The Benjamin/Cummings Publishing Company, **1993**.

[10] B. P. Belousov, *Radiats Med* **1958**, *1*.

[11] A. M. Zhabotinsky, *Biofizika* **1964**, *9*.

[12] A. T. Winfree, *Journal of Chemical Education* **1984**, *61*, 661.

[13] R. M. Noyes, R. J. Field, E. Koros, *Journal Of The American Chemical Society* **1972**, *94*, 1394.

[14] I. R. Epstein, V. K. Vanag, *Experimental Chaos* **2003**, *676*, 265.

[15] A. M. Turing, *Philosophical Transactions of the Royal Society London* **1952**, 37.

[16] V. Castets, E. Dulos, J. Boissonade, P. Dekepper, *Physical Review Letters* **1990**, *64*, 2953.

[17] V. K. Vanag, I. R. Epstein, *Physical Review Letters* **2001**, *8722*.

[18] M. Kaern, M. Menzinger, *Physical Review E* **1999**, *60*, R3471.

[19] H. Degn, *Nature* **1967**, *213*, 589.

[20] E. W. Hansen, P. Ruoff, *Journal of Physical Chemistry* **1989**, *93*, 264.

[21] D. Binks, University of Birmingham (Birmingham), **2009**.

[22] A. L. Cross, R. L. Armstrong, C. Gobrecht, M. Paton, C. Ware, *Magnetic Resonance Imaging* **1997**, *15*, 719.

[23] A. R. Cross, R. L. Armstrong, A. Reid, S. Y. Su, M. Menzinger, *Journal of Physical Chemistry* **1995**, *99*, 16616.

[24] Y. Gao, A. R. Cross, R. L. Armstrong, *Journal Of Physical Chemistry* **1996**, *100*, 10159.

[25] M. Menzinger, A. Tzalmona, R. L. Armstrong, A. Cross, C. Lemaire, *Journal Of Physical Chemistry* **1992**, *96*, 4725.

[26] S. Su, M. Menzinger, R. L. Armstrong, A. Cross, C. Lemaire, *Journal Of Physical Chemistry* **1994**, *98*, 2494.

[27] A. Tzalmona, R. L. Armstrong, M. Menzinger, A. Cross, C. Lemaire, *Chemical Physics Letters* **1990**, *174*, 199.

[28] A. Tzalmona, R. L. Armstrong, M. Menzinger, A. Cross, C. Lemaire, *Chemical Physics Letters* **1992**, *188*, 457.

[29] M. M. Britton, *Journal Of Physical Chemistry A* **2006**, *110*, 2579.

[30] M. M. Britton, A. J. Sederman, A. F. Taylor, S. K. Scott, L. F. Gladden, *Journal Of Physical Chemistry A* **2005**, *109*, 8306.

[31] A. L. Lin, M. Bertram, K. Martinez, H. L. Swinney, A. Ardelea, G. F. Carey, *Physical Review Letters* **2000**, *84*, 4240.

[32] A. Pikovsky, M. Rosenblum, J. Kurths, *Synchronisation: a universal concept in nonlinear sciences*, Cambridge University press, Cambridge, **2001**.

[33] Mcclinto.Mk, *Nature* **1971**, *229*, 244.

[34] E. V. Appleton, *Proceedings of the Cambridge Philosophical Society* **1923**, *21*, 231.

[35] Z. Neda, E. Ravasz, Y. Brechet, T. Vicsek, A. L. Barabasi, *Nature* **2000**, *403*, 849.

[36] A. Pikovsky, M. Rosenblum, J. Kurths, *Synchronization : a universal concept in nonlinear sciences*, Cambridge University Press, Cambridge, **2001**.

[37] G. H. Baillie, *Nature* **1941**, *148*, 412.

[38] V. Petrov, Q. Ouyang, H. L. Swinney, *Nature* **1997**, *388*, 655.

[39] A. J. Perumpanani, J. A. Sherratt, P. K. Maini, *Ima Journal of Applied Mathematics* **1995**, *55*, 19.

[40] D. Binks, PhD Thesis, **2009**

[41] S. P. Kuznetsov, E. Mosekilde, G. Dewel, P. Borckmans, *Journal Of Chemical Physics* **1997**, *106*, 7609.

[42] P. N. McGraw, M. Menzinger, *Physical Review E* **2003**, *68*.

[43] A. F. Taylor, J. R. Bamforth, P. Bardsley, *Physical Chemistry Chemical Physics* **2002**, *4*, 5640.

[44] J. R. Bamforth, R. Toth, V. Gaspar, S. K. Scott, *Physical Chemistry Chemical Physics* **2002**, *4*, 1299.

[45] M. Kaern, M. Menzinger, *Journal Of Physical Chemistry A* **2002**, *106*, 4897.

[46] R. Toth, A. Papp, V. Gaspar, J. H. Merkin, S. K. Scott, A. F. Taylor, *Physical Chemistry Chemical Physics* **2001**, *3*, 957.

[47] A. Taylor, *Advances In Complex Systems* **2003**, *6*, 155.

[48] A. F. Taylor, M. M. Britton, *Chaos* **2006**, *16*.

[49] L. F. Gladden, M. D. Mantle, A. J. Sederman, E. H. L. Yuen, *Applied Magnetic Resonance* **2002**, *22*, 201.

[50] A. J. Sederman, L. F. Gladden, *Magnetic Resonance Imaging* **2001**, *19*, 339.

[51] M. Leconte, J. Martin, N. Rakotomalala, D. Salin, *Physical Review Letters* **2003**, *90*.

[52] P. D. Ronney, B. D. Haslam, N. O. Rhys, *Physical Review Letters* **1995**, *74*, 3804.

[53] C. R. Nugent, W. M. Quarles, T. H. Solomon, *Physical Review Letters* **2004**, *93*.

[54] M. S. Paoletti, C. R. Nugent, T. H. Solomon, *Physical Review Letters* **2006**, *96*.

[55] M. S. Paoletti, T. H. Solomon, *Physical Review E* **2005**, *72*.

[56] M. S. Paoletti, T. H. Solomon, *Europhysics Letters* **2005**, *69*, 819.

[57] A. Pocheau, F. Harambat, *Physical Review E* **2008**, *77*.

[58] J. R. Boehmer, T. H. Solomon, *Epl* **2008**, *83*.

[59] O. Steinbock, J. Schutze, S. C. Muller, *Physical Review Letters* **1992**, *68*, 248.

[60] P. T. Callaghan, *Reports On Progress In Physics* **1999**, *62*, 599.

[61] E. L. Koschmieder, *Bénard cells and Taylor vortices*, Cambridge University Press, Cambridge [England] ; New York, **1993**.

[62] R. M. Lueptow, A. Docter, K. Y. Min, *Physics of Fluids a-Fluid Dynamics* **1992**, *4*, 2446.

[63] R. M. Lueptow, *Physics of Rotating Fluids* **2000**, *549*, 137.

[64] Z. H. Gu, T. Z. Fahidy, *Canadian Journal of Chemical Engineering* **1985**, *63*, 14.

[65] Z. H. Gu, T. Z. Fahidy, *Canadian Journal of Chemical Engineering* **1985**, *63*, 710.

[66] H. A. Snyder, *Proceedings of the Royal Society of London Series a-Mathematical and Physical Sciences* **1962**, *265*, 198.

[67] K. Kataoka, Doi, H., Komai, T., Futagawa, M., *Journal of Chemical Engineering Japan* **1975**, *8*, 472.

[68] S. T. Wereley, R. M. Lueptow, *Physics of Fluids* **1999**, *11*, 3637.

[69] R. C. Giordano, R. L. C. Giordano, D. M. F. Prazeres, C. L. Cooney, *Chemical Engineering Science* **1998**, *53*, 3635.
[70] D. Coles, *Journal of Fluid Mechanics* **1965**, *21*, 385.
[71] P. Ashwin, G. W. Mann, G. P. King, *Physical Review Letters* **1995**, *75*, 4610.
[72] R. L. C. Giordano, R. C. Giordano, D. M. F. Prazeres, C. L. Cooney, *Chemical Engineering Science* **2000**, *55*, 3611.
[73] L. F. Gladden, *Chemical Engineering Science* **1994**, *49*, 3339.
[74] L. F. Gladden, *Aiche Journal* **2003**, *49*, 2.
[75] A. Timur, *Journal of Petroleum Technology* **1969**, *21*, 775.
[76] M. M. Britton, *Journal Of Physical Chemistry A* **2003**, *107*, 5033.
[77] M. M. Britton, *Journal Of Physical Chemistry A* **2006**, *110*, 5075.
[78] R. Evans, C. R. Timmel, P. J. Hore, M. M. Britton, *Journal Of The American Chemical Society* **2006**, *128*, 7309.
[79] M. H. Levitt, *Spin Dynamics; Basics of Nuclear Magnetic Resonance*, Wiley, **2001**.
[80] P. T. Callaghan, *Principles of Nuclear Magnetic Resonance Microscopy*, Oxford University Press, Oxford, **1991**.
[81] R. Freeman, *Magnetic Resonance in Chemistry and Medicine*, Oxford University Press, **2003**.
[82] P. W. Atkins, J. De Paula, *Atkins' Physical chemistry*, 7th ed., Oxford University Press, Oxford ; New York, **2002**.
[83] E. L. Hahn, *Physical Review* **1950**, *80*, 580.
[84] H. Y. Carr, E. M. Purcell, *Physical Review* **1954**, *94*, 630.
[85] E. O. Stejskal, J. E. Tanner, *Journal of Chemical Physics* **1965**, *42*, 288.
[86] J. Hennig, A. Nauerth, H. Friedburg, *Magnetic Resonance in Medicine* **1986**, *3*, 823.
[87] A. Cross, The University of New Brunswick (New Brunswick), **1998**.
[88] P. T. Callaghan, *Principles of nuclear magnetic resonance microscopy*, Clarendon Press ; Oxford University Press, Oxford [England], New York, **1991**.
[89] P. T. Callaghan, C. D. Eccles, Y. Xia, *Journal of Physics E-Scientific Instruments* **1988**, *21*, 820.

[90] J. D. Seymour, B. Manz, P. T. Callaghan, *Physics Of Fluids* **1999**, *11*, 1104.

2. Chapter 2 Chemical Patterns in Plug Flow

2.1. Introduction

Flow-distributed oscillation (FDO) patterns are stationary patterns produced in open flow via a non-Turing mechanism[1]. These patterns have previously only been produced in packed bed reactors[2, 3]. A packed bed reactor consists of a pipe reactor filled with a packing material (for example glass beads), which is used to induce a plug-like flow. Magnetic resonance velocity imaging has shown that flow within a packed bed consists of fast-flowing channels and stagnant pockets[4], which has been shown to affect both pattern formation and the structure of FDO patterns[5]. Therefore, there is interest in the development of a flow system where no packing material is required.

This chapter reports the investigation of FDO patterns in a plug flow system in the absence of a packing material. This system worked by adding agar gel to the Belousov-Zhabotinsky reactants and passing it through a pipe reactor. The flow field within this system was measured using NMR velocity and diffusion imaging.

FDO patterns produced in this system were investigated using optical imaging. The formation and temporal behaviour was studied using space-time plots and was compared to patterns produced in a packed bed reactor. The effect on wavelength of FDO patterns was investigated as a function of both initial reactant concentration and reactor temperature.

A periodic change in reaction tube temperature was used as a forcing parameter. Lissajous plots were constructed to investigate synchronisation behaviour between the FDO patterns and the external temperature forcing.

2.2. Experimental

All plots shown in this chapter represent results from three experimental repeats unless otherwise stated. The points on the graphs show the average value from the three experiments with the error bars showing the range of the data over the three experiments.

2.2.1. Reagents

Malonic acid (Sigma, Gillingham, UK, 99 %), sodium bromate (Sigma, Gillingham, UK, 99 %), sulfuric acid (Fisher, Loughborough, UK, 98 %), agar (Sigma, Gillingham, UK, ash 2-4%), agarose (Sigma, Gillingham, UK, ash 1%) and κ-carageenan (Fluka, Gillingham, UK,) were all used without further purification. Ferroin catalyst/indicator was prepared by dissolving iron (II) sulfate heptahydrate (Sigma, Gillingham, UK, 98 %) and 1,10-phenanthroline (Sigma, Gillingham, UK, 99 %) in a 1:3 ratio in deionised water (Elga Process Water, Marlow, UK). All reagents were prepared freshly on the day of the experiment. The solutions were degassed prior to experimentation. The reactants for the Belousov-Zhabotinsky reaction were separated into two stock solutions. The sulfuric acid and ferroin were placed in one, and malonic acid and sodium bromate were placed in the other. This was done in order to prevent the onset of oscillations prior to mixing.

2.2.2. Well-Stirred Belousov-Zhabotinsky Reaction

Temporal oscillations were studied in the well-stirred ferroin-catalysed Belousov-Zhabotinsky reaction. The two prepared stock solutions were mixed and placed into a temperature-controlled vessel. Solution A consisted of [MA] = 0.52 M and [BrO_3^-] = 0.32 M. Solution B consisted of [H_2SO_4] = 0.26 M and [ferroin] = 3.74×10^{-3} M. The reaction was vigorously stirred by a magnetic follower, which was driven by a magnetic stirrer (IKA, Staufen, Germany). The potential difference of the solution was used to monitor the reaction over time with a Pt-combination electrode employing a Picoscope Oscilloscope (Picotech, Cambridge, UK) and the Picotech software.

2.2.3. Flow Distributed Oscillation Apparatus

A schematic diagram of the general experimental setup for the production of FDO patterns is shown in Figure 2.1. Stock solutions (A and B) were pumped into a continuously stirred tank reactor (CSTR) with a volume of 3 cm^3 using a peristaltic pump (Ismatec, Glattbrugg, Switzerland). From the CSTR, the reacting solution was then fed via PTFE capillary tube (1.3 mm inner diameter and 10 cm length (Cole Parmer, London, UK) into a glass tube with a length of 150 cm. The short length of the capillary tube and the small volume of the CSTR maintain the boundary conditions at the inlet of the reactor. If the volume of the CSTR was too large or the length of the capillary is too long, the phase of the reaction would change at the reactor inlet, resulting in travelling waves. The residence time of the reacting solution in the CSTR and the capillary tube was less than 30 seconds.

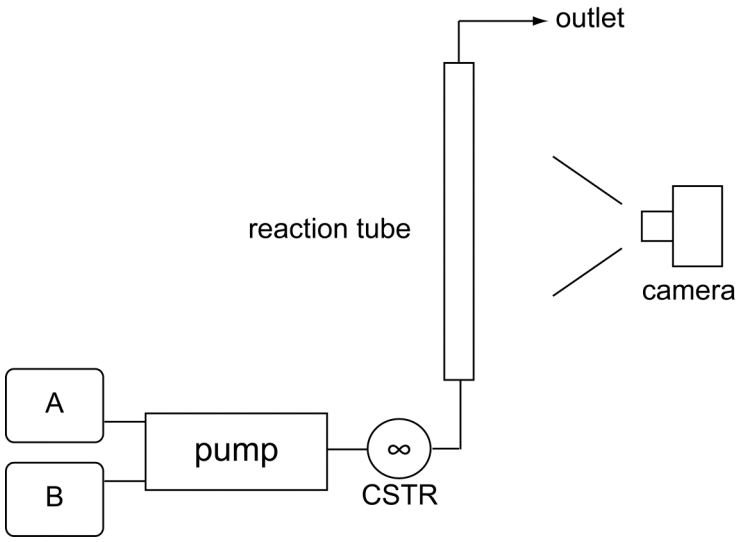

Figure 2.1 Schematic diagram of the general experimental setup for flow-distributed oscillation experiments. The stock solutions A and B were pumped into the reaction tube via the CSTR.

2.2.4. Optical Imaging and Analysis

Optical images of reaction tube were acquired over time to study the temporal behaviour of the chemical patterns. Optical images were acquired in less than a second, with a delay of twenty seconds between acquisitions, using a digital CCD camera (Canon Power Shot A520), which were transferred via USB to a PC.

The ferroin-catalysed Belousov-Zhabotinsky reaction switches between two states. This can be visualised using the colour change of the catalyst upon oxidation/reduction. One state of the catalyst is red ferroin (Fe^{2+}) and the other state of the catalyst is blue ferriin (Fe^{3+}). Adobe Photoshop (Adobe, Dublin, Ireland) was used to isolate the reaction tube from the digital photographs, so that only the reaction tube was shown. The red and green

components of the extracted image from the tube were then removed, which left only the blue. This data was then exported as a bitmap file to Prospa[6] image analysis software (Magritek, Wellington, New Zealand).

A schematic representation of how the bitmap files were analysed is shown in Figure 2.2. (a) Five lines of pixels were extracted vertically from the centre of the reaction tube. This produced a plot of intensity of blue as a function of position, (b). The intensity profiles were then plotted against time, producing a space-time plot in which high intensity areas are related to high ferriin concentration, (c).

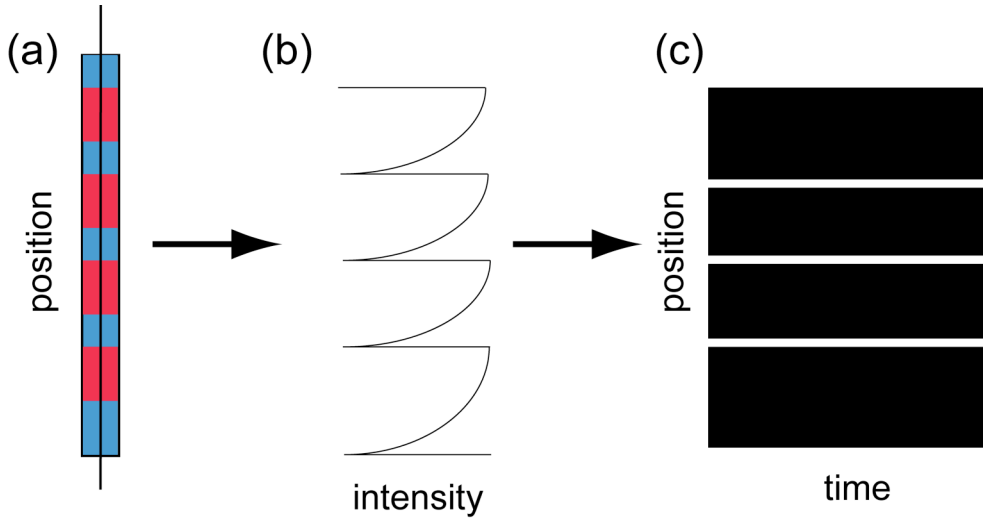

Figure 2.2 A schematic diagram to show the production of a space-time plot. The intensity profile shown in (b) is extracted from the optical image, (a). The intensity for each time frame is then plotted out as a function of time as shown in (c).

2.2.5. Packed Bed Reactor Experiments

The experimental setup described in section 2.2.3 was used for the production of chemical patterns in the packed bed reactor. The reaction tube

was pre-filled with 0.13 M sulphuric acid, the concentration of which was consistent with the initial conditions of the BZ reaction. The reaction tube was filled with 1 mm diameter glass beads (Biospec, Bartlesville, USA, 2.5 g/cm^3 density) in order to produce a plug-like flow. Solution A consisted of [MA] = 0.52 M and [BrO_3^-] = 0.32 M. Solution B consisted of [H_2SO_4] = 0.26 M and [ferroin] = 3.74×10^{-3} M. The volume flow rate was 10 cm^3 min^{-1}. The reaction vessel temperature was maintained at 18 ˚C ± 0.5 ˚C by a water jacket, which was controlled by a water bath (Huber, polystat cc3, Chippenham, UK).

2.2.6. Flow Experiments with No Packing Material

Experiments were conducted, under flow, in the absence of a packing material. In order to produce plug flow, agar was added to the reaction mixture prior to entry into the reaction tube. For these reactions three stock solutions were used. Solution A consisted of [MA] = 1.04 M and [BrO_3^-] = 0.64 M. Solution B consisted of [H_2SO_4] = 0.52 M and [ferroin] = 7.48×10^{-3} M. Solution C was a 1.8% w/v aqueous solution of gel (agar, agarose or κ-cerrageenan), which was held at a temperature of 45 ˚C (to prevent gellation). Solution C was pumped into the CSTR by two separate feeds. Upon entry into the reaction tube, the solution formed a gel between 5 and 10 cm, which was essential for the formation of stable chemical patterns.

For the Poiseuille flow experiments, the agar was replaced with deionised water so no gellation occurred. The concentrations of the BZ reactants were kept constant for these experiments.

2.2.7. NMR Velocity and Diffusion measurements

All NMR measurements were performed on a Bruker DMX 300 spectrometer operating at a proton resonance frequency of 300 MHz. The temperature of the bore was 289.4 K ± 1 K. A probe was used, which consisted of a 25 mm diameter saddle-coil r.f. resonator and water-cooled triple axis magnetic field gradients with a maximum *z* gradient strength of 140 G cm^{-1}. The maximum gradient strength in the *x* and *y* directions was 48 G cm^{-1}.

The empty reaction tube was placed inside the bore of the superconducting magnet. Once set up, the agar solution was pumped up the reaction tube. An air-pocketed chamber (Figure 2.3) was used prior to the solutions entering the reaction tube to dampen the peristaltic flow, which would introduce flow artefacts into the images. Velocity images were acquired of the gelled agar solution under flow in a tubular reactor. The agar solution was the same concentration as used in the FDO experiments but without the BZ reactants. The absence of ferroin and ferric ions lengthened the relaxation time of the water protons, making the velocity measurements possible.

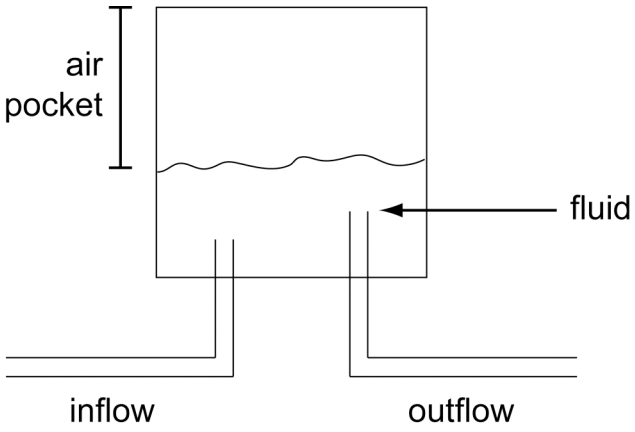

Figure 2.3 Schematic diagram of an air-pocketed chamber used to reduce pulsatile flow from the peristaltic pump.

A VISEHS (**v**elocity **i**maging **s**pin **e**cho **h**ard **s**oft) sequence was used to map both the fluid velocity and diffusion coefficients within the reaction tube. This velocity imaging sequence is the combination of a PGSE and a spin echo imaging sequence. VISEHS consists of a hard 90˚ pulse, followed by a soft, slice-selective 180˚. A vertical slice was acquired with a slice thickness of 1 mm with a field of view of 60 mm (vertical) × 30 mm (horizontal) and a matrix size of 128 × 64 pixels resulting in a pixel size of 0.469 × 0.469 mm. The PGSE gradient parameters used were: Δ = 40 ms, δ = 1 ms and **G** = 0.2 T m^{-1}. The recovery time between excitations was 1 s. PGSE parameters were chosen to provide sufficient phase shift and signal attenuation for both the velocity and diffusion maps. The data was analysed using Prospa NMR analysis software (Magritek, Wellington, New Zealand).

2.3. Results and Discussion

2.3.1. The Well-Stirred Belousov-Zhabotinsky Reaction

The well-stirred ferroin-catalysed Belousov-Zhabotinsky (BZ) reaction chemistry was characterised prior to study of the reaction under flow. Temporal oscillations were measured using potentiometric methods, described in Chapter 1. The measured electrode potential was able to probe the change in oxidation state of the catalyst, from red ferroin (Fe^{2+}) to blue ferriin (Fe^{3+}) over time (Figure 2.4).

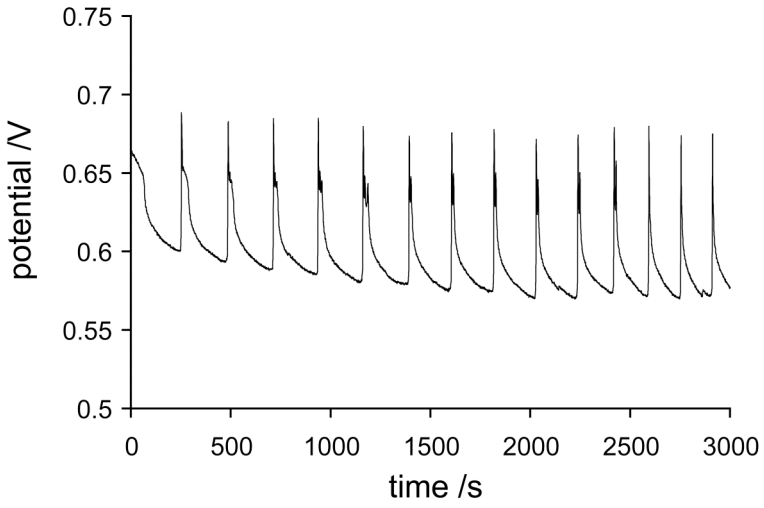

Figure 2.4 Plot showing the measured potential of the well-stirred ferroin-catalysed BZ reaction over time. The peaks and troughs correspond to the ferriin and ferroin catalyst states respectively.

The reaction started in the oxidised (blue) state. A very short induction period of 250 s preceded the oscillatory behaviour. The short induction period was essential for the FDO experiments so multiple bands could be observed

in the reaction tube. If the induction period was too long, the reactants would pass through the tube without switching state.

Following the induction period, a series of peaks and troughs in the potential were observed, which corresponded to switches from ferriin to ferroin respectively. The switch to ferriin occurred rapidly, followed by a slower relaxation to the ferroin state. The magnitude of the potential change is indicative of the conversion ratio of the ferroin/ferriin catalyst states[7]. The potential difference between the ferriin and ferroin states increased as the reaction proceeded. This indicated that the conversion ratio at the start of the experiment was not 100%. The period between the oscillations was measured from the peak-to peak distance in the range of 213 to 237 s. This oscillation period was suitable for the production of FDO patterns, as it would allow the observation of multiple bands.

2.3.2. Flow Distributed Oscillations in a Packed Bed Reactor

When the Belousov-Zhabotinsky reaction is placed under flow, stationary patterns can form along a pipe reactor[1]. These patterns have been termed flow-distributed oscillation (FDO) patterns[2]. FDO patterns have been explained in terms of temporal oscillations distributed through space by a flow. One of the requirements for the production of these patterns is plug flow. An approximation of this flow has previously been achieved using a packed bed reactor[4].

The BZ reaction under flow in a packed bed reactor was studied so the formation of FDO bands could be understood. A typical time-series of optical images acquired of the chemical bands in a packed bed reactor is shown in

Figure 2.5. The images show a reaction tube which is mainly red, intersected with a series of blue bands. The red and blue areas correspond to high ferroin and ferriin concentration respectively.

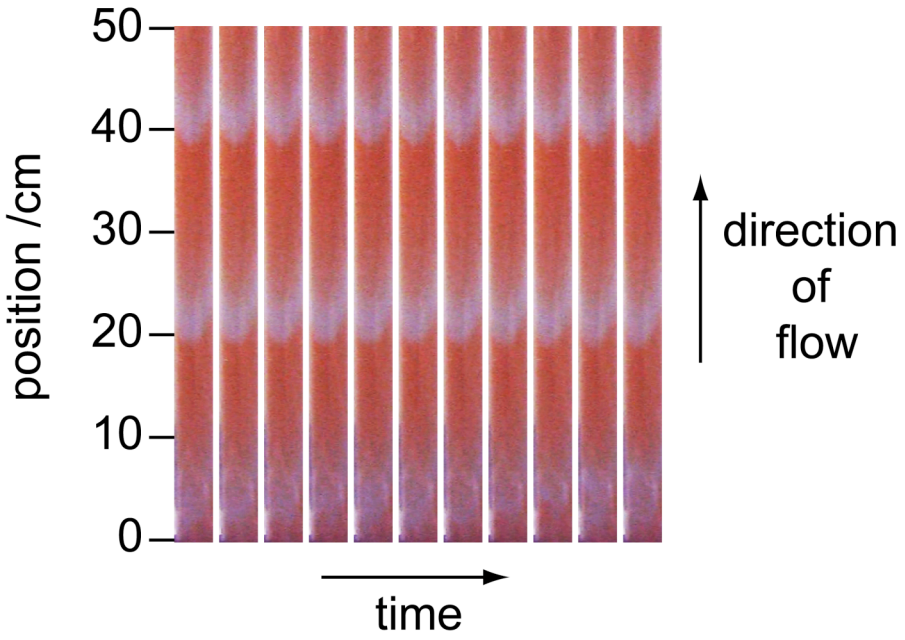

Figure 2.5 A time series of optical images of stationary FDO patterns in a packed bed reactor, using the ferroin-catalysed BZ reaction. Images were acquired every twenty seconds. The images have been enhanced to show the colour contrast between the blue and red regions.

Three distinct chemical bands can be seen in the reactor, shown in Figure 2.5. The initial band at the bottom of the reactor was centred at 4 cm with two subsequent bands at 22 and 41 cm. The bands were periodic through space and fixed over time confirming them as stationary FDO patterns[1].

A space-time plot of the reaction allows the formation and the temporal behaviour of the patterns to be analysed. A light gradient can be seen in the

space-time plot, where the intensity of light increased further up the tube due to the proximity to the light source.

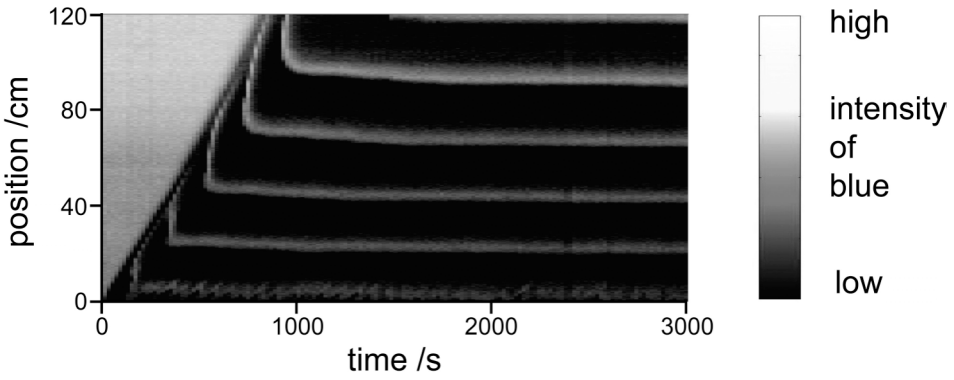

Figure 2.6 A space-time plot of stationary FDO patterns in a packed bed reactor using the ferroin-catalysed BZ reaction.

The region from 0 to 800 s in the space-time plot shows the packed bed filling up with the BZ reactants. The initial band was produced as the reactants began to fill the tube. Four subsequent bands were produced after the formation of the initial band. The formation of these bands occurred via the wavesplitting mechanism, reported previously[3]. This involved the formation of an excitation point, from which two bands propagated. One band travelled up the tube, propelled by the flow. The other band travelled down, against the flow and settled at a steady-state position.

The period between the formation of excitation points is defined by the period between oscillations in the well-stirred reaction[3]. For the packed bed experiments, the excitation point formation period was found to be in the range of 180 to 240 s. This is comparable to the well-stirred BZ reaction from the previous section, where the period between oscillations was 213 to 237 s.

The wavelength of the patterns was measured from the top of a band to the top of the next. The average wavelength for the system was calculated for all the waves in the tube as 24 ± 2 cm. The linear velocity of the reactants through the tube can be calculated from the space-time plot.

Previously, the wavelength of the patterns has been predicted using a kinematic equation[2], which described the FDO bands in terms of well-stirred BZ reaction oscillations, distributed by the flow. The kinematic wavelength can be calculated from eq 2.1 where λ is the wavelength, τ is the period between the oscillations and v is the linear velocity of the fluid through reaction tube.

$$\lambda = \tau \times v \qquad \text{(eq 2.1)}$$

The predicted wavelength for the packed bed experiments, shown in Figure 2.6, was 33.9 cm. The large discrepancy between the calculated and experimental wavelengths has previously been described by Bamforth *et al*.[3]. It was argued that this difference was due to axial dispersion effects, not accounted for in eq 2.1[8]. Dispersion in the axial direction leads to a mixing between adjacent fluid packets. The adjacent fluid packets are in different phases of oscillation and mixing between these packets causes the phase of each packet to change, therefore reducing the wavelength of the FDO patterns.

The flow field within the packed bed has been analysed in detail using NMR velocity imaging[9]. This investigation showed the flow within the packed bed consisted of a combination of fast-flowing channels and stagnant pockets.

The fast flowing channels could cause an uneven distribution of oscillation phases within the reactor, resulting in a modulation of the wavelength. In addition to this, the stagnant pockets could oscillate independently. Diffusion from these pockets could cause the oscillation phase of neighbouring regions to be altered.

FDO patterns in a packed bed reactor have previously been studied using magnetic resonance imaging by Britton *et al*.[5]. This imaging technique provided information on the formation and three-dimensional structure of stationary FDO patterns using the manganese-catalysed BZ reaction. The shape of the patterns was shown to be conical, which was attributed to the velocity field within the packed bed.

2.3.3. Flow-Distributed Structures Without Packing Material

FDO patterns have previously only been produced in packed bed reactors in order to produce a plug-like flow. A plug flow profile is where the velocity of the fluid is uniform across the width of the tube. The plug flow profile is essential, so the phase of the chemical oscillation is identical through the width of the reaction tube. It has been shown previously that the packed bed reactor is not an idealised plug flow. It would, therefore, be of interest to find a system where a packed bed is not required in which to study FDO patterns.

Plug flow through a tube can be achieved by a number of methods. Shear thinning materials have been shown to produce a plug flow profile through a tube by NMR velocity imaging[10]. Attempts were made to produce

a suitable system employing shear-thinning polymers. In particular, Xanthan gum and high-molecular weight polyethylene oxide were mixed with the BZ reactants. Both systems were found to be unworkable, as the viscous polymer solutions did not easily mix with the BZ reactants.

Gel systems provide an alternative to shear thinning polymers for the production of plug flow through a tube. Some gel systems, such as alginate, are formed by cross linking with a metal cation[11]. This would be unsuitable due to the ferroin catalyst cross-linking the gel, which could affect pattern formation within the reactor. Other gel systems, such as agar, are dissolved in water by heating, followed by cooling to form a gel. Many gel systems have previously been used for the BZ reaction in order to stabilise patterns and reduce convective effects[11, 12]. The gels used for the reactants include agar, agarose and silica gel.

2.3.4. NMR Velocity and Diffusion Imaging

A flow system was developed, where agar was mixed with the BZ reactants prior to entry into the reaction tube. The flow within the agar system was characterised with NMR velocity and diffusion imaging[13]. An aqueous solution of agar, in the absence of BZ reactants, was used for the flow measurements. The tube diameter was different to the BZ experiments shown below but the flow profile of the gel can still be understood from these measurements.

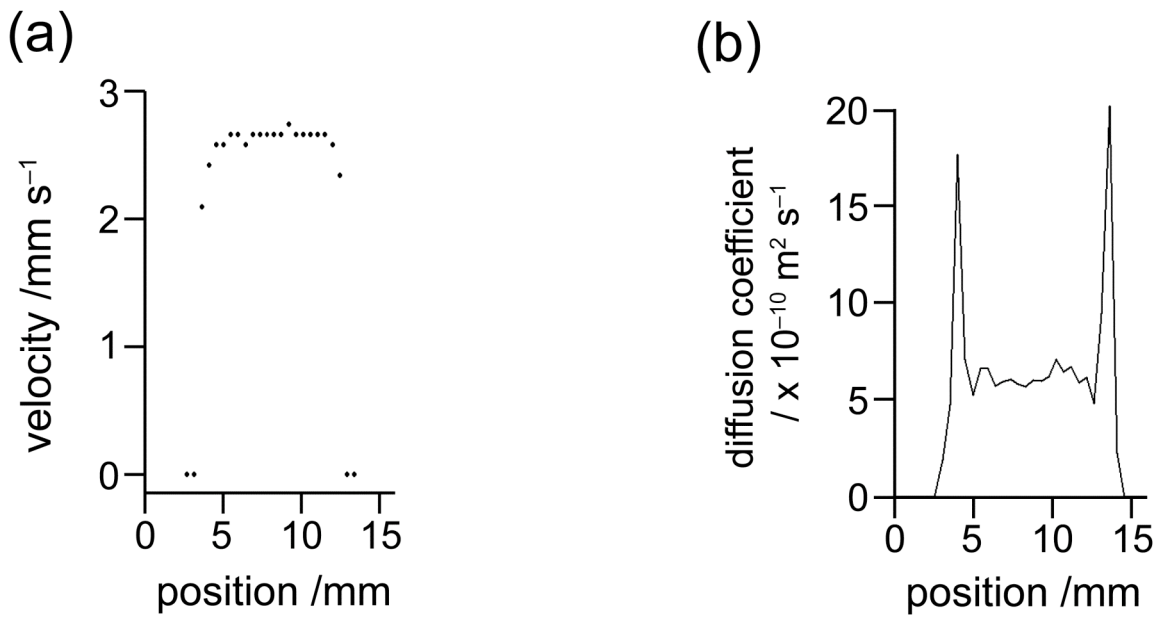

Figure 2.7 Velocity and diffusion profiles of an aqueous solution of agar passed through a tube a reaction tube. (a) Shows a single velocity profile through the centre of the reaction tube and (b) shows a single diffusion profile through the centre of the reaction tube.

Figure 2.7 (a) shows a one-dimensional profile of the velocities of the agar solution across the width of the reactor tube. The flow velocities are virtually uniform across the tube. This confirmed a plug flow profile. A reduction of fluid velocity was observed at the outer cylinder wall, which was due to the no-slip boundary condition. The no-slip boundary condition states that the fluid velocity at the boundary (tube wall) is equal to the velocity of the boundary (i.e. zero)[14]. There was also evidence to show that some of the agar gel sticks to the tube when passing through. This was shown by a residual film of agar, which adhered to the reaction tube post-experiment.

Figure 2.7 (b) shows a diffusion profile of the agar solution through the width of the tubular reactor. The diffusion coefficient was shown to be virtually uniform across the annulus of the tube, except for two regions of increased

diffusion coefficient at the walls of the reactor. As mentioned previously, the velocity at the walls of the reactor was close to zero. This resulted in a high velocity gradient, therefore increasing the fluid shear[14]. This shear resulted in enhanced diffusion at the walls of the reactor[15].

These experiments showed that an agar solution pumped through a reaction tube induced a plug-flow profile when neglecting the boundary conditions.

2.3.5. Patterns Produced in an Agar Plug-Flow Reactor

The ferroin-catalysed BZ reactants were mixed with agar prior to entry into a tubular reactor. Figure 2.8 shows a series of optical images of the reaction tube at twenty-second intervals.

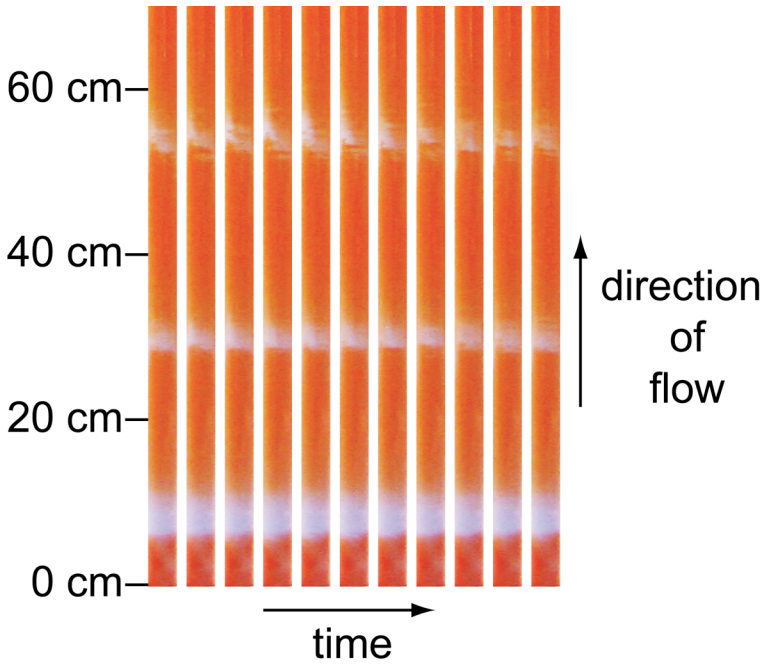

Figure 2.8 A time series of optical images of chemical bands produced with agar mixed with the ferroin-catalysed BZ reaction. Images were acquired every twenty seconds. The images have been enhanced to show the colour contrast between the blue ferriin (Fe^{3+}) and red ferroin (Fe^{2+}).

Three distinct ferriin-containing bands can be seen through the reaction tube in Figure 2.8. The positions of the three bands are shown at 5, 30 and 52 cm. The bottom band is larger than the subsequent bands, which is consistent with the well-stirred reaction shown in Figure 2.4, where the residence time in the ferriin state is longer for the induction period. The positions of the bands are quasi-periodic through space and stationary over time, confirming them as stationary FDO patterns[1].

The contrast between blue and red areas is significantly increased in the agar system compared to the packed bed reactor. This can be attributed to the optical opacity and high reflectivity of the glass beads in a packed bed reactor.

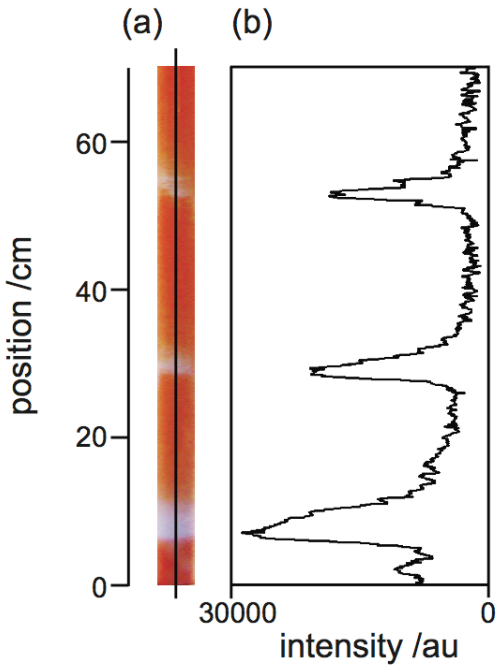

Figure 2.9 (a) Shows a single image of stationary FDO patterns produced with the ferroin-catalysed BZ reaction, mixed with agar. (b) Shows an intensity profile of the blue colour through the reaction tube. The profile was extracted from the centre of the tube, as shown by the black line in (a).

It can be seen from the optical images in Figure 2.8 that the intensity of the ferriin bands decreased further up the tube. This decrease is highlighted by the intensity plot in Figure 2.9 (b), which was extracted from the image in Figure 2.9 (a). The reduction in intensity can be explained by the deposition of agar onto the reaction tube walls. This deposition increased further up the tube, which explains the reduction in the signal.

A space-time plot was constructed for the agar system, shown in Figure 2.10. The space-time plot shows the intensity of blue through the reaction tube over time. The region from 0 to 1100 s shows the BZ reactants filling the tube.

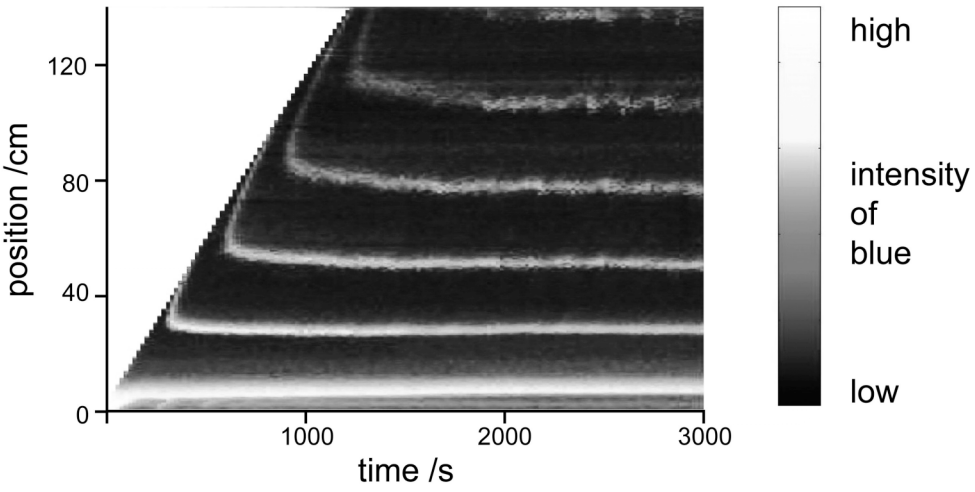

Figure 2.10 Space-time plot of FDO patterns produced with the ferroin-catalysed BZ reaction mixed with agar gel. The inner diameter of the reaction tube was 16 mm.

When the waves had settled, the distance between the first two waves was 19 cm and the distance between the third and fourth waves was 25 cm. This difference can be explained by the warm temperature of the agar solution upon entry into the reaction tube. The agar was warm enough to ensure that no gellation occurred prior to entry into the reaction tube. The agar solution cools as it ascends the reaction tube. The decrease in temperature resulted in an decrease in the frequency of the oscillations[16], which translated to a change in the wavelength (eq 2.1). This temperature gradient is an unavoidable limitation of the agar gel system.

The average measured wavelength for the system was 25.2 ± 5 cm where the large error was due to the decrease in wavelength. The predicted kinematic wavelength for this system was calculated as 27.79 cm, using the linear velocity and the period from the well-stirred BZ reaction. The difference between the calculated and experimentally measured wavelengths can again

be attributed to axial diffusive mixing between fluid packets[8] but also to the presence of agar. The diffusion of BZ reactants in agar gel has been investigated previously[11]. It was shown that the diffusivity of the reactants was unchanged in agar gel when compared to a purely aqueous system. The authors in the same paper suggested the reaction kinetics are unaffected by the presence of the agar gel, however, the period of the reaction has been shown to be sensitive to the presence of chemicals with alcohol groups[17-20]. The presence of these OH groups was suggested to partially inhibit the BZ reaction, but the mechanism of the inhibition has not been fully explained, due to the complexity of the kinetics. Agar gel contains OH groups, which could perturb the reaction kinetics, therefore altering the wavelength of the patterns.

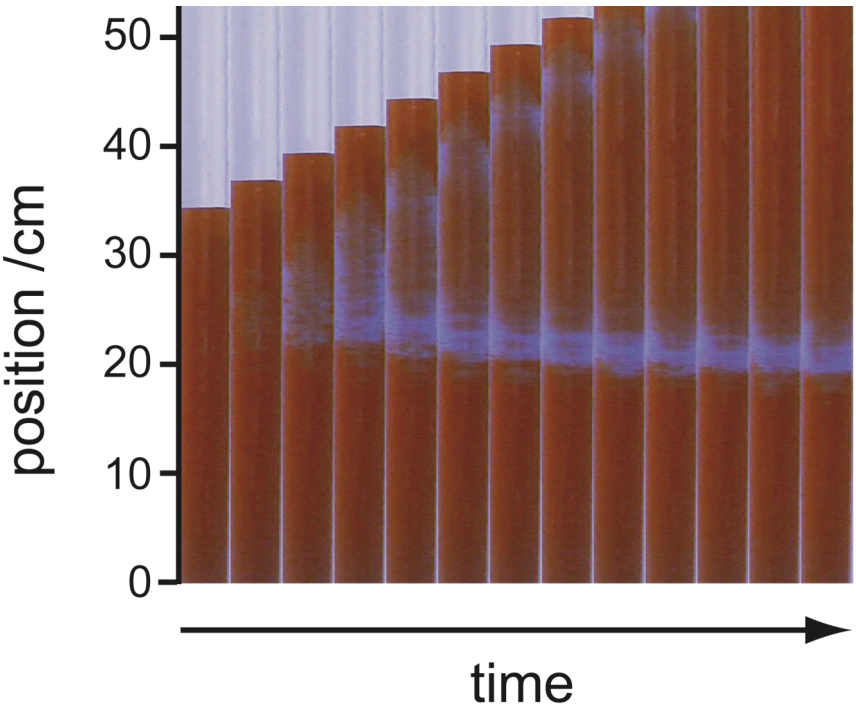

Figure 2.11 A time-series of optical images showing wavesplitting in the ferroin-catalysed BZ reaction with agar. Images were acquired sequentially every twenty seconds. Two blue waves propagate from one excitation point.

The space-time plot confirms the patterns produced in the agar system are stationary after settling to the steady-state position. The formation mechanism for the production of the stationary bands can also be extracted from the space-time plots. The initial band at the bottom of the reactor appeared as the reaction mixture entered the tube. The subsequent waves were produced via the waveplitting mechanism. This is the same mechanism reported previously for the packed bed reactor[3]. A series of optical images showing the wavesplitting mechanism for the agar system is shown in Figure 2.11. A single wave appeared at an excitation point, close to the reacting solution front. This wave then elongated and split into two distinctive waves. One of the waves propagated down to the steady state position. The other wave travelled up the tube, propelled by the flow and out of the reaction tube. The velocity of this wave was 0.15 ± 0.01 cm s^{-1}, and the linear velocity of the fluid was 0.12 cm s^{-1}, showing that the wave propagated faster than the velocity of the fluid. This is because the reaction-diffusion wave was enhanced by the advection.

2.3.6. Control of Flow Distributed Oscillations

The wavelength of FDO patterns was previously shown both theoretically[21] and experimentally[3] to scale with the inverse square root of the BrO_3^- and the H^+ concentration. This relationship is shown in equation 2.2 where λ is the wavelength of the patterns and v is the linear velocity of the reacting solution up the tube.

$$\lambda \propto \frac{v}{[BrO_3^-]^{1/2}[H^+]^{1/2}} \qquad \text{(eq 2.2)}$$

A linear relationship between the concentrations and the wavelength was not observed due to the complex kinetics where the concentrations of all species are interlinked. The wavelength of FDO patterns was also shown to increase linearly with the linear velocity of the reaction solution[3]. This control method would be difficult with the agar system, as the gellation point changes at different flow rates, affecting the stability of the patterns. Control of the patterns via alteration of the concentration of H^+ ions was also experimentally challenging due to the degradation of agar in a low pH medium.

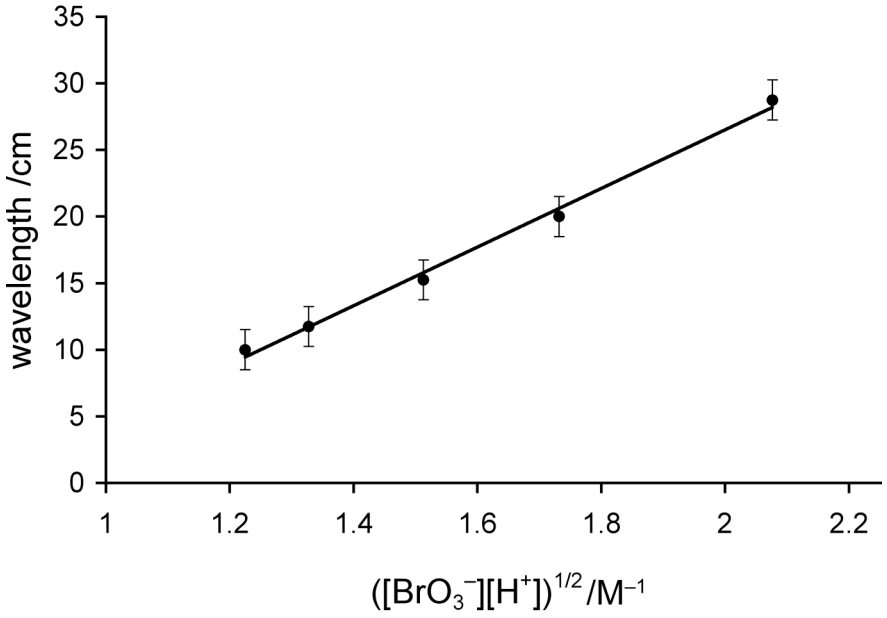

Figure 2.12 A plot showing the wavelength of FDO patterns in an agar gel as a function of BrO_3^- concentration. All other concentrations and experimental parameters were fixed. The temperatures of all reactions were held at 14 ˚C.

To show patterns in the agar system can be controlled in the same way as the packed bed reactor, the initial concentration of BrO_3^- was varied (Figure 2.12). Multiple repeats were conducted and the error bars in the plot were calculated from experimental error. A linear relationship was observed between the wavelength and $([BrO_3^-][H^+])^{1/2}$ for bromate concentrations in the range of 0.12-0.28 M. These experiments showed that the patterns in the agar system can be controlled in the same way as the packed bed reactor in previous investigations[3, 21]. At a concentration of 0.32 M, the system did not produce consistent patterns with an easily measurable wavelength. This was due to a very short wavelength combined with a large volume of carbon dioxide bubbles produced.

2.3.7. Other Gel Systems

Other gel systems were also used to induce plug-flow through a tubular reactor. A similar gel system to agar is agarose, which is a constituent of agar. Agarose was an attractive alternative to agar due to the wide range of gellation temperatures commercially available. The agarose system did produce stationary FDO patterns, which were very similar to the agar system (not shown). The agar system was preferentially used to the agarose system due to the lower costs.

κ-carageenan was also used to generate a plug flow profile. The κ-carageenan system shows similar gellation characteristics to both agar and agarose. The κ-carageenan system, however, was shown to completely inhibit the BZ reaction with no production of patterns.

2.3.8. Pattern Formation in Poiseuille Flow

Packed bed reactors and agar have been used to induce a plug flow profile in order to produce stationary patterns. This was necessary to ensure the phase of the reaction is constant through the width of the reaction tube. Previously, Kaern and Menzinger attempted to produce FDO patterns in a tubular reactor with no packing material[2]. When a Newtonian liquid is passed through a tubular reactor, a parabolic, Poiseuille flow profile is observed[14]. In this profile, the fluid moves at twice the average velocity in the centre of the tube. The velocity gradients in the Poiseuille flow resulted in different reaction phases across the tube. They observed a single band at the bottom of the reactor with no other patterns observed throughout the tube. The lack of any observed subsequent patterns was explained by a mixing of different reaction phases in the reactor via diffusion. Reaction–diffusion waves in Poiseuille flow have been previously been investigated[22]. This study investigated the deformation of chemical waves, not FDO patterns.

Experiments were conducted in the absence of a packing material and agar to re-confirm the requirement for a plug-flow profile for the production of stationary FDO patterns. The space-time plot for these experiments is shown in Figure 2.13.

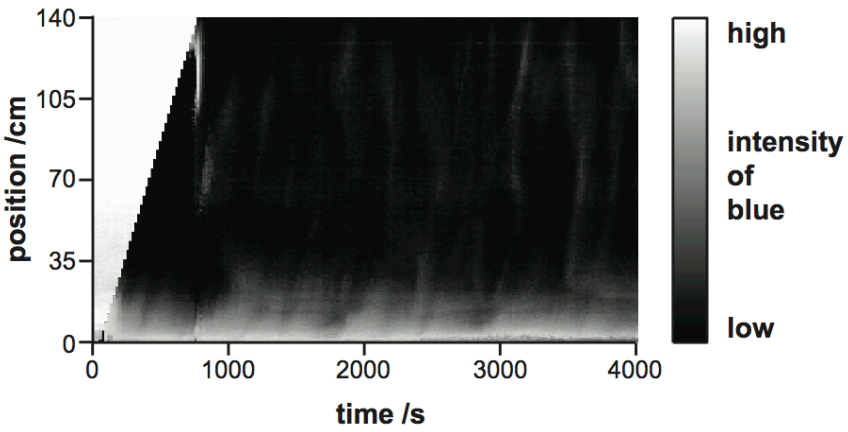

Figure 2.13 Space-time plot for the BZ reaction under flow though a tubular reactor in the absence of a packing material or gel.

A single band at the bottom of the reactor was formed as the tube filled up. This band was previously reported by Kaern and Menzinger[2]. The size of this band varied in size through the course of the reaction, which as not previously reported.

A second band appeared in the reaction tube at 800 s towards the top of the reactor at the reaction/air interface. The spontaneous appearance of the band was followed by elongation and rapid annihilation. Kaern and Menzinger had not previously observed this band. The inner diameter of the reaction tube used by Kaern and Menzinger was smaller than the one investigated in this study, which may explain why it was not observed. After the formation of this pattern, a series of what appear to be chaotic waves were observed in the reaction tube for the duration of the experiment.

The lack of stability of the second pattern can be explained by the mixing of reaction phases due to the parabolic flow profile. In the centre of the reaction tube the reaction could be in a different phase of oscillation to the solution at the walls. These different oscillation phases would mix due to

dispersion, causing the annihilation of the band. These experiments show that a second unstable concentration band can be formed in the absence of a plug-flow profile.

2.3.9. Temperature Control of Flow-Distributed Oscillations

Bamforth *et al*.[3] have previously used chemical concentrations and flow rate to control the wavelength of FDO patterns. Other studies have also shown the effect of changing the boundary conditions at the inlet of the reactor[23-26]. All of these studies change the initial conditions at the inlet of the reactor. To this date no studies have been conducted where the system has been globally forced. The temperature of the entire reaction tube can be controlled in order to observe a global response to a temperature change. Figure 2.14 shows the response of two FDO bands to a global change in temperature.

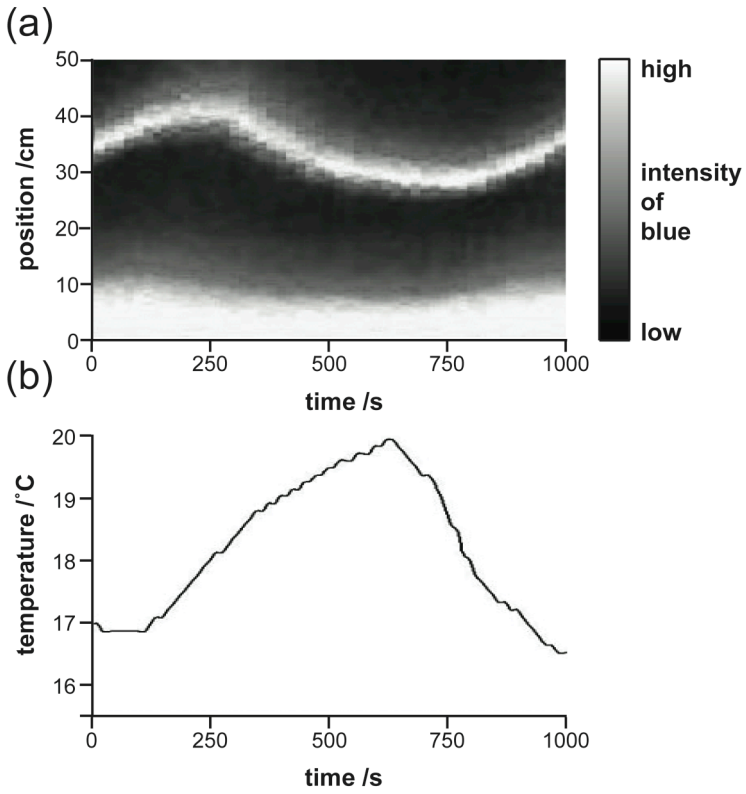

Figure 2.14 (a) Shows a space-time plot of FDO patterns in the ferroin-catalysed BZ reaction under the influence of global temperature changes. (b) Shows temperature change of the reaction tube.

The temperature changes of the reaction tube were monitored during the course of an agar FDO experiment. The effect on FDO patterns of a temperature increase and decrease are shown in Figure 2.14. Initially, the temperature was increased from 17˚ C to 20˚C. Both bands shown in the space-time plot moved down in response to the global temperature increase. This response indicated an inverse relationship between reaction temperature and wavelength of the FDO patterns. This suggested an increase in temperature decreases the period between oscillations, as the linear velocity was maintained.

It has been shown previously that differences in reaction temperature modulate the period of chemical oscillators[27]. An increase in BZ reaction temperature results in a shorter oscillation period. The well-stirred ferroin-catalysed BZ reaction was investigated to see the effect of a temperature change on the period of oscillations.

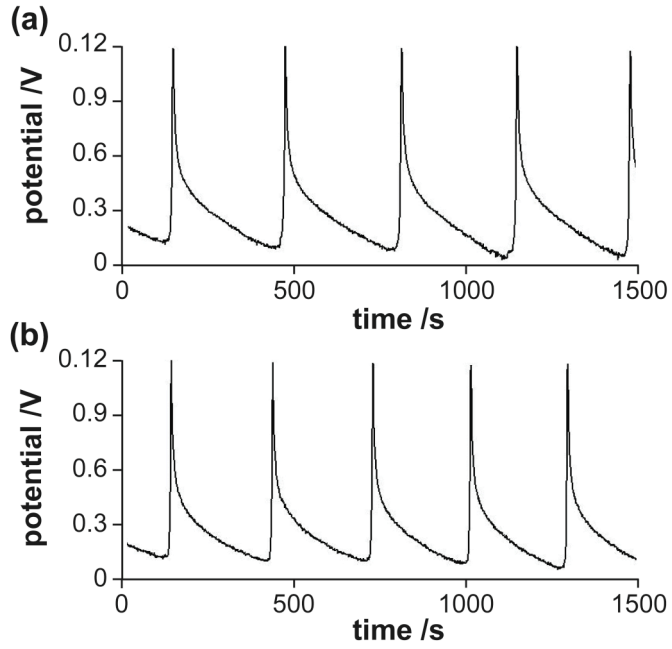

Figure 2.15 Two reaction profiles of the well-stirred BZ reaction over time using a combination Pt-combination electrode. The temperature of the reaction vessel was changed for each experiment. (a) Shows oscillations at 14˚ C and (b) 16˚C.

Figure 2.15 shows the measured potential change for the well-stirred ferroin-catalysed BZ reaction at two different reactor temperatures. The average measured period between oscillations from two repeats of the reaction at 16˚ C was 279.2 ± 2 s. The average period between oscillations for a reactor temperature of 14 ˚C was 330.4 ± 2 s, again from two repeats.

These results show an inverse relationship between reaction temperature and the period between the oscillations. This verified the earlier result where the decrease in wavelength observed for the FDO patterns was the result of a decrease in the period between the oscillations in the well-stirred reaction.

2.3.9.1. Synchronisation of Flow-Distributed Oscillations

Synchronisation is the weak coupling of two oscillators[28]. Synchronisation has been shown in both reaction-diffusion[29] and reaction-diffusion-advection systems by the application of an external force[30, 31]. Experiments such as these have shown that the application of an external parameter such as light[32] can control pattern formation. To this date, there have been no synchronisation studies of the BZ reaction using a change in temperature. Figure 2.16 shows the effect of an oscillating global temperature change of the reaction tube on stationary FDO patterns in the agar system.

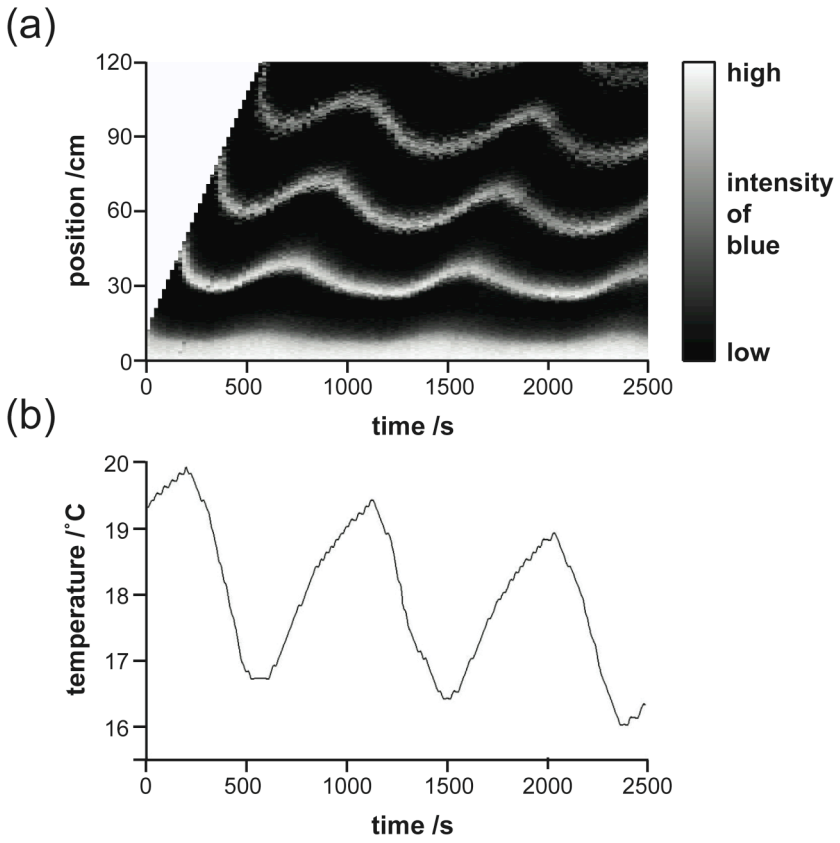

Figure 2.16 (a) A space-time plot of FDO patterns in the agar system. The reaction tube was subjected to an oscillating temperature change over the course of the reaction, shown in (b).

The space-time plot in Figure 2.16 shows the behaviour of FDO patterns when forced by an oscillating reaction tube temperature. The reaction tube temperature is shown in Figure 2.16 (b). The temperature was switched between 20˚ and 16˚ at a forcing frequency of 1000 s. This forcing frequency was approximately three times that of the natural period of oscillation for this FDO system.

The initial band was formed as the reaction solution entered the reaction tube. Three subsequent waves were produced via the wavesplitting mechanism explained previously. The FDO patterns respond to the oscillating temperature by moving up and down. The positional change of the initial

band, at the bottom of the reactor, occurs almost immediately after the temperature change. For increased temperature, the position is lower and for decreased temperature the position of the band is higher. The subsequent bands (the ones higher in the tube) also show a similar response to the change in the temperature. However, unlike the initial band, a phase delay was observed for subsequent bands in response to the temperature change. The second band responded to the temperature change after the initial one and the third one after the second. The phase delay in the response of the subsequent bands to the temperature change can be explained in terms of the linear velocity of the reaction solution. Figure 2.17 (b) shows the position of the top of the four FDO bands over time when forced by the oscillating temperature change. This plot has been annotated with a line, which represents a single fluid packet travelling up the tube at a velocity of 0.188 $cm^{-1}\,s^{-1}$.

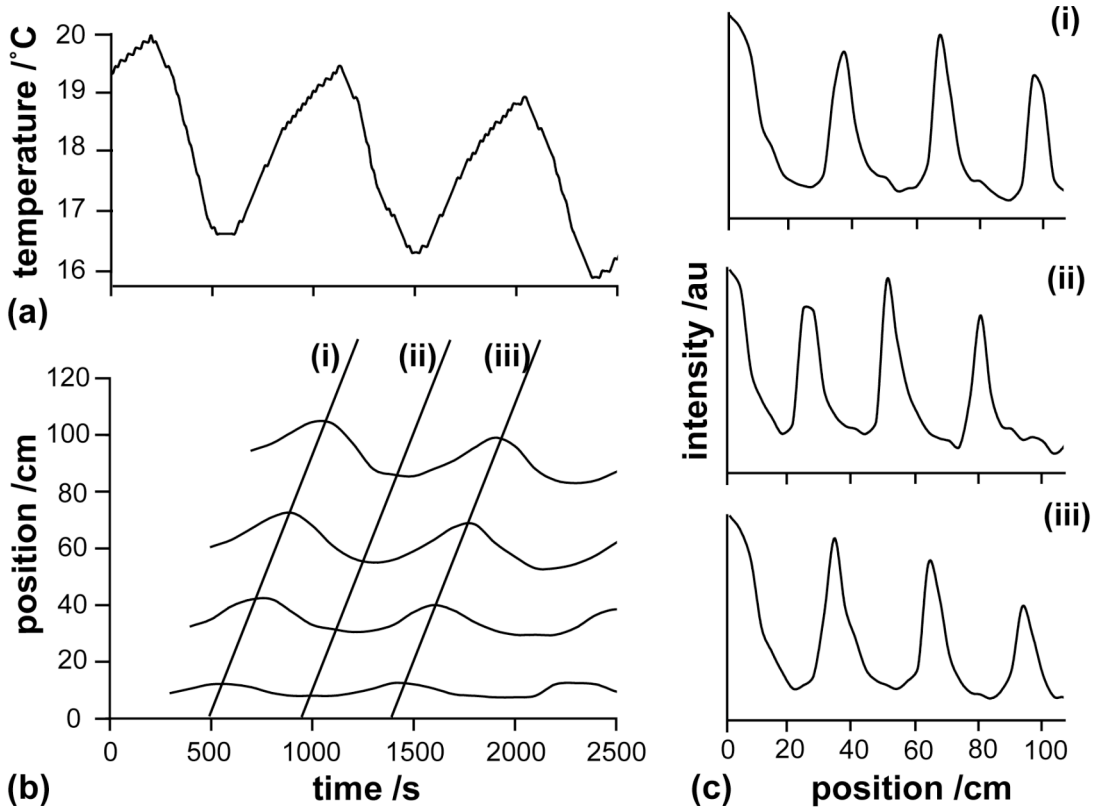

Figure 2.17 Plots showing: (b) the position of the top of the FDO bands plotted out as a function of time. The temperature of the reaction tube is shown in (a). (c) Shows intensity plots extracted from the space-time plot in Figure 2.16 as a function of the linear velocity of the reaction solution. The lines, (i-iii), in (b) show the positions of the extracted intensity profiles.

The flow lines shown in Figure 2.17 (b) indicate the delay in the response of the FDO patterns to the temperature change, can be explained by the velocity of the fluid packets moving up the reaction tube. For example, a fluid packet entered the reaction tube at 500 s, when the temperature of the reaction tube was low (16.5 ˚C). The response to the temperature change can be seen to occur when the fluid packet reaches the bands. The opposite behaviour can be seen for the fluid packet that entered the reaction tube at 925 s at a higher temperature (19.4˚ C). The bands were seen to move

downwards in response to the temperature high as a function of the linear velocity.

Three intensity profiles are shown for the position of FDO bands as a function of the velocity of fluid packets in Figure 2.17 (c) (i-iii). From these intensity profiles, the wavelength of individual fluid packets can be measured. The wavelength when the fluid packet entered at the higher temperature, (ii), was 27.0 ± 1.0 cm and at the lower temperature, (i), 29.5 ± 1 cm. The positional and wavelength change as a function of the linear velocity of the fluid packets showed that the waves were frequency locked to the period of the reaction temperature changes. The result of this was synchronisation in space-time but not time (due to the positional change as a function of the linear velocity). The synchronisation behaviour can be shown in the Lissajous diagrams in Figure 2.18.

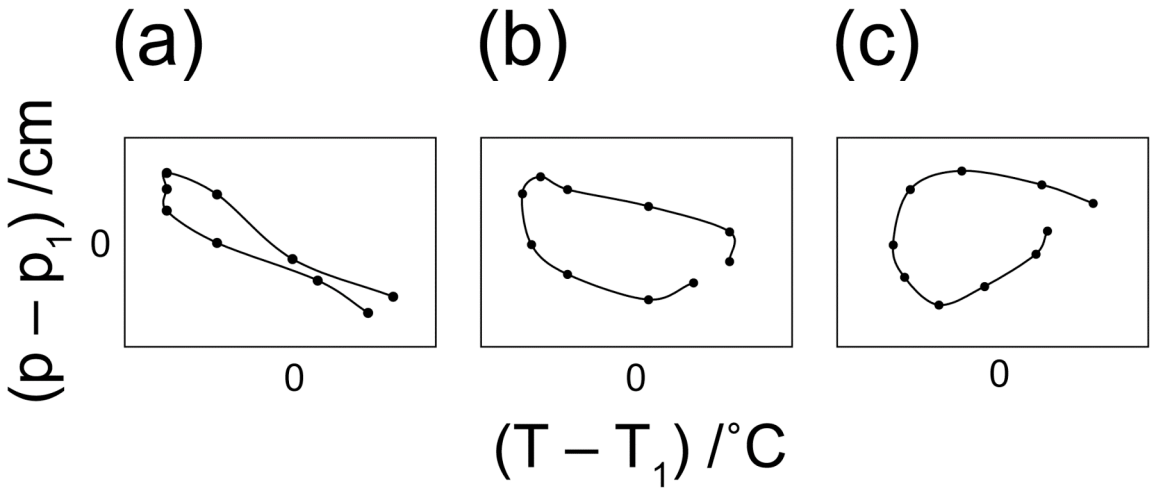

Figure 2.18 Lissajous Diagrams for the first band (b), the second band (b) and the third band (c). p is position and T is temperature

The Lissajous diagrams in Figure 2.18 show the change in the position (p to p_1) as a function of the reactor temperature (T to T_1). The temperature and position data were all taken from 900 to 1800 s. All of the waves were shown to be frequency synchronised i.e. the period of the forcing is identical period of the positional change. The loop is relatively closed for the first wave showing that the phase of the forcing and the response were similar. The loops become progressively larger further from the inlet, showing the delay in the phase to the forcing, i.e. there is a phase delay for subsequent bands.

The lack of observed entrainment in time, is in stark contrast to the large body of research on the light forcing of chemical oscillators[28]. Entrainment has been found for the heterogeneous catalysis of CO, forced with periodic variations of the partial pressure of oxygen[33]. FDO-type patterns have also showed synchronisation by periodic light forcing of the boundary conditions[24]. Crucially, the aforementioned systems all involve the alteration of the rate of reaction of a single step. When the temperature of the BZ reaction is changed all of the reaction rates are simultaneously altered. Some of the reaction steps at higher temperatures are faster and some are slower, with an overall increase in reaction rate that reduces the oscillation period[27]. In conjunction with this, the activation energies of the reactions also change as a function of temperature, further increasing the complexity of the system[34].

2.4. Conclusions

FDO patterns were investigated in a plug flow system without a packing material for the first time. This system put a mixture of agar gel and the Belousov-Zhabotinsky reactants under flow in a pipe reactor.

The ferroin-catalysed BZ system was employed for optical visualisation of the FDO patterns, which were shown to be stationary over time. The optical transparency of the system allowed the defined shape of the patterns to be observed. These patterns were a different shape to the packed bed reactor which have previously been shown to have a canonical shape[5]. The intensity of the bands was shown decrease to further up the tube in the agar system, which was not seen for the packed bed reactor. This was attributed to the agar gel, which adhered to the inside of the reaction tube.

It was shown that the agar system could be controlled by the initial concentration of BrO_3^-, which had previously been used in the packed bed system[3]. It was also found that a temperature variation of the reaction tube could be used to control the wavelength of the patterns. An inverse relationship was found between the wavelength and the temperature.

A periodic change in reaction tube temperature was used to force the stationary FDO patterns in the agar system. Synchronisation was found in space-time as a function of the linear velocity of the fluid. However, synchronisation was not found in time due to a phase delay in the response of the waves to the temperature change. This behaviour was significantly different to other investigations including periodic light forcing of chemical patterns[35]. The response of the FDO patterns was attributed to the complex

kinetics found in the BZ reaction where temperature affects all of the reaction steps[36], inducing complex, anomalous behaviour.

Experiments were performed in the absence of a packing material (Poiseuille flow) to test the necessity of plug flow for the formation of stationary FDO patterns. An initial band at the bottom of the reactor was formed as the reactants entered the tube. Contrary to the previous investigation by Kaern and Menzinger[2], a second, highly unstable band was produced further up the reaction tube.

2.5. References

[1] P. N. McGraw, M. Menzinger, *Physical Review E* **2003**, *68*.

[2] M. Kaern, M. Menzinger, *Physical Review E* **1999**, *60*, R3471.

[3] J. R. Bamforth, R. Toth, V. Gaspar, S. K. Scott, *Physical Chemistry Chemical Physics* **2002**, *4*, 1299.

[4] A. J. Sederman, M. L. Johns, P. Alexander, L. F. Gladden, *Magnetic Resonance Imaging* **1998**, *16*, 497.

[5] M. M. Britton, A. J. Sederman, A. F. Taylor, S. K. Scott, L. F. Gladden, *Journal Of Physical Chemistry A* **2005**, *109*, 8306.

[6] Magritek, Wellington, New Zealand

[7] S. K. Scott, *Oscillations, Waves and Chaos in Chemical Kinetics*, Oxford Science Publications, Oxford, **1994**.

[8] P. Andresen, E. Mosekilde, G. Dewel, P. Borckmans, *Physical Review E* **2000**, *62*, 2992.

[9] A. J. Sederman, L. F. Gladden, *Magnetic Resonance Imaging* **2001**, *19*, 339.

[10] Y. Xia, P. T. Callaghan, *Macromolecules* **1991**, *24*, 4777.

[11] T. Yamaguchi, L. Kuhnert, Z. Nagyungvarai, S. C. Muller, B. Hess, *Journal Of Physical Chemistry* **1991**, *95*, 5831.

[12] R. Yoshida, S. Onodera, T. Yamaguchi, E. Kokufuta, *Journal Of Physical Chemistry A* **1999**, *103*, 8573.

[13] P. T. Callaghan, *Principles of nuclear magnetic resonance microscopy*, Clarendon Press ; Oxford University Press, Oxford [England], New York, **1991**.

[14] J.-L. Peube, *Fundamentals of fluid mechanics and transport phenomena*, ISTE Ltd. ; J. Wiley, London, Hoboken, NJ, **2008**.

[15] P. T. Callaghan, Y. Xia, *Journal Of Magnetic Resonance* **1991**, *91*, 326.

[16] K. KurinCsorgei, G. Nagy, E. Koros, *Chemical Physics Letters* **1997**, *271*, 67.

[17] J. Horvath, Z. Nagy-Ungvarai, S. C. Muller, *Physical Chemistry Chemical Physics* **2001**, *3*, 218.

[18] R. Lombardo, C. Sbriziolo, M. L. T. Liveri, K. Pelle, M. Wittmann, Z. Noszticzius, *Nonlinear Dynamics in Polymeric Systems* **2004**, *869*, 292.

[19] K. Pelle, M. Wittmann, Z. Noszticzius, R. Lombardo, C. Sbriziolo, M. L. T. Liveri, *Journal Of Physical Chemistry A* **2003**, *107*, 2039.

[20] Z. Ungvarainagy, I. Zimanyi, *Reaction Kinetics And Catalysis Letters* **1986**, *31*, 249.

[21] J. R. Bamforth, J. H. Merkin, S. K. Scott, R. Toth, V. Gaspar, *Physical Chemistry Chemical Physics* **2001**, *3*, 1435.

[22] B. F. Edwards, *Physical Review Letters* **2002**, *89*.

[23] D. G. Miguez, P. McGraw, A. P. Munuzuri, M. Menzinger, *Physical Review E* **2009**, *80*.

[24] P. N. McGraw, M. Menzinger, A. P. Munuzuri, *Physical Review E* **2009**, *80*.

[25] P. N. McGraw, M. Menzinger, *Physical Review E* **2005**, *72*.

[26] P. N. McGraw, M. Menzinger, *Physical Review E* **2005**, *72*.

[27] P. Ruoff, *Physica D* **1995**, *84*, 204.

[28] A. Pikovsky, M. Rosenblum, J. Kurths, *Synchronization : a universal concept in nonlinear sciences*, Cambridge University Press, Cambridge, **2001**.

[29] A. F. Taylor, M. R. Tinsley, F. Wang, Z. Y. Huang, K. Showalter, *Science* **2009**, *323*, 614.

[30] M. S. Paoletti, C. R. Nugent, T. H. Solomon, *Physical Review Letters* **2006**, *96*.

[31] M. S. Paoletti, T. H. Solomon, *Europhysics Letters* **2005**, *69*, 819.

[32] M. R. Roussel, J. C. Wang, *Journal of Physical Chemistry A* **2000**, *104*, 11751.

[33] M. Eiswirth, G. Ertl, *Physical Review Letters* **1988**, *60*, 1526.

[34] S. Sen, S. S. Riaz, D. S. Ray, *Journal of Theoretical Biology* **2008**, *250*, 103.

[35] O. Steinbock, *Abstracts of Papers of the American Chemical Society* **1995**, *209*, 233.

[36] J. Z. Zhang, L. Q. Zhou, O. Y. Qi, *Journal of Physical Chemistry A* **2007**, *111*, 1052.

3. Chapter 3 Chemical Patterns in Taylor Vortices

3.1. Introduction

When under flow, further control is gained over the pattern-producing behaviour of the Belousov-Zhabotinsky (BZ) reaction. Taylor vortex flow[1], produced within a Couette cell, provided the opportunity to study the behaviour of chemical patterns in a three-dimensional vortex flow system. Contrary to the magnetohydrodynamic[2-6] methods previously employed, the formation of Taylor vortices requires no specific chemical composition and applied potential to produce the vortex flow. It has been shown that both of these parameters affect the wave propagation velocity.

The three-dimensional propagating waves through the Taylor vortices required an imaging method that can probe the microscopic behaviour within the Couette cell. Optical imaging is able to probe only the macroscopic behaviour of waves through Taylor vortices. Chemical patterns in three-dimensional systems have previously been visualised using magnetic resonance imaging (MRI)[7, 8]. Visualisation of the patterns, using MRI is usually achieved with the manganese-catalysed BZ reaction[7, 9-18]. This is due to differences in the paramagnetism of the oxidised and reduced states of the catalyst.

This chapter reports the investigation of travelling waves produced by the manganese-catalysed BZ reaction in Taylor vortex flow. Initially the flow field was characterised using NMR velocity and diffusion imaging techniques. The parameters for imaging the chemical patterns were optimised with the aid

of T_1 and T_2 relaxation measurements. It was shown that it was possible to monitor the propagation of travelling waves through Taylor vortices using MRI.

The majority of waves propagated via a distributed reaction front mechanism. Propagation velocities were measured for the distributed reaction fronts, which were explained by the data from the NMR velocity and diffusion measurements. In conjunction with this, different propagation behaviour was observed at lower rotation rates within the Couette cell.

3.2. Experimental

All plots shown in this chapter represent results from three experimental repeats unless otherwise stated. The points on the graphs show the average value from the three experiments with the error bars showing the range of the data over the three experiments.

3.2.1. Reagents

Malonic acid (Sigma, Gillingham, UK, 99 %), sodium bromate (Sigma, Gillingham, UK, 99 %), phosphoric acid (Fisher, Loughborough, UK, 85 %), manganese sulfate heptahydrate (BDH, Lutterworth, UK, 98.5 %) and sulfuric acid (Fisher, Loughborough, UK, 98 %) were all used without further purification. Ferroin catalyst/indicator was prepared by dissolving iron (II) sulfate heptahydrate (Sigma, Gillingham, UK, 98 %) and 1,10-phenanthroline (Sigma, Gillingham, UK, 99 %) in a 1:3 ratio in deionised water. All reagents were prepared freshly on the day of the experiment. The solutions were degassed prior to experimentation.

3.2.2. Couette Cell

A schematic diagram of the Couette cell used inside the magnet of the NMR spectrometer is shown in Figure 3.1. The inner cylinder was positioned centrally inside the outer tube. The inner cylinder was connected by a T-piece to the drive shaft, which in turn was rotated by a stepper motor controlled by the Rheo-NMR kit (Bruker).

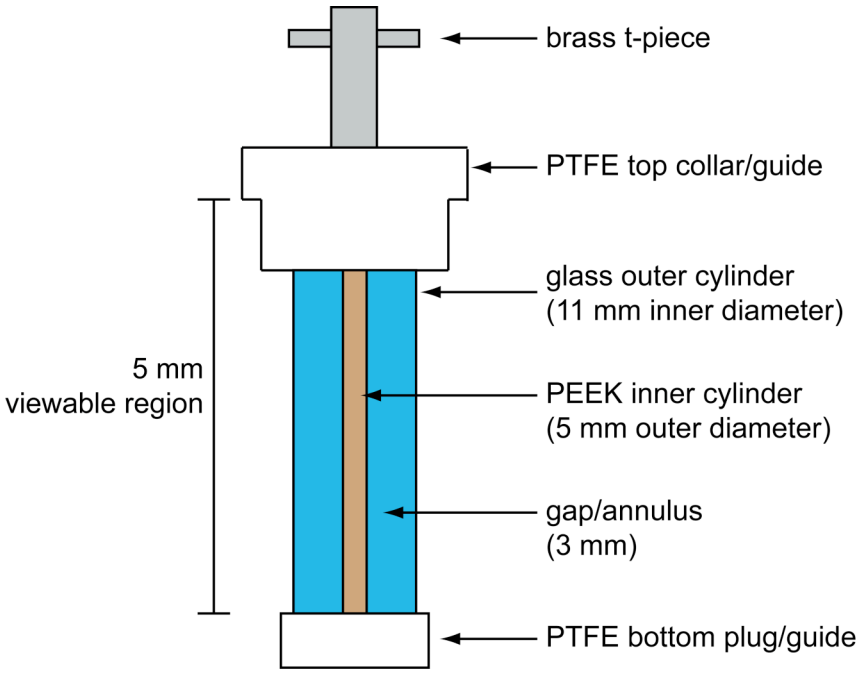

Figure 3.1 Schematic diagram of the Couette cell used for MRI of chemical waves in Taylor vortices.

3.2.3. NMR Experiments

All NMR measurements were performed on a Bruker DMX 300 spectrometer at a proton resonance frequency of 300 MHz. The temperature of the bore was 289.4 K ± 0.5 K. A Micro 2.5 probe was used which consisted

of a birdcage r.f. resonator and water-cooled, triple axis magnetic field gradients with a maximum gradient strength of 100 G cm^{-1}.

3.2.4. Relaxation Measurements

T_1 and T_2 relaxation time measurements were performed on aqueous solutions of both oxidised and reduced states of the manganese catalyst[16]. This was done in order to optimise the parameters for MR imaging experiments.

For the relaxation experiments, a 10 mm resonator was used and XWIN-NMR 2.6 software was used to collect the data. T_1 relaxation times were measured using a T_1 inversion recovery experiment[19]. T_2 relaxation times were measured using a CPMG (**C**arr **P**urcell **M**eiboom **G**ill) experiment[20].

Measurements were made in a 5 mm tube. The Mn^{3+} sample was prepared by making a solution of 6×10^{-4} M manganese sulfate in a mixture of 2.8 M H_3PO_4 and 0.6 M H_2SO_4 (to approximate BZ reaction conditions). A solution of Mn^{2+} was prepared by the addition of 0.05 M $NaBrO_3$ (to oxidise the Mn) to a 6×10^{-4} M manganese sulfate in a mixture of 2.8 M H_3PO_4 and 0.6 M H_2SO_4. Prior to the relaxation measurements, thirty minutes were allowed for the sample to equilibrate to the temperature of the magnet bore. 90˚ r.f. and 180˚ pulse durations were 12 and 24 μs respectively, both with an attenuation of 0 dB. Four signal averages were acquired with 16k complex data points and a spectral width of 10 kHz. The inversion recovery experiments used a variable delay list with τ values logarithmically spaced between 5 μs and 500 ms with a repetition time of a minimum $5 \times T_1$. CPMG experiments, used to

measure T_2, had a variable counter list with values ranging from 0 to 2400 with a repetition time of 7s. τ values were between 1 and 2 ms. Data sets acquired for both experiments were analysed using a combination of Kaleidagraph[21] (Synergy Software, Pennsylvania, USA) and Prospa[22] NMR analysis software (Magritek, Wellington, New Zealand) to obtain T_1 and T_2 relaxation time constants.

Table 3.1 gives the average T_1 and T_2 relaxation times for water protons in solutions of Mn^{2+} and Mn^{3+} from two repeats. The error shows the scatter of the data. Significant differences were measured for relaxation times (T_1 and T_2) of water protons in the presence of Mn^{2+} and Mn^{3+} ions.

	T_1 /ms	T_2/ms
oxidised	375.5 ± 1.0	181.5 ± 4.0
reduced	106.5 ± 1.0	7.8 ± 0.5

Table 3.1 A table showing average relaxation times for water protons in an aqueous acidic solution containing Mn^{2+} and Mn^{3+}. The concentration of manganese in both solutions was 6×10^{-4} M. The average is from two repeats with the error representing the scatter of the data. The data shows the average values with the error showing the spread of the data.

3.2.5. Sample Preparation

For magnetic resonance imaging of chemical waves in a Couette cell, the manganese-catalysed Belousov-Zhabotinsky reaction was used[23]. Three different reaction compositions were used for the travelling wave experiments (Table 3.2).

Reagent	1	2	3
$[Mn]_0$ /M	6×10^{-4}	1×10^{-3}	6×10^{-4}
$[BrO_3^-]_0$ /M	0.05	0.05	0.05
$[Br^-]_0$ /M	0.06	0.05	0.075
[malonic acid]$_0$ /M	0.15	0.2	0.15
$[H_3PO_4]_0$ /M	2.8	1.5	2.8
$[H_2SO_4]_0$ /M	0.6	0.95	0.6

Table 3.2 A table showing the three reaction compositions used for the magnetic resonance imaging of the manganese-catalysed BZ reaction.

Composition 1 was initially used, as it had previously been shown to be suitable for MR investigations of patterns in the BZ reaction[7]. Composition 1, however, was not consistently excitable and sometimes showed oscillatory behaviour. Composition 2[13] was used because it was known to provide MR contrast and also proved to be more repeatably excitable (consistently produced reaction waves). Composition 3 was derived from composition 1 with the Br^- concentration slightly increased, which produced a chemical wave upon triggering (a critically low concentration for the onset of oscillations could not be achieved without an external perturbation). Two stock solutions were prepared prior to the experiments in an aqueous mixture of sulphuric and phosphoric acid. This was so the reactants could be separated and the reaction did not take place. Solution A consisted of malonic acid and sodium bromide. Solution B consisted of manganese sulfate and sodium bromate. The two solutions were mixed together in equal amounts in a conical flask, which was stoppered to prevent the release of bromine gas. Once the malonic acid had been brominated (indicated by a brown to clear colour

change), the reacting solution was transferred to the Couette cell. The Couette cell was placed inside the probe which was in turn placed in the magnet.

For optical imaging of travelling waves in a Couette cell, the ferroin-catalysed BZ reaction was used. Two stock solutions were prepared for the experiment. Solution A consisted of 0.26 M H_2SO_4 and 2.74×10^{-3} M ferroin. Solution B consisted of 0.32 M sodium bromate and 0.52 M malonic acid. The two solutions were mixed in a beaker and transferred to the Couette cell.

3.2.6. Magnetic Resonance Imaging

PARAVISION 2.1.1 software was used to collect the data for travelling wave imaging experiments. Velocity and diffusion maps were acquired using a VISEHS (**V**elocity **I**maging **S**pin **E**cho **H**ard **S**oft)[19] pulse sequence. A RARE (**R**apid **A**cquisition with **R**elaxation **E**nhancement)[24] pulse sequence was used for imaging the travelling waves.

All MRI experiments had the following parameters unless stated otherwise. A Gaussian r.f. pulse was used to selectively excite a 0.5 mm thick vertical slice through the centre of the Couette cell. A time series of the slices were acquired sequentially, one after another. Pulse lengths for the 90˚ and 180˚ r.f. pulses were both set at 1000 μs with a respective attenuation of 12.4 dB and 6.4 dB. The recovery time between each excitation was 100 ms. The spectral width of the experiments was 50 kHz. The echo time was 8.79 ms.

3.2.6.1. MRI of Traveling Waves

Reaction composition 1 was chosen for these experiments. The recovery time between each excitation was 1 s. The echo time was 4.954 ms. The field of view was 50 (vertical) × 25 (horizontal) mm with a matrix size of 256 × 64 pixels resulting in a pixel size of 0.195 × 0.391 mm. The spectral width of the experiments was 100 kHz. To reduce experiment time and increase T_2 contrast a RARE factor of 16 was used. The images were acquired every 4s sequentially one after another.

3.2.6.2. Measurements of Propagation Velocities in Taylor Vortices

A RARE factor could not be used for imaging the BZ reaction under flow due to fluid moving out of the excited slice post-excitation and pre-acquisition. The artefacts appear as ghosting outside of the reaction tube and a decrease in signal within the reaction tube. A single echo was acquired per excitation using a repetition time of 100 ms, this allowed for short experiments while significantly reducing image artefacts. The contrast between the two reaction states was maintained with the new parameters. A combination of both T_1 and T_2 relaxation times provided the contrast for the images.

Reaction composition 2 was used for these experiments. This composition allowed the repeatable production of chemical waves through Taylor vortices. The field of view was 40 (vertical) × 13 (horizontal) mm with a matrix size of 256 × 64 pixels resulting in a pixel size of 0.156 × 0.203 mm.

All chemical wave velocities were measured from the MR image sequences. The position of the waves was measured from signal intensity

profiles vertically (*z*-direction) through the Couette cell. From these profiles, the highest signal intensity from the centre of each wave was measured within an accuracy of ± 1 pixel.

3.2.7. NMR Velocity and Diffusion Measurements

The Couette cell was filled with the same concentration of acidic water (1.5 M H_3PO_4 and 0.95 M H_2SO_4) as reaction composition 2, as to closely approximate the viscosity of the reaction solution. The absence of manganese ions lengthened the relaxation time of the water, making the velocity measurements possible. A VISEHS (**v**elocity **i**maging **s**pin **e**cho **h**ard **s**oft) sequence was used to map both the fluid velocity and diffusion coefficients within the Couette cell. This velocity imaging sequence is the combination of a spin echo imaging and a PGSE sequence. VISEHS consists of a hard 90˚ pulse followed by a soft, slice-selective 180˚ Gaussian refocussing pulse, whose duration was 1 ms with an attenuation of 12.5 dB and spectral width of 3300 Hz. The hard 90˚ excitation pulse was 81 μs with a duration of 0 dB.

All vertical slices had a slice thickness of 1 mm with a field of view of 40 mm (vertical) × 11 mm (horizontal) and a matrix size of 256 × 64 pixels resulting in a pixel size of 0.156 × 0.172 mm. The PGSE gradient parameters used were in the following ranges: Δ = 11 – 60 ms, δ = 1 – 3 ms and $\boldsymbol{G}$ = 0.2 – 0.4 T m^{-1}. The recovery time between excitations was 1 s. PGSE parameters were chosen to provide sufficient phase shift for the velocity maps and sufficient signal attenuation for the diffusion maps. For the velocity measurements, eight $\boldsymbol{q}$ slices (gradient steps) were used with eight

signal averages. For the diffusion maps 16 ***q*** slices were used and four signal averages. The data was analysed using Prospa NMR analysis software and the images were further processed using a combination of Adobe Photoshop and Adobe Illustrator.

3.2.8. Optical measurements

Optical measurements of propagating waves through Taylor vortices were performed using a Couette cell that was 1000 cm long. The cell was made from a glass tube (20 mm inner diameter) with a glass rod (11 mm outer diameter) through the centre. The cell was filled with the ferroin-catalysed BZ reactants as described in section 3.2.5. The Couette cell was set up outside of the NMR magnet so that optical images could be acquired of the reaction tube. The inner cylinder of the Couette cell was rotated by the Rheo-NMR kit (Bruker). Optical images were acquired every twenty seconds with a digital CCD camera (Canon Power Shot A520) which were transferred via USB to a PC.

3.3. Results and Discussion

3.3.1. MRI of Travelling Waves

Initially, measurements of travelling waves in the absence of flow were conducted. A time series of images of travelling waves through the annulus of the Couette cell in the absence of rotation is shown in Figure 3.2. The reacting solution is contained (only) in the annulus and the middle of the cell where the inner rod is located and has no signal. The bright regions are associated with

a high T_2 relaxation time where Mn^{3+} predominates[14]. The dark regions are associated with the presence of Mn^{2+}, which is more paramagnetic and hence the water solvent molecules relax faster and less signal is detected. Multiple waves were initiated from an excitation point at the top of the cell and propagated downwards.

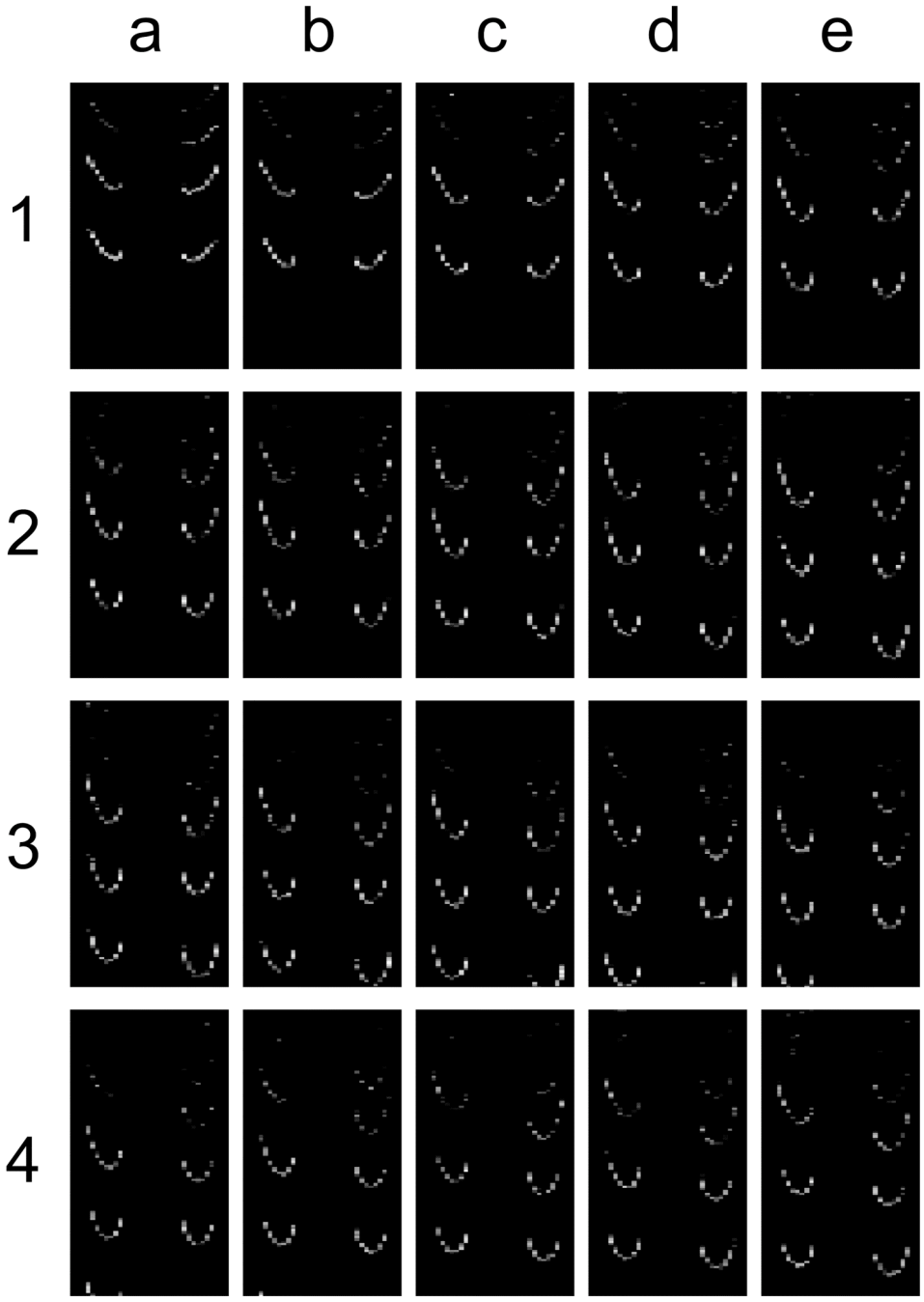

Figure 3.2 A time series of magnetic resonance images of travelling waves in the manganese-catalysed BZ reaction in a Couette cell in the absence of flow. The viewable region was 24 mm (vertical) × 16 mm (horizontal). Each image was acquired in 4s with no delay between acquisitions. The light regions show regions of high Mn^{2+} concentration.

The average propagation velocity for the waves was measured as 0.174 ± 0.010 mm s^{-1}. The error was calculated from multiple repeats of the experiment. The wave propagation velocity in the absence of fluid flow provides a benchmark for the investigation of propagating waves through Taylor vortices.

3.3.2. NMR Velocity and Diffusion Imaging of Taylor Vortices

Quantification of the flow field within the Taylor vortices is essential in order to study reaction-diffusion-advection (RDA) phenomena. Seymour *et al*.[25] previously used NMR velocity imaging to characterise the Taylor vortex flow in the Couette cell. They didn't, however, publish the corresponding diffusion maps. Both velocity and diffusion maps are shown in Figure 3.3 in three directions.

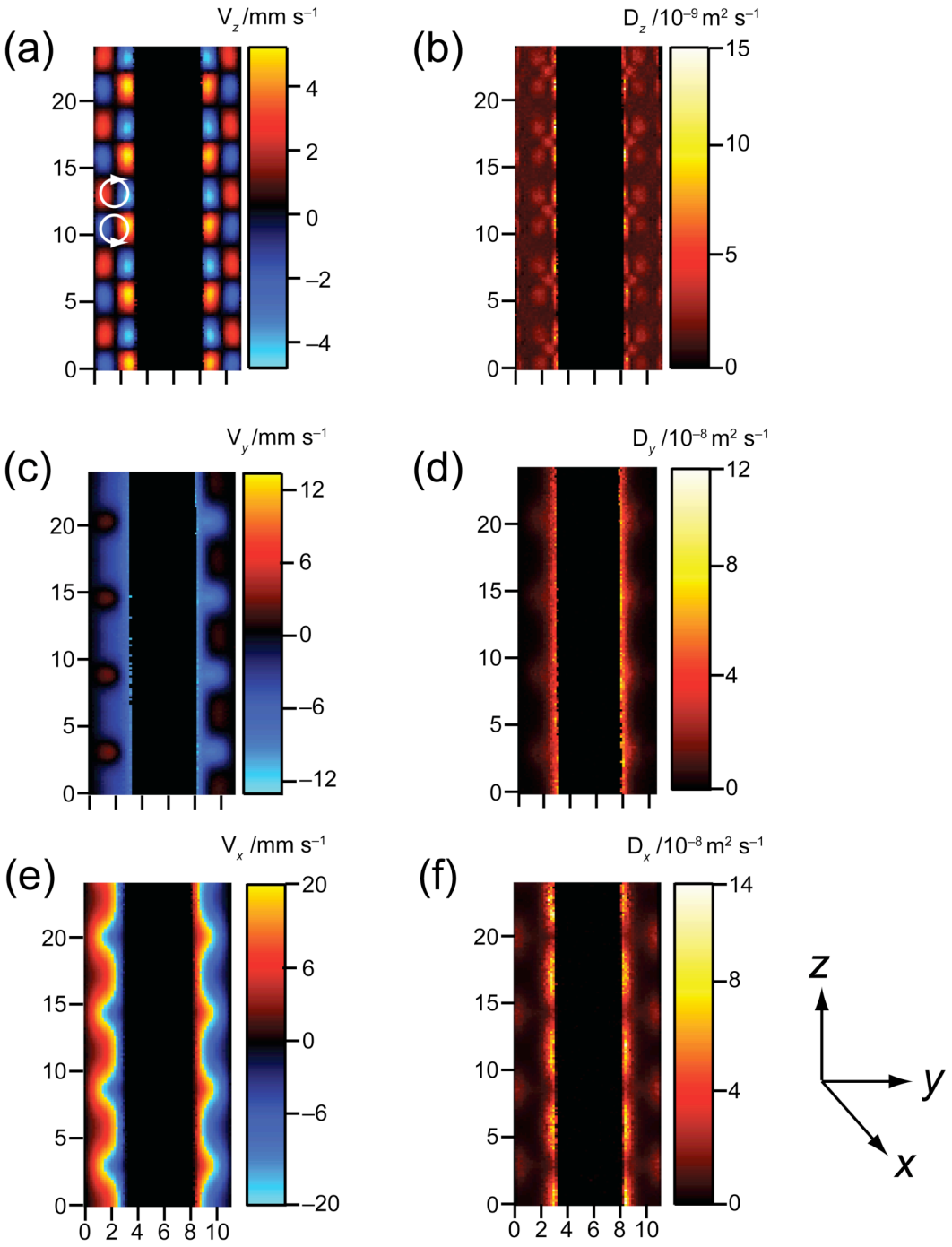

Figure 3.3 Velocity and diffusion maps of Taylor vortices in the Couette cell. The velocities and diffusion coefficients were measured in three directions: *z* ((a) and (b)), *y* ((c) and (d)) and *x* ((e) and (f)). All velocity maps were produced at an inner rotation rate of 3.0 Hz. The white arrows on (a) highlight the rotation of a pair of vortices.

The intensity of the pixels for the velocity and dispersion maps was calculated via propagator analysis, explained in Chapter 1. Positive and negative velocities are represented by yellow/red and white/blue regions respectively with the magnitude of the flow shown by the relevant adjacent bar. For the dispersion maps the adjacent intensity bar shows the magnitude of the diffusion coefficient, where black shows the lowest diffusion and yellow/white shows the highest measured diffusion coefficient.

The *x*, *y* and *z*-velocity maps combined, provide a picture of the flow within the Taylor vortices in three directions for a vertical slice. Both the *y* and the *x*-direction velocity maps show structure, which is indicative of the period of the vortex pairs. The velocity map in the *z*-direction (Figure 3.3 (a)) provides the best picture of the vortex flow within the Couette cell. In this velocity map, the red yellow/red regions indicate upwards flow and blue/white regions indicate downwards flow. One vortex pair has been annotated to show the counter-rotation of adjacent vortices. The size of the vortex pairs was measured as 5.80 ± 0.15 mm in the *z*-direction and 3.00 ± 0.15 mm in the *y*-direction, which makes each singular vortex approximately square. The approximately square aspect ratio is in line with previous studies[1]. A close up view of both the velocity and diffusion maps for one vortex pair is shown in Figure 3.3 where the inner rod is located on the right hand side. The top vortex is rotating clockwise and the vortex beneath is rotating anticlockwise.

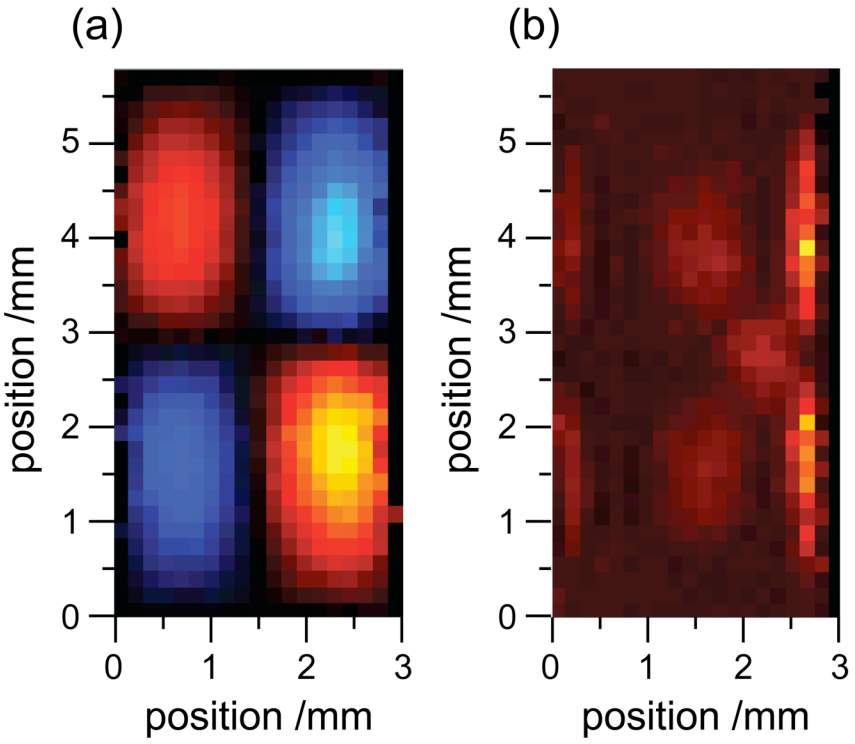

Figure 3.4 One vortex pair extracted from the *z*-direction velocity and dispersion maps. (a) is the velocity map and (b) is the diffusion map. The inner cylinder is located outside of the field of view on the right hand side of the images.

The dispersion map in Figure 3.4 (b) shows the areas of enhanced diffusion where the shear rate is highest in the direction of the applied magnetic field gradient. Enhanced shear is generated by high velocity gradients. Two regions of high dispersion are shown where the vortices rotate against the inner cylinder. Two enhanced dispersion regions with reduced magnitude are observed in opposite positions at the outer cylinder. Enhanced dispersion is observed within each vortex where the difference between upward and downward flow is high. Another region of enhanced dispersion is observed where the two vortices rotate against one another.

The velocity of the fluid within in the Taylor vortices decreases further away from the rotating cylinder which is illustrated in the close up velocity maps of the single pair of vortices in Figure 3.5 (a). Another illustration of the reduction in the velocity of the vortex flow further away from the inner cylinder is shown in Figure 3.5 (b).

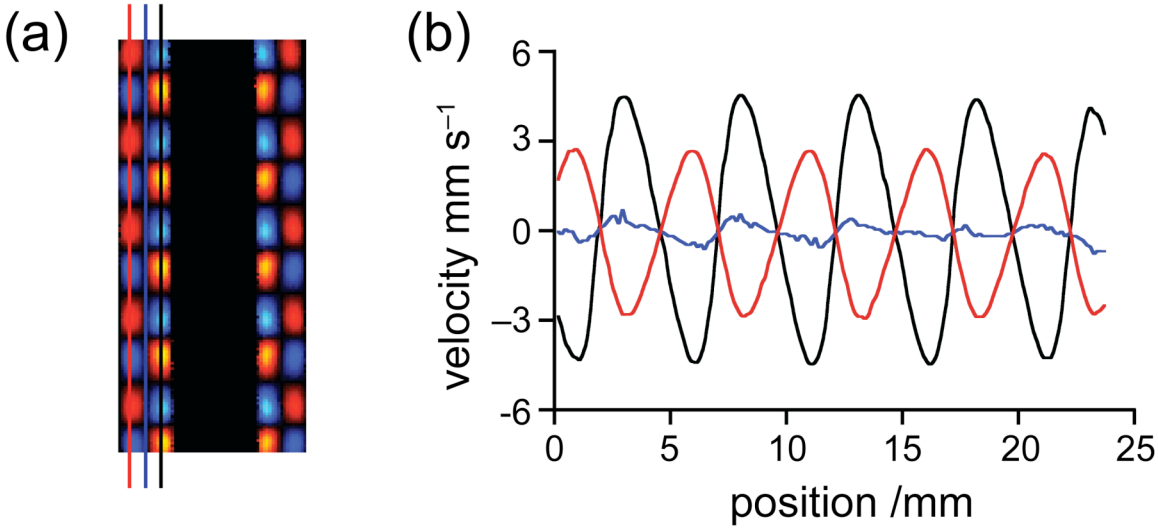

Figure 3.5 (a) Shows a velocity map of Taylor vortices in the z-direction. Three velocity profiles have been extracted (indicated by the coloured lines) and plotted out as a function of position in (b).

Figure 3.5 (b) shows three velocity profiles, which have been extracted from the *z*-direction velocity map (Figure 3.5 (b)) at incremental positions through the annulus and plotted out as a function of position. The black line shows the velocity profile directly next to the inner cylinder where the maximum observed velocity is 4 mm s^{-1}. The velocity profile through the outer part of the annulus (red) shows a maximum velocity of 3 mm s^{-1}, indicating the amplitude of the flow was significantly reduced from 4 mm s^{-1} to

3 mm s^{-1}. The two velocity profiles are mirror reflections for the left and right hand side of the vortices with the low velocity in the z-direction through the centre of the vortices (blue line).

2.6 Hz was the lowest inner rotation rate at which steady Taylor vortices were observed. A series of velocity images were produced from 2.6-4.5 Hz, which show steady vortex behaviour. The inner rotation rate was varied to show the dependence of *z*-direction velocities and diffusion coefficients within the vortices on the rotation rate of the inner cylinder (Figure 3.6).

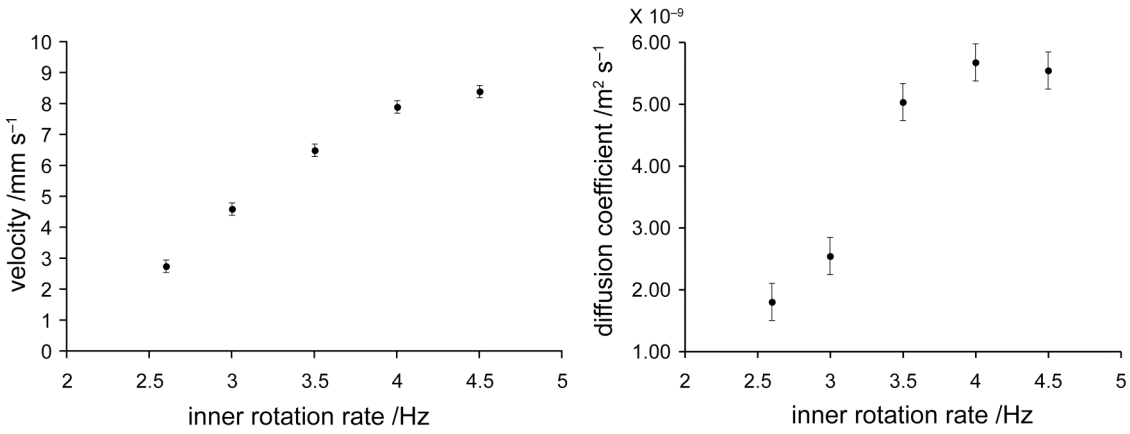

Figure 3.6 Plots showing the maximum velocity, (a), and diffusion coefficient, (b), within the vortices in the *z*-direction as a function of inner rotation rate.

Figure 3.6 (a) shows a plot of the maximum velocity in the *z*-direction against the inner rotation rate. The maximum diffusion coefficient within the vortices in the axial direction is plotted against inner rotation rate in Figure 3.6 (b). A linear increase in the *z*-direction velocity was observed for the rotation rates 2.6 to 3.5 Hz. The diffusion coefficients follow a similar trend to velocities, with an increase in diffusion coefficient as the inner rotation rate is

increased. A change in behaviour of the velocity and the diffusion coefficients was observed for both 4.0 and 4.5 Hz. There is a reduced increase in the maximum *z*-velocity and a small decrease in the diffusion coefficient. There is no apparent change in the shape of the vortices to suggest any change in the vortex flow regime (e.g. wavy vortices) but could possibly indicate a possible transition barrier to another flow regime. This behaviour requires further study but is out of the scope of this thesis.

3.3.2.1. Three Dimensional Visualisation of Taylor Vortex flow

The images presented in Figure 3.3 (a), (c) and (e)quantify the flow field in the *x*, *y* and *z*-directions respectively for a two dimensional vertical slice through the Couette cell. They don't, however, show the torroidal, three-dimensional structure of the vortices. By combining a series of two-dimensional images in the *z*-direction, it was possible to produce three-dimensional reconstructions of the torroidal flow within the Taylor vortices. A series of adjacent vertical slices (13 in total) were produced which were combined to produce a three-dimensional *z*-direction velocity image. Various orientations of the three-dimensional velocity map are shown in Figure 3.7. The void through the middle of the cell shows where the inner cylinder is positioned. Blue indicates negative flow and red indicates positive flow.

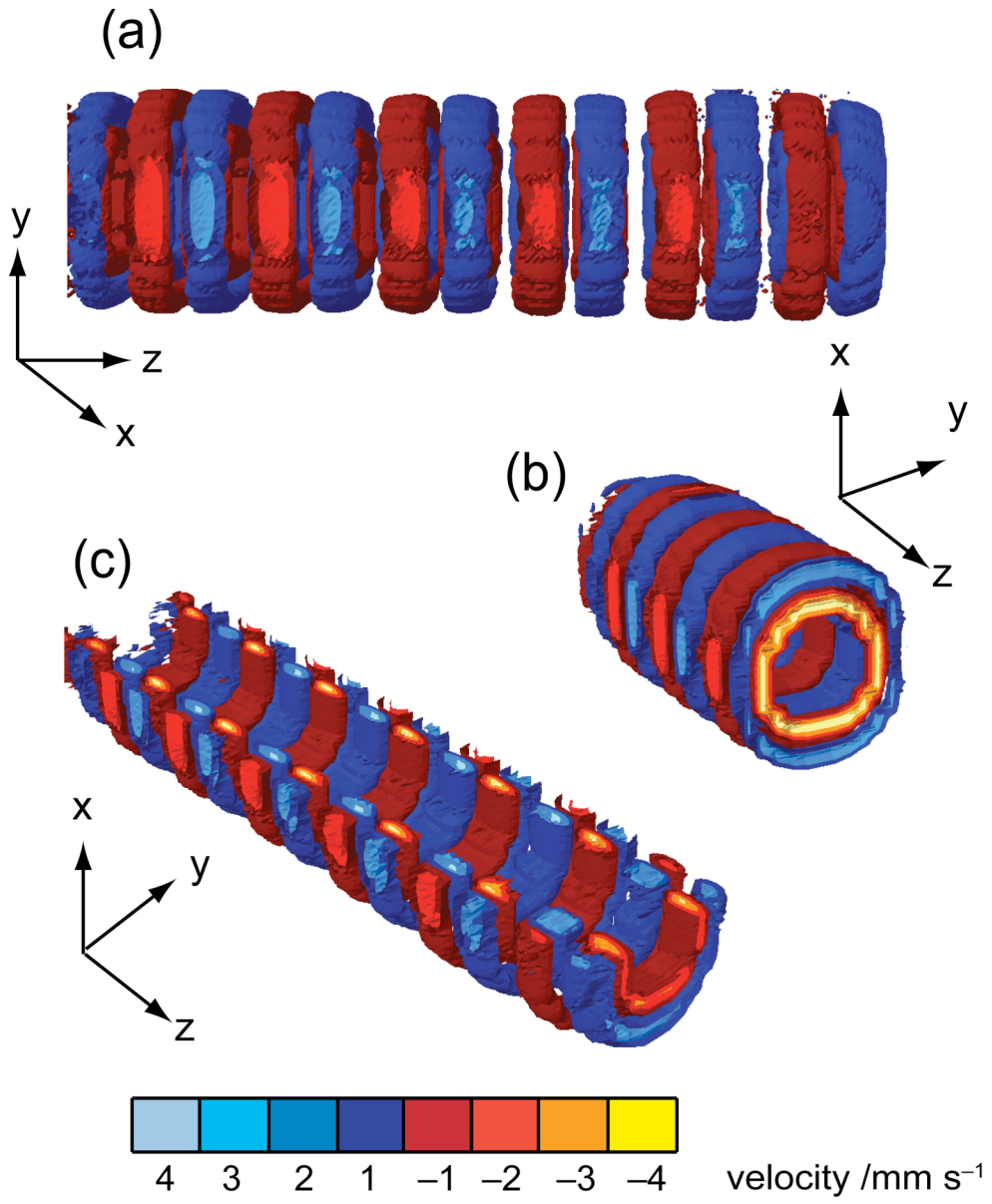

Figure 3.7 (a), (b) and (c) show a variety of orientations of a three-dimensional reconstruction of velocities in the *z*-direction. Integer values, excluding zero, of the velocities were selected ranging from – 4 to + 4 mm s^{-1} and plotted on a three-dimensional axis in layers. The colours of the layers are shown in the bar with the lightest blue colour showing the highest negative velocities and the yellow showing the highest positive velocities

3.3.3. Optical Measurements of Waves Through Taylor Vortices

Figure 3.8 shows a series of optical images of the ferroin-catalysed BZ reaction in a Couette cell. The ferroin-catalysed BZ reaction was used due to superior optical contrast as explained in Chapter 1. The blue areas show a high concentration of ferriin (Fe^{3+}) and the red areas show a high concentration of ferroin (Fe^{2+}).

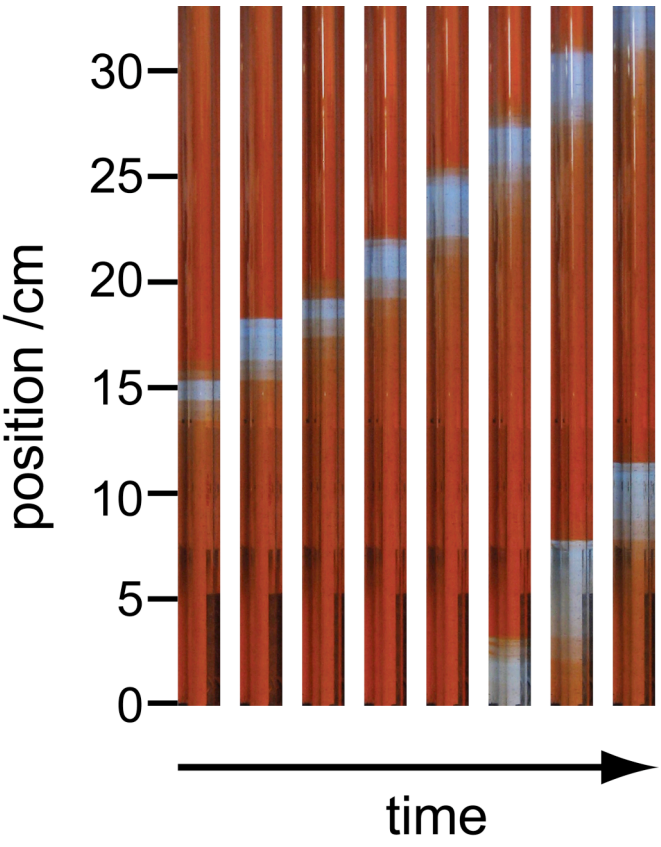

Figure 3.8 A series of optical images of propagating waves through Taylor vortices in a Couette cell. Each image is separated by twenty seconds. The rotation rate of the inner cylinder was 4 Hz. The field of view for each image is 33 cm in height and two cm in width.

Figure 3.8 shows one chemical wave propagating from an initial position of 15 cm. This wave propagated upwards towards the top of the

tube. Another chemical wave is shown at the bottom of the reactor for the final three images, also propagating up the tube. The optical images show a projection through the reaction tube, rather than a slice produced in the MR images. The projection is a sum over the depth of the reaction tube, which makes the structural detail of the chemical wave difficult to infer. The MR images allow the propagation mechanism of the reaction waves to be determined.

3.3.4. Distributed Reaction Fronts in Taylor Vortices

A typical series of images of a reaction wave travelling through Taylor vortices is shown in Figure 3.9. The figure shows the manganese-catalysed BZ reaction in the excitable regime (i.e. produced waves from an excitation point). The bright regions show the water signal in the presence of oxidised catalyst.

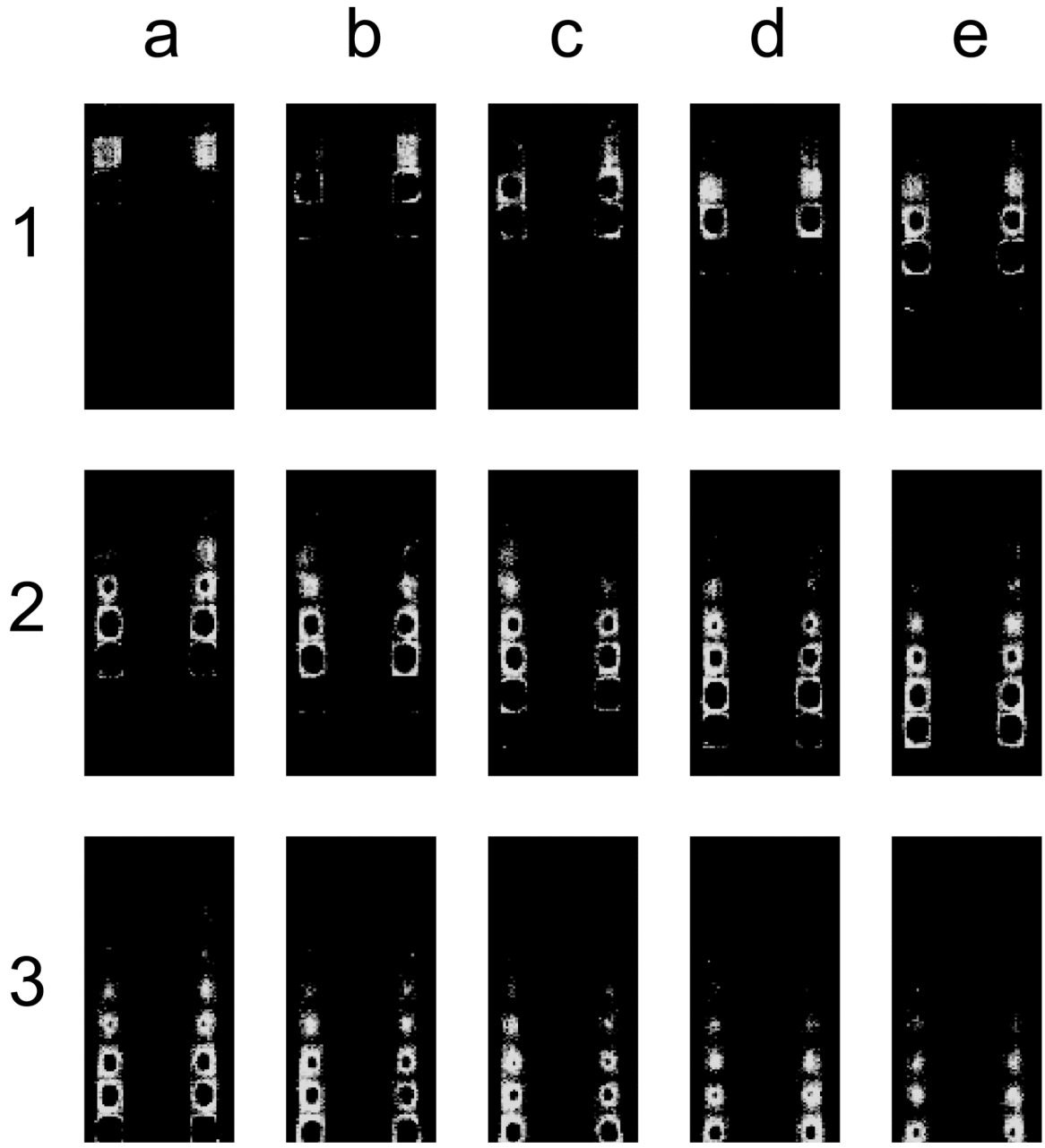

Figure 3.9 A typical series of magnetic resonance images of an excitable BZ reaction wave travelling through Taylor Vortices in a Couette cell. The viewable region is 26 mm (vertical) × 13 mm (horizontal) region of the cell. The rotation rate of the inner cylinder was 3.0 Hz. Each image was acquired in 6.4 s with no delay between acquisitions. The bright areas are indicative of high Mn^{2+} concentration.

Figure 3.9 shows chemical waves were initiated from a single vortex at the top of the cell, which had undergone a bulk oscillation. From this cell, the autocatalytic species diffused into the adjacent cell across the boundary between vortices (the separatrix). When the autocatalyst has entered a vortex cell, it was rapidly transported around the perimeter within the timescale of an imaging experiment (6.4 seconds). Two chemical waves were produced following the spread of the autocatalyst around the perimeter of the vortex cell. One wave travels within a single vortex from the perimeter, inwards to the centre of the vortex. The other wave travels through multiple vortices down the Couette cell.

The wave travelling within the single vortex has previously been explained by Pocheau and Harambat[6] in the two-dimensional vortex system as a purely reaction-diffusion process. The streamlines that carry the autocatalyst towards the centre of the vortex are described as a poor mixing region. It was proposed that the dominant transport process is diffusion across the flow streamlines towards the centre of the vortex cell. The measured propagation velocity of this wave at 3.0 Hz was 0.047 ± 0.020 mm s^{-1}, which is significantly reduced compared to the wave travelling through the multiple vortices (shown below). The relatively large error can be attributed to the limited pixel resolution in the *y*-direction (5 pixels within the annulus).

The propagation of the wavefront down the Couette cell, through the multiple vortices is amplified by the advection, but is limited by the diffusion across the separatrix, as was shown for two-dimensional experiments[6]. The enhancement of propagation velocities is apparent when comparing the velocity of the travelling waves through the vortices (0.636 mm s^{-1} at an inner

rotation rate of 2.6 Hz) and the propagation of waves through the Couette cell in the absence of flow (0.181 mm s^{-1}). The rapid propagation of the chemical wave in the *z*-direction results in the distribution of the reaction across a number of vortices. This specific mechanism of propagating through the vortices has been termed distributed reaction[6] and corresponds to a situation where advection dominates reaction and diffusion. The combination of the two chemical waves results in an overall structure that is composed of a chemical wavefront followed by a wake. This wake consists of a number of autocatalyst-contaminated vortex cells behind the reaction front.

3.3.5. Effective Propagation Velocities

The rotation rate of the inner cylinder of the Couette cell was varied to assess the effect of increased fluid flow on the effective propagation velocity of a RDA wave. A set of typical MR images at multiple rotation rates is shown in Figure 3.10. Degradation in the signal-to noise ratio was observed at higher inner rotation rates due to excited proton nuclei passing out of the slice prior to acquisition. Measurements were also attempted for a rotation rate of 5 Hz. The experiments proved to be difficult to analyse due to poor signal and the rapid rate of the propagation of the waves through the Taylor vortices.

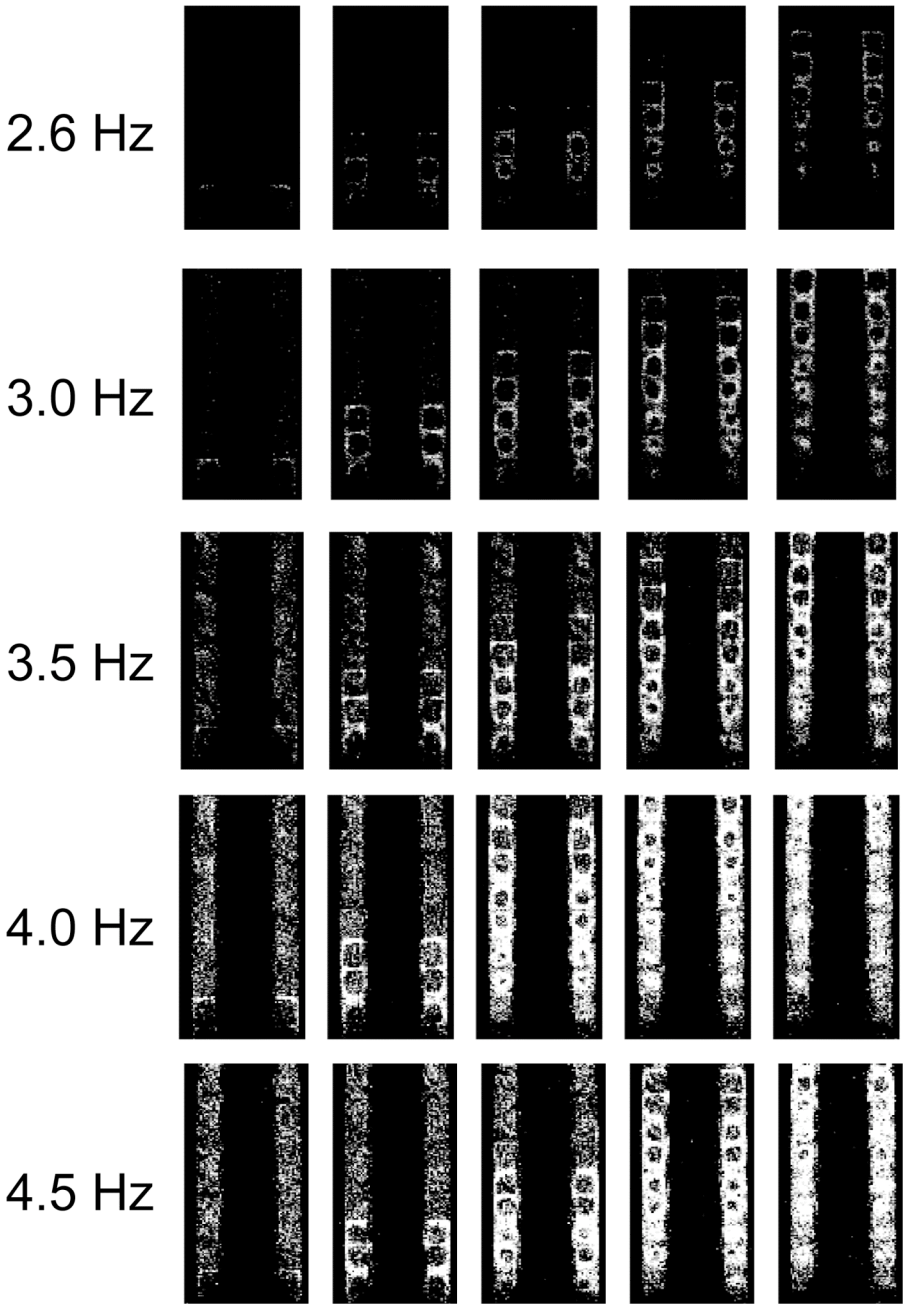

Figure 3.10 A typical series of magnetic resonance images of an excitable BZ reaction wave travelling through Taylor Vortices in a Couette cell at different rotation rates. The viewable region is 26 mm (vertical) × 13 mm (horizontal). Each image was acquired in 6.4 s with no delay between acquisitions. Bright regions indicate high Mn^{2+} concentration.

It is important here to distinguish between propagation velocities and effective velocities. The measurement of reaction diffusion waves was taken

from the tip of the propagating wave. The propagation of the waves through the vortices is more complex due to the rapid propagation of the autocatalyst around the vortices followed by diffusion across the separatrix. An effective propagation velocity can be used to describe the propagation of a wave through a series of vortices. This corresponds to the most progressed point of the wave, disregarding the propagation of waves within the vortices. Figure 3.11 shows the effective front velocity at a series of inner rotation rates from 2.3 Hz to 4.5 Hz.

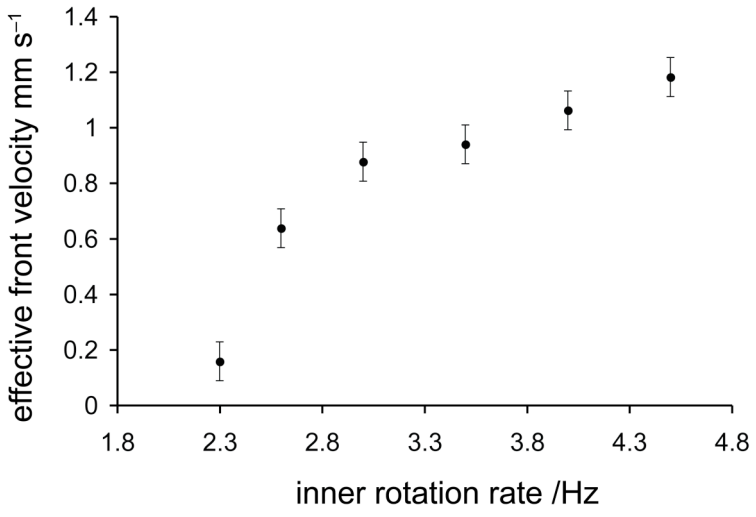

Figure 3.11 A plot showing the effect of inner rotation rate on the effective velocity of travelling waves through a series of Taylor vortices.

The effective front velocity was shown to increase at higher inner rotation rates. This enhancement can be related back to the velocity measurements, where higher fluid velocity within the vortices was found for the increased inner rotation rates. The higher fluid velocity within the vortices at increased inner rotation facilitates faster transport of the chemical waves from one part of the vortex cell to another. Dispersion effects also increase

with inner rotation rate as was shown by the shown previously in Figure 3.6 (b). This results in a more rapid transport of the autocatalyst between vortex cells across the separatrix. These two factors combine to increase the effective front velocity as a function of inner rotation rate. This behaviour has been observed previously for both BZ reaction waves[5] and propagating fronts[6] in planar vortex systems.

In the two-dimensional system, the effective front propagation was shown to increase as a function of the vortex strength, but not linearly[5]. This was also the case for the propagating reaction wave through the Taylor vortices as shown in Figure 3.11[26]. The non-linearity of the relationship was described by the fast-slow nature of the propagating waves through the Taylor vortices, where the fronts are advected by the flow but limited by the diffusion across the separatrix[6]. In the Taylor vortex system, the non-linear relationship can also be explained by the non-linear increase in both fluid velocity and diffusion coefficients as the inner rotation rate was increased.

The effective propagation velocity for a rotation rate of 2.3 Hz was significantly reduced compared to 2.6 Hz. Quantification of the vortex behaviour at a rotation rate of 2.3 Hz was found to be impossible using the velocity imaging technique. This was due to the vortices exhibiting non-steady-state behaviour at this rotation rate. The wave propagation mechanism in the unsteady vortex regime is discussed below.

The wake behind the distributed reaction fronts was also investigated as a function of inner rotation rate. The length of the wake behind the reaction front was predicted for the two-dimensional system by Pocheau and Harambat[6]. Equation 3.1 was used to calculate a theoretical number of cells

within a reaction front (N), where V_f is the effective velocity of the advected wavefront, T_B is the total burning time of one vortex cell and L_X is the length of the vortex cell.

$$N = \frac{V_f T_B}{L_x} \qquad \text{(eq.3.1)}$$

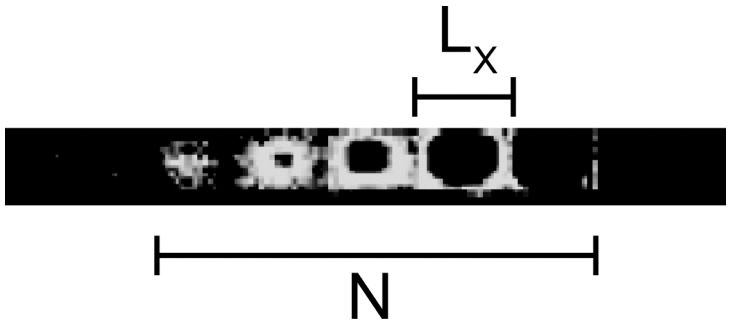

Figure 3.12 A selected region from an MR image of a distributed reaction front showing the size of a vortex pair and the length of the wake. The viewable region is 4 mm (vertical) × 26 mm (horizontal). Bright regions indicate high Mn^{2+} concentration.

The total burning time of the vortices (T_B) is a measure of how fast a reaction diffusion wave propagates within a given vortex cell. The measured T_B values are given in Figure 3.13. T_B decreases with increasing inner rotation rate. If the burning process is a purely reaction-diffusion process, as suggested by Pocheau and Harmabat, the decrease in T_B can be explained by the scaling of diffusion coefficients at increased inner rotation rates.

The number of vortex cells within the wake of a distributed reaction front passing through Taylor vortices was measured experimentally and predicted using eq 3.1. N_{exp} was not measurable for a rotation rate of 4.5 Hz

due to the rapid propagation rate of the reaction wave. Experimental data (N_{exp}) and predicted values (N_{pred}) for the rotation rates between 2.6 and 4.0 Hz are shown in Figure 3.13. N_{exp} increases at higher inner rotation rates, which is explained by both increased vortex flow and increased diffusion between vortices. The inaccuracy of N_{pred} can be explained by the limited temporal resolution of the MR images and could potentially be improved upon future experiments with other rapid imaging techniques such as FLASH[19].

inner rotation rate /Hz	V_f / mm s^{-1} ($\pm$0.003 mm s^{-1})	T_B /s ($\pm$3.2 s)	N_{exp}	N_{pred}
2.6	0.636	32	6	6.70
3.0	0.876	32	7	9.28
3.5	0.938	25.6	7	8.01
4.0	1.061	19.2	8	6.79
4.5	1.181	19.2	–	7.56

Figure 3.13 Table showing, for a range of inner rotation rates, the measured (N_{exp}) and predicted (N_{pred}) number of vortices in the wake of a reaction front. The total burning time (T_B) is also shown for all rotation rates.

3.4. Triggered BZ reaction Waves Through Taylor Vortices

In the previous sections, the BZ reaction was studied in the excitable regime. The excitable regime results in waves, which propagate from (sometimes multiple) excitation points. In a triggerable BZ system, propagating reaction waves appear from an artificially created excitation point. Experimentally, triggerable BZ systems are engineered by an increase in initial Br^- (the inhibitor) concentration. This is done so that the threshold

amount of Br^- required for the onset of a chemical wave cannot be achieved without an external perturbation.

Two triggering systems were produced to initiate BZ reaction waves in the Couette cell. The first system involved the injection of a weak silver nitrate solution into the bottom of the cell. The silver ions in this solution bind to the bromide ions producing a local reduction in the inhibitor concentration by precipitation of insoluble AgBr. The delivery system proved to be experimentally challenging and the presence of the precipitate was unfavourable. The second system used an electrode pair positioned at the bottom of the cell, which allowed an electrochemical reaction to take place, reducing the local bromide concentration. This system exhibited limited reproducibility over five experiments and the electrodes were prone to breakage. Consequently, both systems were not investigated any further.

3.4.1. Other Propagation Mechanisms Observed in Couette flow

Wave propagation mechanisms other than distributed reaction fronts have been observed in the Taylor vortex system. Figure 3.14 shows a series of images with a different propagating front structure than the distributed reaction fronts.

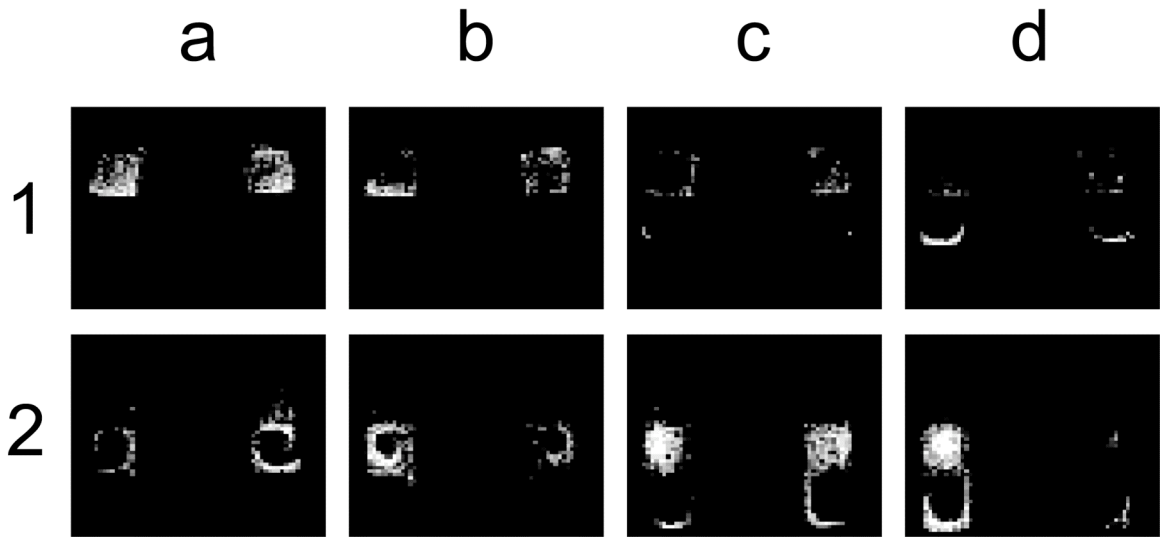

Figure 3.14 A time series of MR images of a propagating finger through Taylor vortices in a Couette cell. The viewable region is 10 mm (vertical) and 13 mm (horizontal). The curvature at the top of the image is due to the inhomogeneity of the magnetic field towards the top of the r.f. coil. The images were acquired in 6.4 s sequentially one after another. The bright areas indicate high concentration of Mn^{2+}.

Figure 3.14 shows the excitation point from which the wave propagated was a vortex cell that had undergone a bulk oscillation. The adjacent vortex cell was contaminated by the same mechanism as the distributed reaction fronts, where the autocatalyst diffuses across the separatrix (1-c). In contrast to the distributed reaction fronts however, the wave does not envelop the vortex cell within the timescale of a single image. The reaction propagated as a finger through the vortex cell in a circular motion following the outer streamlines of the vortex cell. This circular motion continues as the wave propagated towards the centre of the cell producing a spiral-like structure (1-c to 2-b). This propagation mechanism highlights the counter-rotation of adjacent vortices as the finger propagated in one direction through the upper vortex and switched the propagation direction for the next vortex (2-c to 2-d).

The diffusion of the autocatalyst into the separatrix can also be clearly seen in the sixth image (2-b), which is not immediately obvious from the images of the distributed reaction fronts shown earlier.

This finger-like structure has been observed before for both BZ reaction waves[5] and for a propagating front[6] in a two-dimensional vortex system. These structures have been termed flamelets. Flamelet behaviour has also been modelled in the Taylor vortices using BZ reaction waves[26]. This behaviour was observed when diffusion dominated the advection in the Taylor vortices.

The rate at which the flamelet propagated within the vortices was measured. This was achieved by tracing the position of the wavefront within the vortex as a function of time. The radial velocity can be measured when the trajectory of the wave is assumed to be circular. The radius used for the calculations was 1.5 mm, which was extracted from the velocity images in the *z*-direction shown in Figure 3.3 (a). The radial velocity calculated was 0.55 ± 0.05 rad s^{-1}, which equates to a linear velocity of 0.83 ± 0.08 mm s^{-1}. This velocity is greater than the velocity of the waves measured in the absence of flow (0.174 ± 0.010 mm s^{-1}). This shows how the reaction can be amplified by the flow within the vortex cell. The flamelets also consume the vortex cell in a similar timescale to the distributed reaction fronts for the same inner rotation rate (2.6 Hz), which was modelled previously for this system[26]. T_B for the flamelets in the image series above was 25.6 ± 3.2 s and T_B for the distributed reaction fronts was 32 ± 3.2 s.

Flamelets were not consistently observed when the reaction waves propagated through the Taylor vortices. The image sequence shown in

Figure 3.14 was acquired directly after the vortex flow was initiated. This may have resulted in a non-steady-state flow behaviour, giving rise to the anomalous wave propagation behaviour. A change in the kinetics of the reaction may also have resulted in different behaviour. The kinetics of the BZ reaction is extremely sensitive to small temperature changes (Chapter 2)[27] and initial conditions[28].

3.4.2. Travelling Waves Through Unstable Vortices

Using NMR velocity imaging techniques, the lowest steady-state vortex behaviour was observed in the Couette cell at an inner rotation rate of 2.6 Hz. Below this rotation rate some vortex behaviour was observed when propagating waves were imaged, using MRI. Figure 3.15 shows the behaviour of an excitable manganese-catalysed BZ reaction at a rotation rate of 2.0 Hz.

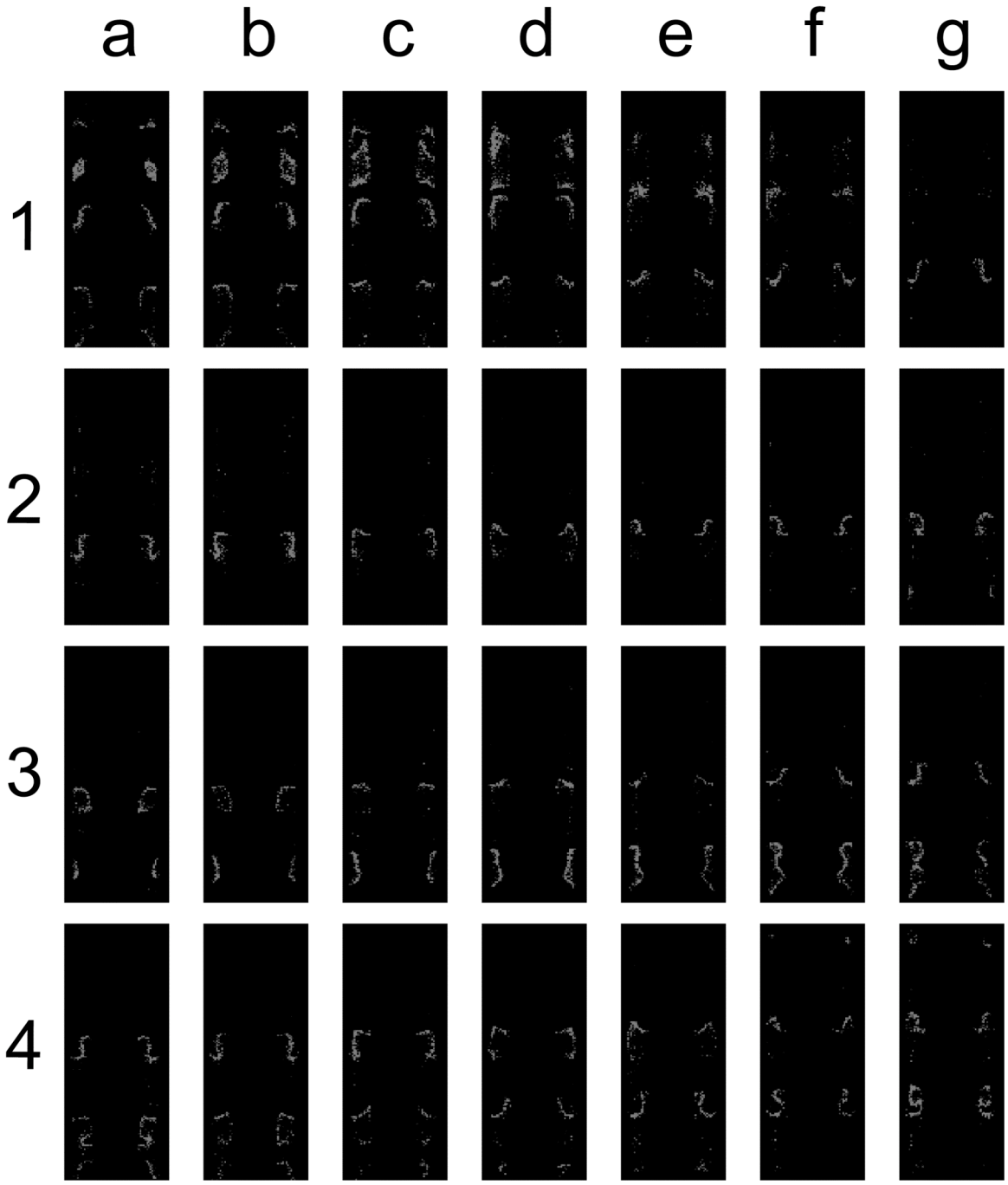

Figure 3.15 A time series of magnetic resonance images of propagating waves through the Couette cell at an inner rotation rate of 2.0 Hz. The viewable region is 28 mm (vertical) × 13 mm (horizontal). The images were acquired in 6.4 s sequentially one after another. The bright regions are indicative of high Mn^{2+} concentration.

In Figure 3.15, two waves can be seen to propagate from an excitation point towards the bottom of the cell. Both of the waves can be seen either side of the inner cylinder. One of the waves propagated downwards out of the field of view and behaved like a reaction-diffusion wave in the absence of advection. Initially, the upward travelling wave propagated as a reaction diffusion wave. However, as the wave moved further up the cell, a distortion was observed, which can be attributed to vortex flow (1-c to 2-c). The wave maintained the width of a purely reaction-diffusion wave in the absence of flow but was wound by the flow to produce s-shaped structures. Mirror reflections of the s-shaped waves were produced in adjacent vortices showing that the flow of the vortices was counter-rotational. Additional structures are shown for the second propagating wave up the Couette cell where the reaction wave had spread over two vortex pairs. The behaviour of the propagating wave could possibly indicate some inconsistent, time-dependent, flow within the vortices.

The behaviour shown in this image sequence has been modelled previously for propagating waves in the Taylor vortices and was termed front wrinkling[26]. In the model, wrinkled fronts were produced at low vortex strength (low flow). This indicated that the flow within the unstable vortices was comparably low.

3.4.3. Flow Manipulation of Propagating Waves in the BZ Reaction

All of the systems described above, study propagating waves through a pre-established flow system. It has been shown that the wave propagation velocity through Taylor vortices can be controlled by alteration of the inner

cylinder rotation rate. What has not been shown, however, is the effect of an imposed flow upon pre-established patterns in the manganese-catalysed BZ reaction.

A series of propagating waves as shown in Figure 3.2 were formed in the Couette cell. Following the onset of the waves, the inner cylinder was rotated at a rate of 2.6 Hz. At this rotation rate, velocity measurements show that steady Taylor vortices were produced in the Couette cell. Figure 3.16 shows the effect of the vortex flow on the propagating waves in the Mn-catalysed BZ reaction. A slight delay was experienced in the initiation of the rotation of the inner cylinder and the acquisition of images. As a result of this, the manipulation of the chemical waves had already commenced.

Towards the top of the cell, a spiral structure was observed with a finger-like wave propagating towards the centre of a vortex (1-e to 2-d). This behaviour is similar to the flamelet behaviour described above and modelled previously[26]. A large spiral structure in the centre of the cell was observed, where a wave was dragged around by a vortex (2-a to 2-d). The pattern formation shown in Figure 3.16 is similar to previous work where an established pattern-producing system is distorted by a superimposed flow field[29]. The images show how a non-linear chemical system can be forced by a non-linear flow system to control pattern formation.

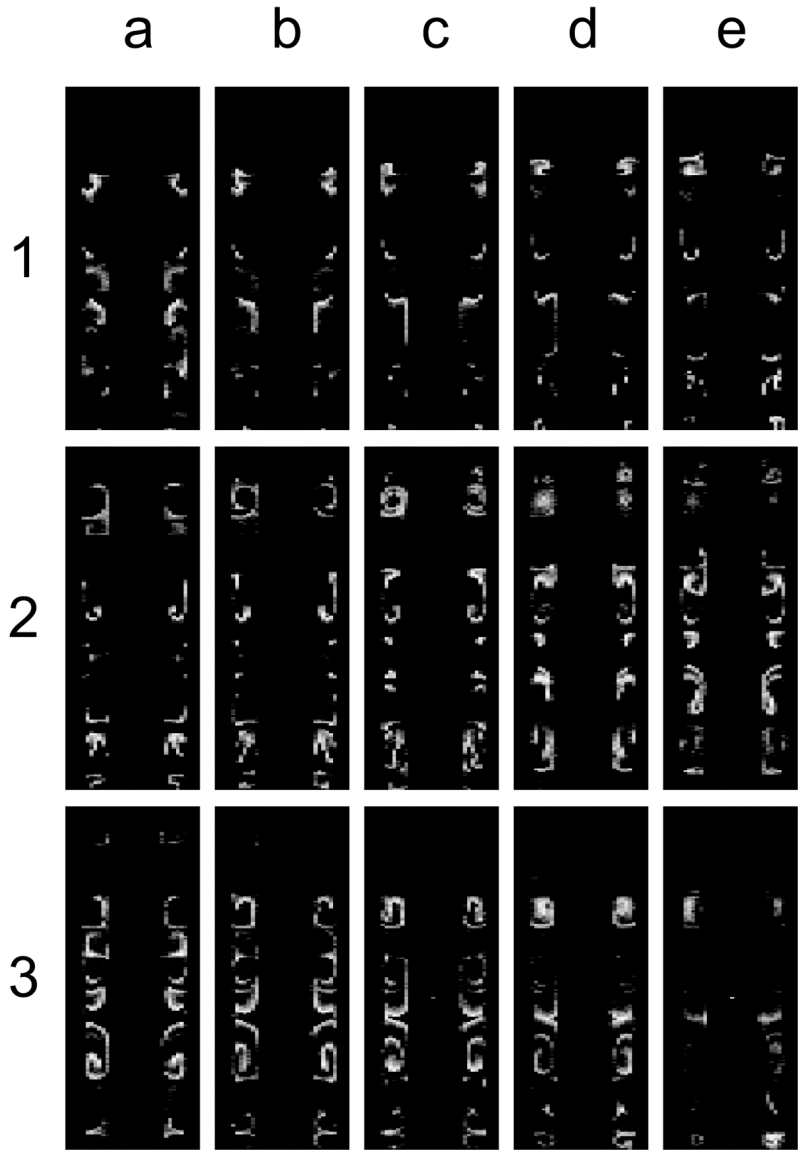

Figure 3.16 A time series of MR images for chemical waves in Taylor vortices. The chemical waves were formed prior to the application of Taylor vortex flow. Each image took 6.4 seconds to acquire. The viewable region is 34 (vertical) × 16 (horizontal) mm. The bright regions correspond to areas of high Mn^{2+} concentration

3.5. Oscillatory Reaction in Taylor Couette Vortices

All of the previous image sequences in this chapter show the propagation of excitable BZ reaction waves through the Taylor vortices. The

behaviour of an oscillatory reaction is significantly different than the excitable regime. An excitable reaction can have multiple excitation sites from which chemical waves can propagate[28]. Oscillatory reactions undergo a complete change of state and do not produce waves from excitation points like the excitable BZ reaction[30]. Figure 3.17 shows typical behaviour of a BZ reaction in the oscillatory regime within Taylor vortex flow. The images in the sequence show some artefacts throughout the reaction tube. This is shown for the fifth image (e) where there is a spatially periodic disappearance of signal at the outer cylinder. This is confirmed by the spatial periodicity of the artefacts being equal to the wavelength of the vortex pairs.

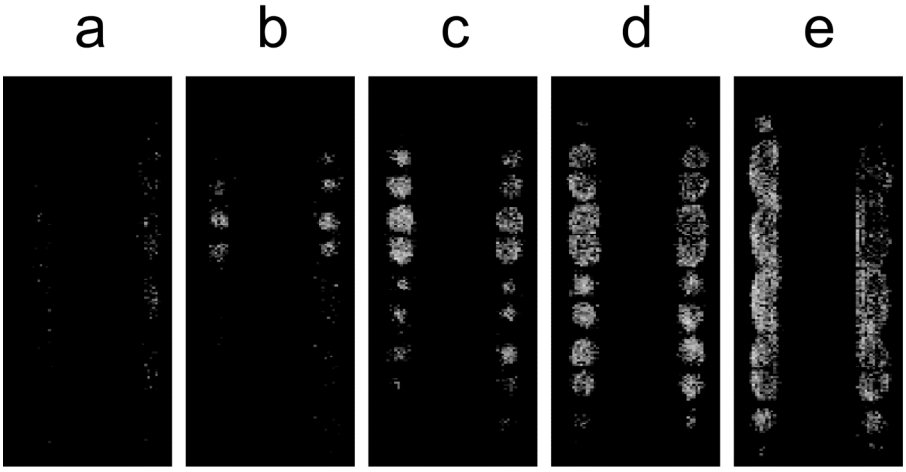

Figure 3.17 A time series of magnetic resonance images of a manganese-catalyed BZ reaction in Taylor vortices in the oscillatory regime. Each image was acquired in 6.4 seconds. The rotation rate of the inner cylinder was 2.6 Hz. Reaction composition 1 was used for these experiments. The observable region in these images is 30 × 13 mm.

The reaction within the Couette cell almost simultaneously switches state, which is indicative of a bulk oscillation. The origin of the reaction state switch was consistently the centre of the vortices. This could be due to an enhanced diffusion coefficient in the centre of the vortex (Figure 3.6 (b)) that increases the rate of reaction[30]. This is the opposite case to the distributed reaction fronts where the waves propagate from the outer part of the vortex towards the centre[26].

The reaction within the vortex pairs appeared to oscillate at the same time with a slight delay between the period between adjacent vortex pairs. This could indicate a variety of conditions in different vortex pairs. As the reaction experiment progressed, a delay was observed, in which different parts of the cell oscillated with a different frequency (not shown). This could be due to different conditions arising in the Couette cell over time[1] including

frictional heating from the rotating cylinder or inhibitory oxygen effects[31] at the reaction/air interface.

3.6. Conclusions

Travelling chemical waves were investigated in a three-dimensional vortex system for first time. Imaging parameters were optimised using both T_1 and T_2 water proton relaxation measurements in the presence of both the oxidised and reduced forms of the manganese catalyst.

The majority of rotation rates studied produced a distributed reaction front propagation mechanism, where advection dominated reaction and diffusion[6]. Effective front velocities were measured for BZ reaction waves through Taylor vortices. The velocity was found to increase non-linearly with rotation rate. This was attributed to the fast-slow propagation mechanism of the distributed reaction fronts, as was shown for the two-dimensional vortex system[5, 6]. The propagation velocities were also explained by the non-linear increase in the velocity and diffusion coefficients as a function of inner rotation rate.

Other wave propagation behaviour was investigated including flamelets and wrinkled fronts. These propagation methods had previously been shown for theoretical studies of BZ reaction waves through Taylor vortices[26]. In a separate investigation, an imposed vortex flow upon an established travelling wave system was shown to produce novel pattern formation.

Optical images were unable to visualise the microscopic behaviour of the BZ reaction waves propagating through the Taylor vortex flow. This research showed that NMR imaging in conjunction with velocity/diffusion

imaging was able to identify regions of high mixing from which the chemical behaviour could be deduced.

3.7. References

[1] E. L. Koschmieder, *Bénard cells and Taylor vortices*, Cambridge University Press, Cambridge [England] ; New York, **1993**.

[2] J. R. Boehmer, T. H. Solomon, *Epl* **2008**, *83*.

[3] M. S. Paoletti, C. R. Nugent, T. H. Solomon, *Physical Review Letters* **2006**, *96*.

[4] M. S. Paoletti, T. H. Solomon, *Europhysics Letters* **2005**, *69*, 819.

[5] M. S. Paoletti, T. H. Solomon, *Physical Review E* **2005**, *72*.

[6] A. Pocheau, F. Harambat, *Physical Review E* **2008**, *77*.

[7] M. M. Britton, A. J. Sederman, A. F. Taylor, S. K. Scott, L. F. Gladden, *Journal Of Physical Chemistry A* **2005**, *109*, 8306.

[8] A. R. Cross, R. L. Armstrong, C. Gobrecht, M. Paton, C. Ware, *Magnetic Resonance Imaging* **1997**, *15*, 719.

[9] Y. Gao, A. R. Cross, R. L. Armstrong, *Journal Of Physical Chemistry* **1996**, *100*, 10159.

[10] A. R. Cross, R. L. Armstrong, A. Reid, S. Y. Su, M. Menzinger, *Journal of Physical Chemistry* **1995**, *99*, 16616.

[11] S. Su, M. Menzinger, R. L. Armstrong, A. Cross, C. Lemaire, *Journal Of Physical Chemistry* **1994**, *98*, 2494.

[12] A. Tzalmona, R. L. Armstrong, M. Menzinger, A. Cross, C. Lemaire, *Chemical Physics Letters* **1992**, *188*, 457.

[13] A. Tzalmona, R. L. Armstrong, M. Menzinger, A. Cross, C. Lemaire, *Chemical Physics Letters* **1990**, *174*, 199.

[14] A. F. Taylor, M. M. Britton, *Chaos* **2006**, *16*.

[15] R. Evans, C. R. Timmel, P. J. Hore, M. M. Britton, *Journal Of The American Chemical Society* **2006**, *128*, 7309.

[16] M. M. Britton, *Journal Of Physical Chemistry A* **2006**, *110*, 2579.

[17] M. M. Britton, *Journal Of Physical Chemistry A* **2006**, *110*, 5075.

[18] M. M. Britton, *Journal Of Physical Chemistry A* **2003**, *107*, 5033.

[19] P. T. Callaghan, *Principles of nuclear magnetic resonance microscopy*, Clarendon Press ; Oxford University Press, Oxford [England], New York, **1991**.

[20] H. Y. Carr, E. M. Purcell, *Physical Review* **1954**, *94*, 630.

[21] www.synergy.com

[22] Magritek, New Zealand

[23] A. R. Cross, PhD Thesis, University of New Brunswick, **1998**

[24] J. Hennig, A. Nauerth, H. Friedburg, *Magnetic Resonance in Medicine* **1986**, *3*, 823.

[25] J. D. Seymour, B. Manz, P. T. Callaghan, *Physics Of Fluids* **1999**, *11*, 1104.

[26] B. W. Thompson, J. Novak, M. C. T. Wilson, M. M. Britton, A. F. Taylor, *Physical Review E* **2010**, *81*.

[27] A. K. Dutt, S. C. Muller, *Journal of Physical Chemistry* **1993**, *97*, 10059.

[28] J. A. P. Irving R Epstein, *An Introduction to Non-Linear Kinetics*, OUP, **1998**.

[29] C. R. Nugent, W. M. Quarles, T. H. Solomon, *Physical Review Letters* **2004**, *93*.

[30] S. K. Scott, *Oscillations, Waves and Chaos in Chemical Kinetics*, Oxford Science Publications, Oxford, **1994**.

[31] O. Steinbock, C. T. Hamik, B. Steinbock, *Journal of Physical Chemistry A* **2000**, *104*, 6411.

4. Chapter 4 Chemical Patterns in a VFR

4.1. Introduction

So far, stationary flow-distributed oscillation (FDO) patterns have been produced in both a packed bed reactor[1-3] and in a pipe reactor with the addition of agar gel (Chapter 2). Both of these systems are used to induce a plug-like flow. Other systems, such as steady Taylor vortex flow with superimposed axial flow, can be used to induce plug-like flow[4]. This flow regime, termed vortex flow reactor (VFR)[5], forces the Taylor vortices to drift up the reaction tube. There is still open debate in the literature with regards to this flow system. Kataoka[4] claimed the VFR was able to produce a perfect plug flow (within certain experimental parameters) but the drift velocity of the vortices has since been shown to be slower[5, 6] or faster[7] than the axial flow. Where the vortices travel slower than the axial flow, there must be a flow through or around the vortices known as by-pass flow[5, 6]. The by-pass flow mechanism is still poorly understood and requires further study. It has also been shown that the size of the vortex pairs is altered at different inner rotation rates[8].

This chapter reports the investigation of FDO patterns in a VFR. Optical images of the reaction tube were produced using the ferroin-catalysed BZ reaction. The effect of inner rotation rate on the structure, stability and wavelength of patterns produced in the system has been investigated and related back to the flow within the system. Comparisons were drawn between results in the VFR, packed bed, and agar experiments, which show that the flow field can be used to explain the behaviour of the patterns within the VFR.

Patterns produced with the manganese-catalysed BZ reaction were investigated in the VFR. This work was conducted to lay the foundation for future magnetic resonance investigations of the patterns.

4.2. Experimental

All plots shown in this chapter represent results from three experimental repeats unless otherwise stated. The points on the graphs show the average value from the three experiments with the error bars showing the range of the data over the three experiments.

4.2.1. Reagents

Malonic acid (Sigma, Gillingham, UK, 99 %), sodium bromate (Sigma, Gillingham, UK, 99 %), phosphoric acid (Fisher, Loughborough, UK, 85 %), manganese sulfate heptahydrate (BDH, Lutterworth, UK 98.5 %), penta-sodium triphosphate (Fluka, Gillingham, UK, 98%) and sulfuric acid (Fisher, Loughborough, UK, 98 %) were all used without further purification. Ferroin catalyst/indicator was prepared by dissolving iron (II) sulfate heptahydrate (Sigma, Gillingham, UK, 98 %) and 1,10-phenanthroline (Sigma, Gillingham, UK, 99 %) in a 1:3 ratio in deionised water (Elga Process Water, Marlow, UK). All reagents were prepared freshly on the day of the experiment. The solutions were degassed prior to experimentation. Reactants for the Belousov-Zhabotinsky reaction were separated into two stock solutions for the experiments to prevent the onset of the oscillations prior to mixing.

4.2.2. Vortex Flow Reactor

A schematic diagram of the VFR is shown in Figure 4.1. The outer tube had an inner diameter of 16.5 mm. An inner tube, with an outer diameter of 6.5 mm, was placed inside the tube. PTFE guides were used at the top and the bottom of the cell to ensure the inner rod rotated centrally with minimal deviation. The inner cylinder was connected by a T-piece to the drive shaft, which in turn was rotated by a stepper motor controlled by the Rheo-NMR kit (Bruker, Germany). The VFR had a small inlet at the bottom to allow reactants to enter the tube with minimal residence time. This was to ensure the phase of the reaction remained constant at the inlet of the reactor. A larger outlet at the top of the reactor was used to remove the waste products without pressure build up. The inner cylinder was rotated at the desired frequency prior to the reactants being pumped into the tube. Following this, solutions A and B were pumped into a continuously stirred tank reactor (CSTR) of volume 3 cm^3 using a peristaltic pump (Ismatec, Glattbrugg, Switzerland). From the CSTR, the mixture was passed, via capillary (1.3 mm inner diameter and <10 cm long) into the reaction tube. The residence time in both the capillary tube and the CSTR was less than 30 seconds. Typically, the reaction tube temperature was maintained at 22 ± 0.5 ˚C, unless otherwise stated.

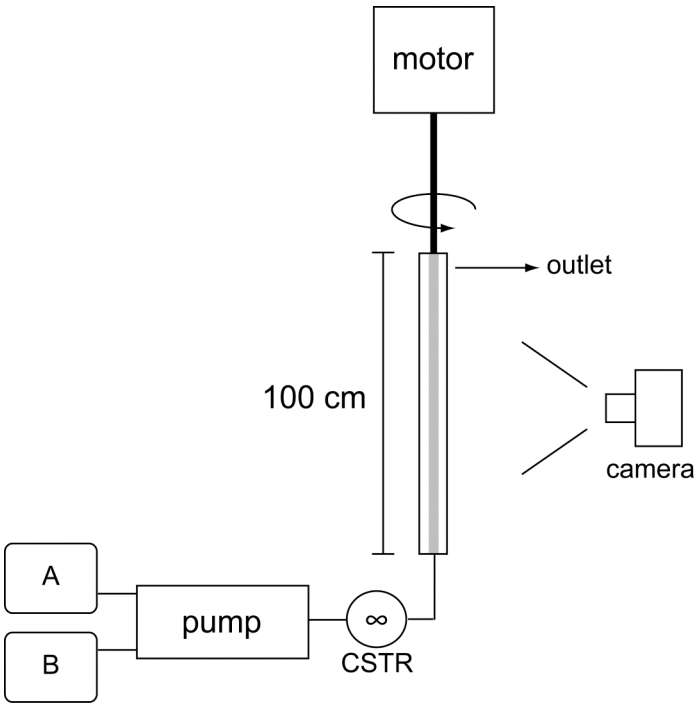

Figure 4.1 Schematic diagram showing the vortex flow reactor setup. A and B represent the two stock solutions for the BZ reaction.

4.2.2.1. Ferroin-Catalysed Belousov-Zhabotinsky Reaction

The ferroin-catalysed Belousov-Zhabotinsky reaction was used for optical imaging of patterns in the VFR. Solution A consisted of [malonic acid] = 0.52 M and [sodium bromate] = 0.4 M. Solution B consisted of $[H_2SO_4]$ = 0.26 M and [ferroin] = 9.35×10^{-4} M. The rotation rates studied were in the range: 1.25 - 2.3 Hz. Typically, the reactions were conducted at a volume flow rate of 12 cm^3 min^{-1} unless stated otherwise.

4.2.2.2. Manganese-Catalysed Belousov-Zhabotinsky Reaction

The manganese-catalysed Belousov-Zhabotinsky reaction was also used for optical imaging of patterns in the VFR. Solution A consisted of

[$MnSO_4$] = 5×10^{-4} M and [H_2SO_4] = 0.06 M. Solution B consisted of [BrO_3^-] = 0.125 M, [malonic acid] = 0.125 M and [penta-sodium triphosphate] = 5×10^{-4} M. A small amount of ferroin was added to the reaction to increase the optical contrast between the two reaction states. The volume flow rate was 4 cm^3 min^{-1} for the optical images.

4.2.3. Well-Stirred Belousov-Zhabotinsky Reaction

Temporal oscillations were studied in the well-stirred ferroin-catalysed Belousov-Zhabotinsky reaction. The two prepared stock solutions were mixed and placed into a temperature-controlled vessel. The reaction was vigorously stirred by a magnetic follower, which was driven by a magnetic stirrer (IKA, Staufen, Germany). The potential difference was used to monitor the reaction over time with a Pt-combination electrode using a Picoscope Oscilloscope (Picotech, Cambridge, UK) and the Picotech software (Picotech, Cambridge, UK). The reaction temperature was maintained at 22 ˚C ± 0.5 ˚C by a water jacket, which was controlled by a water bath (Huber, polystat cc3, Chippenham, UK).

4.2.4. Optical Measurements

Optical measurements were acquired of chemical patterns, produced by both the ferroin and manganese-catalysed BZ reaction, in a VFR (refer to Figure 4.1). Optical images were acquired in less than a second with a delay of twenty seconds between acquisitions, using a digital CCD camera (Canon

Power Shot A520), which were transferred via USB to a PC. Space-time plots were produced using the same method as Chapter 2.

4.3. Results and Discussion

4.3.1. Well-Stirred Belousov-Zhabotinsky Reaction

The oscillatory ferroin-catalysed BZ reaction was chosen as the appropriate chemical system for the observation of chemical patterns in a VFR. Temporal oscillations in the ferroin-catalysed BZ reaction were measured using potentiometric methods. A typical plot of the temporal oscillations for the chosen reaction composition is shown in Figure 4.2.

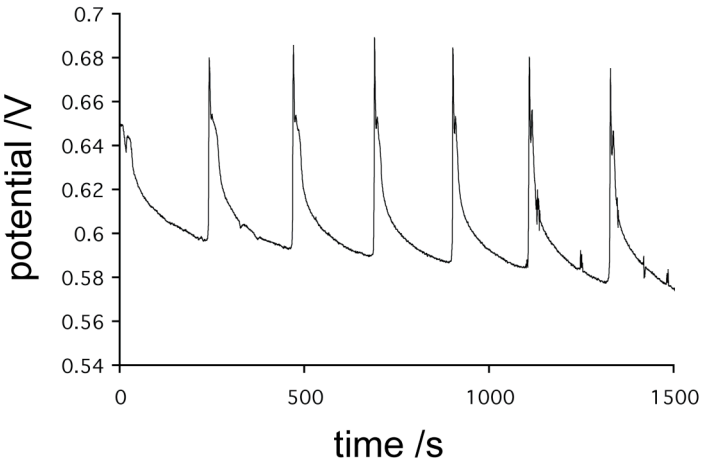

Figure 4.2 Plot showing potentiometric measurements of temporal oscillations in the well-stirred ferroin-catalysed BZ reaction.

Oscillations between the oxidised (ferriin) and reduced (ferroin) state of the catalyst are shown by the peaks and troughs respectively. The induction period was shown to be 250 s, which was a suitably short for observation of

chemical patterns in the VFR. The period between the oscillations was measured from the peak-to-peak distance as 207 to 227 s, which was suitable for the dynamics of the patterns to be observed.

4.3.2. Chemical Patterns in a Vortex Flow Reactor

Vortex flow reactors have previously been proposed as ideal plug flow reactors[4]. However, subsequent studies have shown the flow to be more complex. These complexities include the presence of inter-vortex by-pass flow through or around the vortices[5, 6] and an alteration of the size of the vortices at different inner rotation rates[8]. These changes in the flow field as a function of the parameters provide an interesting medium in which to study flow-distributed patterns.

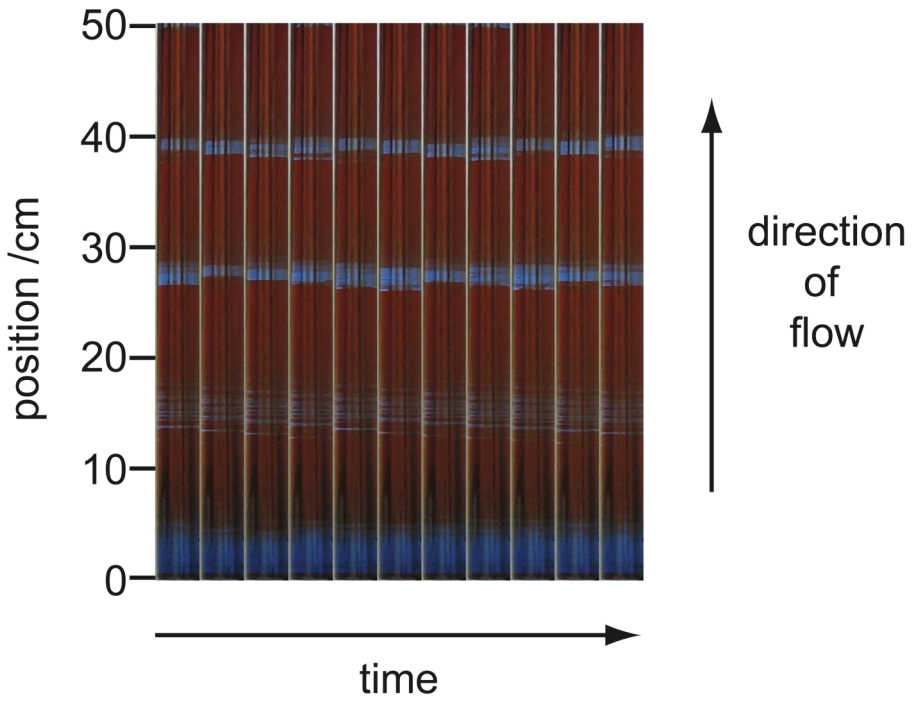

Figure 4.3 A time-series of optical images of chemical bands in a VFR produced with the ferroin-catalysed BZ reaction. Images were acquired

sequentially with a delay of twenty seconds. The temperature was 23 ˚C. The rotation rate of the inner cylinder was 1.75 Hz.

Figure 4.3 shows a time series of optical images of the ferroin-catalysed BZ reaction in a VFR. The transparency of the reactor allowed the outline of the glass inner cylinder to be observed through the outer tube. The fluid within the reaction tube was mainly red, which was indicative of high ferroin (Fe^{2+}) concentration. Defined blue bands were observed though the reaction tube, which indicated high concentration of ferriin (Fe^{3+}). The initial pattern at the bottom of the reactor was larger than subsequent bands. In the well-stirred reaction, the residence time in the ferriin state is longer for the induction period, which could account for the larger pattern at the inlet. This phenomenon could also be explained by the flow at the inlet of the VFR, where the vortices have been reported as larger[5]. This increase in size is due to the inflow of the reactants through the small inlet. Larger diameter vortices at the inlet of the reactor, filled with ferriin catalyst, could account for the larger band observed. The second pattern centred at 15 cm had a diffuse structure, which will be discussed further in section 4.3.5. The third and fourth patterns are positioned at 28 and 39 cm respectively.

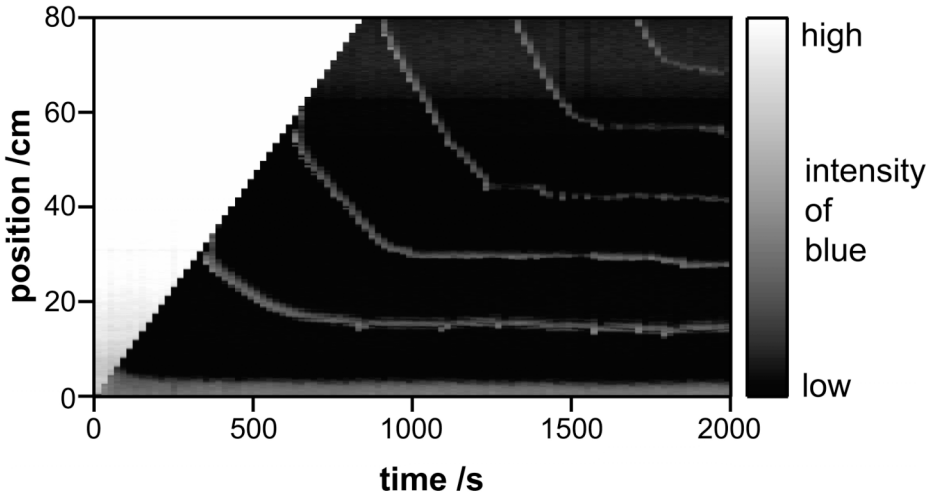

Figure 4.4 A space-time plot showing the development of stationary FDO patterns in a VFR. The inner rotation rate was 2.0 Hz.

Figure 4.4 shows a space-time plot for a typical FDO experiment in a VFR. The period from 0 to 800 s shows the tube filling with BZ reactants. The high intensity regions correspond to increased ferriin concentration (high intensity of blue). An initial band formed immediately at the bottom of the reactor when the reactants entered the tube. The formation of this initial band was via the same mechanism as previously observed for both the packed bed reactor and the agar system. During the experiment, five subsequent bands were formed which settled to steady-state positions. Once the bands had settled, both the optical images and the space-time plot show the chemical bands formed in the VFR are periodic through space. These bands remain stationary over time, therefore fulfilling the criteria for formation of stationary FDO patterns[10]. The formation of the FDO bands showed the vortex flow within the VFR does not prevent the formation of stationary FDO patterns. The flow within the vortices and increased axial dispersion within the VFR could possibly have hindered the formation of the FDO bands. The flow within

this system is significantly different to the agar system, which was shown by velocity and diffusion measurements to be close to perfect plug flow.

Comparisons can be drawn between the bands in the VFR and those observed in both the packed bed reactor[2, 3, 11] and the agar system (Chapter 2). The optical contrast between the two oxidation states of ferroin is comparable to the agar system and superior to the packed bed reactor. This is due to the optical transparency of the agar and VFR systems, whereas the packed bed has inferior contrast due to the optical opacity and reflectivity of the glass beads.

4.3.3. Chemical Pattern Formation in a VFR

FDO patterns have previously been formed in packed bed reactors and the agar system by a mechanism termed wavesplitting[3]. Wavesplitting involves the formation of an excitation point, which produces two propagating waves. One propagates up, which is propelled by the flow out of the tube. The other wave propagates against the flow to a steady state position. The mechanism by which bands in the VFR system were formed was different to both the packed bed reactor and the agar system. A typical series of optical images showing the formation of FDO bands in the VFR are shown in Figure 4.5.

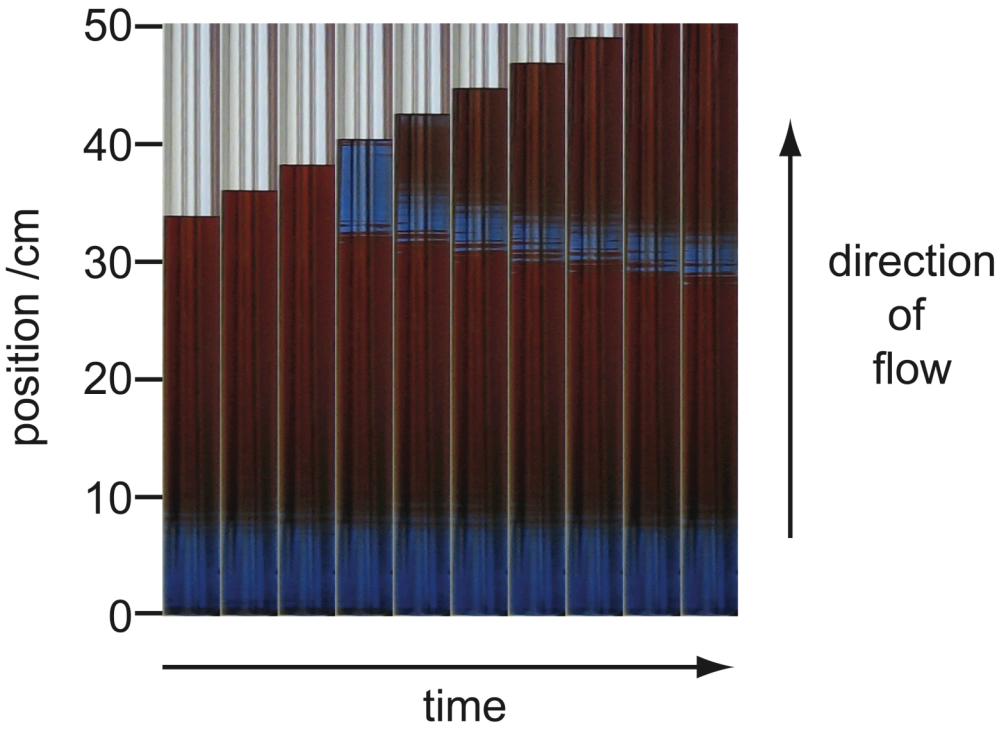

Figure 4.5 A time-series of optical images showing the formation of a stationary FDO band in the VFR. Images were acquired sequentially with a twenty second delay.

Bands in the VFR form at the top surface of the reaction solution as it fills the reactor. From the surface of the reaction solution, the bands propagate down and slowly settle at the steady-state wavelength. Because the excitation point is at the reaction solution/air interface, no band was seen to propagate upwards, as was seen for the packed bed and agar systems.

In the VFR system, the reaction solutions are pumped into an empty reaction tube. This results in a reaction solution/air interface, which is persistently disturbed by rotation of the inner cylinder. The stirring would increase the uptake of oxygen from the atmosphere into the reaction solution[12].

Oxygen inhibition of the reaction could possibly be used as an explanation for lack of any wavesplitting behaviour. Dissolved oxygen has previously been shown to affect both the induction and oscillation periods of the BZ reaction[13, 14]. The general consensus in the literature is that molecular oxygen, found in the atmosphere, inhibits BZ oscillations[12].

Uptake of oxygen into the reaction solutions could therefore increase the period between oscillations in the VFR. The time between the formation of wavesplitting excitation points has previously been described by the period between oscillations in the well-stirred reaction[3]. The period between the formation of the first, second and third excitation points was measured as 280 ± 5 s, which is longer than the measured period for the well-stirred reactions (207 to 227 s). The well-stirred reaction was conducted in a sealed container, so the discrepancy could be explained by oxygen inhibition in the VFR.

The period between formation of subsequent excitation points (fourth, fifth etc..) was found to be longer than the first three at 370-420 s. The amount of dissolved oxygen at the top of the reactor could be greater than at the bottom due to the reaction solution/air interface being stirred for longer. This could alter the excitation point formation period for the bands produced later in the reaction. The oxygen inhibition could also be combined with the age of the reaction solution, where pattern dynamics have been shown to change as the reaction becomes older[15].

This formation mechanism of the bands was found to be consistent for all rotation rates studied. The period between excitation point formation for bands further up the tube was found to be consistently longer at all rotation rates studied.

The formation mechanism in the VFR has not been observed in previous FDO systems. In the packed bed system, the reactor is pre-filled with sulfuric acid so the reaction air interface is found only at the top of the reactor. This would not affect the formation of patterns further down the tube. As for the VFR system, the agar reaction solution is pumped into an empty reaction tube. However, the agar system has no stirring effects from the inner cylinder to encourage the dissolution of oxygen from the atmosphere.

The propagation velocity of settling waves was investigated as a function of rotation rate (Figure 4.6). The plot shows the average settling velocities for the first three waves after formation, excluding the initial band.

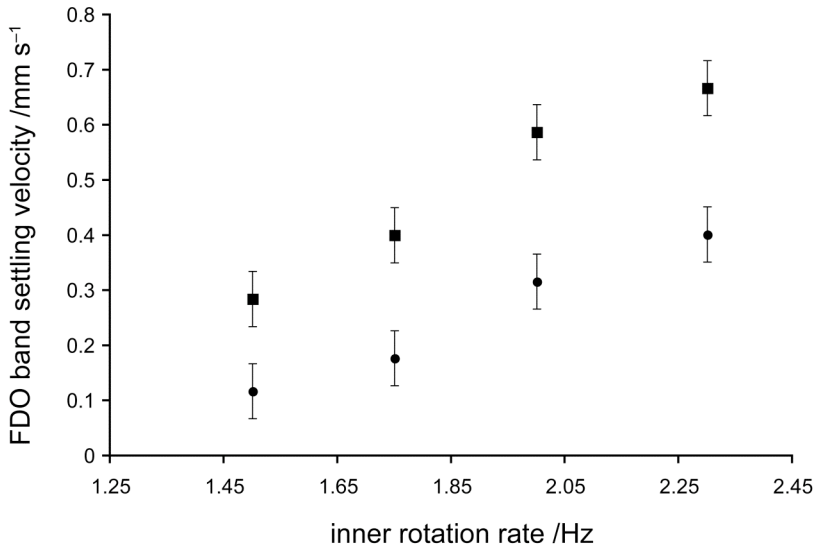

Figure 4.6 A plot to show the velocity of settling FDO bands after formation as a function of inner rotation rate. The circles represent the first wave to settle. The squares show the average velocity of the second and third waves.

The propagation velocity of the first settling FDO band was found to be lower than the subsequent bands in the VFR. This could be due to increased

oxygen dissolution in the reaction solution further up the tube, which could perturb the reaction waves[13]. It has been shown in previous studies that the velocity of travelling waves can change for subsequent waves[15]. This is due to the composition of the reaction changing over time.

The propagation velocity of settling FDO bands throughout the VFR was shown to increase at higher inner rotation rates. This can be explained in terms of increased fluid flow within the vortices, which enhances the transport of chemical waves through the VFR. The maximum velocity within the Taylor vortices in the *z*-direction was plotted out as a function of inner rotation rate in Figure 4.7. The velocity images used for the plot were obtained without superimposed axial flow. The measurements are therefore an approximation, but it can be assumed that the flow within the vortices increased with the inner rotation rate as has been shown for previous VFR investigations[5, 6].

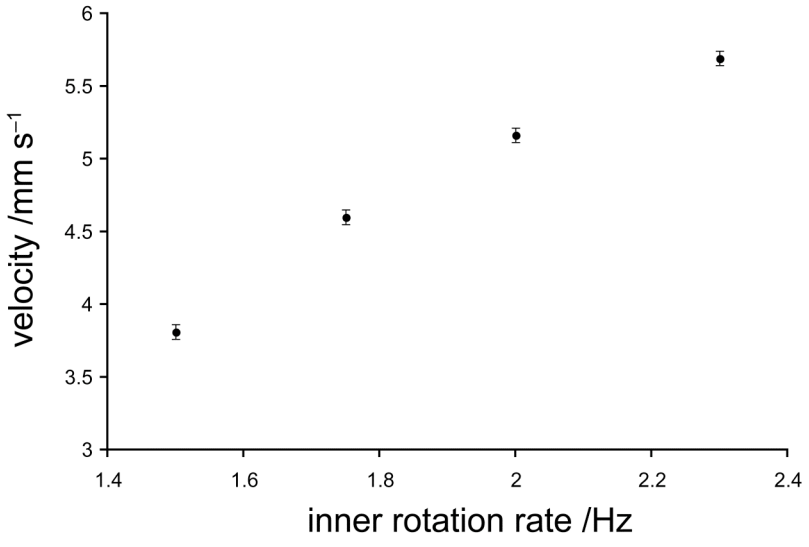

Figure 4.7 Plot showing the maximum measured velocities in the *z*-direction as a function of inner rotation rate. The velocity images were produced in the absence of superimposed axial flow.

The exact mechanism through which the FDO bands propagate when settling cannot be determined using optical imaging. This is due to the optical images showing a projection through the torroidal vortices. To properly characterise the band propagation mechanisms, magnetic resonance images could be acquired of the system. A standard spin echo sequence could be used to obtain vertical slices through the centre of the reactor, from which the propagation mechanism could be elucidated. Regardless of the propagation mechanism, the velocity of the bands would still increase at higher inner rotation rates. The increased flow within the vortices transports the autocatalyst more rapidly. Axial dispersion also increases at higher inner rotation rates[16], which facilitates more rapid transport of the autocatalyst from one vortex to another. These two factors have been shown to enhance the velocity of chemical waves and fronts propagation in both Taylor vortices[17] and planar vortex systems[18, 19].

The by-pass flow seen at higher inner rotation rates could also enhance wave propagation velocities. Giordano *et al.*[5, 6] showed that the drift velocity of the vortices decreased at higher inner rotation rates. It was inferred from this that fluid must pass through or around the vortices. This by-pass flow could increase the propagation velocities of the propagating waves by increasing the axial transport of the autocatalytic species. This phenomenon has not been comprehensively explained in the literature and requires further study, possibly with a suitable NMR velocity imaging technique.

4.3.4. Wavelength of FDO Patterns in a VFR

Previously[3], FDO patterns in a packed bed reactor have been controlled by changing volume flow rates and initial chemical compositions. An increase in the initial concentration of both H^+ and $HBrO_3^-$ were shown to decrease the wavelength of the patterns at higher concentrations. An increase in volume flow rate was shown to monotonically increase the wavelength of FDO patterns. The wavelength of the patterns in the agar system was controlled by both the initial concentration of $HBrO_3^-$ and the global temperature of the reaction tube. The wavelength of patterns in the VFR can be controlled by the parameters previously used to control the wavelength of FDO patterns. In addition to this, the VFR has the unique parameter of the inner rotation rate, which can be used to control the behaviour of the FDO patterns.

Figure 4.8 shows a plot of the relationship between the inner rotation rate and wavelength for stationary FDO patterns in the VFR. The wavelength was measured from the bottom of one band to the bottom of the next. This was then averaged over all bands through the VFR.

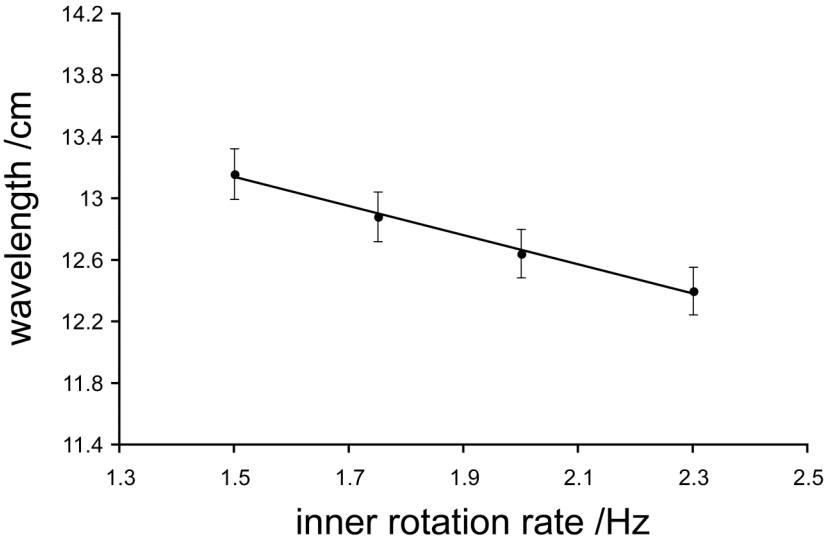

Figure 4.8 A plot of the wavelength of stationary FDO patterns in the VFR as a function of inner rotation rate.

Figure 4.8 shows an inverse relationship between inner rotation rate and wavelength, where higher inner rotation rates resulted in decreased wavelength. The wavelength, λ, of FDO patterns has previously been predicted using eq 4.1, where v is the linear velocity of the fluid and τ is the period between oscillations in the well-stirred reaction. A lower experimental wavelength, compared to the predicted wavelength, has previously been explained by increased axial diffusive mixing[10, 20]. It must be noted that fluid packets in this context are conceptual and must not be confused with the Taylor vortices moving up the reaction tube.

$$\lambda = v\tau \qquad \text{(eq 4.1)}$$

The VFR flow is more complex than the simple plug flow assumed for eq 4.1. At higher inner rotation rates, the flow within the vortices increased[5,

[6]. The axial mixing, associated with the reduced FDO wavelength[20], could be increased by a number of factors at higher inner rotation rates. It was mentioned in section 4.3.3 that increased inner rotation rate stabilised the position of the vortices in the VFR, hence increasing the by-pass flow through or around the vortices. A flow through or around the vortices would increase the axial mixing between fluid packets in different oscillation phases. This would alter the wavelength of the FDO patterns[10]. Transport of the autocatalytic species within the vortices would increase as a function of inner rotation rate, as would the diffusive transport between the vortices[17]. All three of these factors scale with increased inner rotation rate contributing to the reduced FDO wavelength.

4.3.5. Structure of FDO Patterns in a VFR

FDO patterns in the agar system (Chapter 2) were produced in an almost perfect plug flow regime, as shown by the velocity and diffusion measurements. The structure of the patterns remained constant for the duration of the experiments which can be attributed to the flow. The flow within the VFR is more complex than the agar system. This flow directly affects the structure of stationary FDO patterns.

Figure 4.9 shows the typical behaviour of one stationary concentration band over time. The image sequence shows the pattern is virtually stationary over time. However, the band deviated axially by ±1 cm. In conjunction with the axial translation of the bands, the size of the band is not fixed over time. For example, the first image shows the band to be roughly twice as long as the second image.

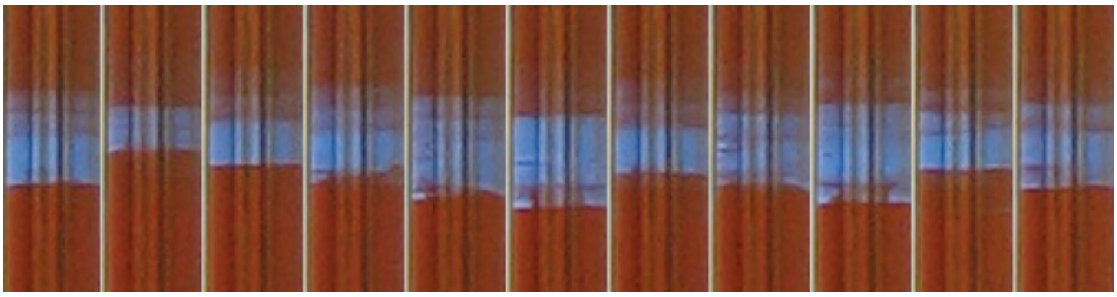

Figure 4.9 A series of optical images showing the dynamic behaviour of a single FDO band over time. Images were acquired sequentially in less than a second with a delay of twenty seconds between acquisitions.

The change in size and position of the bands can be explained by the coupling of the reaction-diffusion chemistry to the flow within the VFR. The FDO band propagated downwards into the vortex cell beneath by diffusion across the separatrix. This newly contaminated vortex cell is then translated upwards by the axial flow. This process occurs continually with the downwardly propagating reaction-diffusion-advection wave in balance with the axial flow up the tube, which produced a band that is close to maintaining a stationary position. The propagation mechanism results in a discrete system where a vortex cell either has ferriin within it, or not. Optical images show the stationary band at different stages of the reaction, where the smaller bands are in a timeframe just before the ferriin is going to enter the next cell. The images with the larger band show the band when the ferriin is in multiple cells. For the same reason the band appears to be translating axially from one image to the next. This can be compared to the agar system where a reaction-diffusion wave is in competition with the axial plug flow which produces a wave which remains stationary.

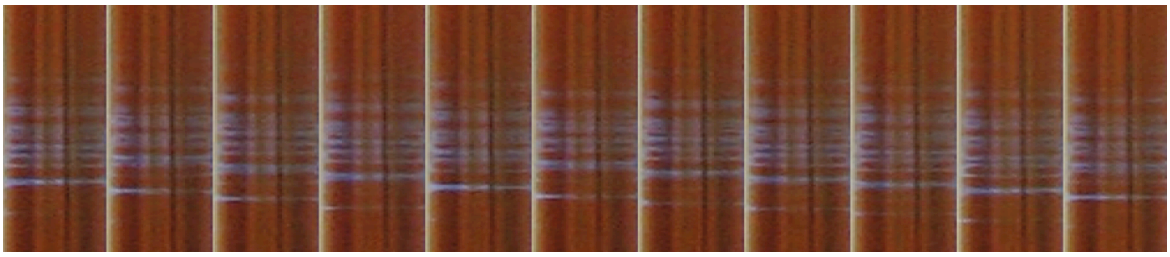

Figure 4.10 A time series of optical images of the second stationary FDO pattern shown in Figure 4.3. Images were acquired sequentially in less than a second with a delay of twenty seconds between acquisitions.

The second stationary FDO band, shown in Figure 4.3 had a different structure to the other bands through the reaction tube. A close-up of this band is shown in Figure 4.10. The band was approximately 5 cm in length compared to the 1-2 cm length of other bands in the reaction tube. The band appears diffuse due to the presence of ferriin and ferroin over a number of vortices.

The second pattern was the only pattern in the VFR to show this type of structure. At higher inner rotation rates, the band was more defined and resembled the patterns observed further up the tube. No abnormal behaviour was observed in the well-stirred reactions or in the packed bed or agar systems to indicate that the chemistry would be responsible for the nature of the second pattern. These two factors indicated the flow within the VFR was responsible for the structure of this pattern. The diffuse pattern is spread over a number of vortex cells, indicative of increased mixing between the cells. This could be due to the flow within the VFR, which is not confined to the vortices. At the lower rotation rates, the vortices may not be fully formed at the bottom of the reactor due to the fluid inflow[5]. These vortices could be

stabilised at higher inner rotation rates. The flow at this position of the VFR needs to be verified at different rotation rates to confirm this hypothesis.

4.3.6. Stability of FDO Patterns in a VFR

The stability of FDO patterns in a packed bed reactor has been investigated previously as a function of volume flow rate[21]. Zigzag patterns and travelling waves were produced at lower flow rates. This was attributed to the magnitude of diffusive and advective transport processes becoming comparable at lower volume flow rates.

FDO patterns in the VFR were shown to be stable for a specific range of parameters. These parameters included the initial chemical concentrations and the volume flow rate of the reaction solution through the VFR. Uniquely in the VFR experiments, the stationary FDO patterns were found to be stable for only a narrow range of inner rotation rates at the volume flow rates studied.

Figure 4.11 shows a situation where FDO patterns fail to settle at the steady-state position. For example, the fourth pattern spontaneously disappeared prior to settling at the steady-state wavelength. A similar disappearance is observed twice for the fifth pattern at 2500 s and 3000 s. The stability of the FDO patterns in a VFR was found to be dependent on the rotation rate of the inner cylinder, where at higher inner rotation rates, the patterns do not consistently settle to the equilibrium positions.

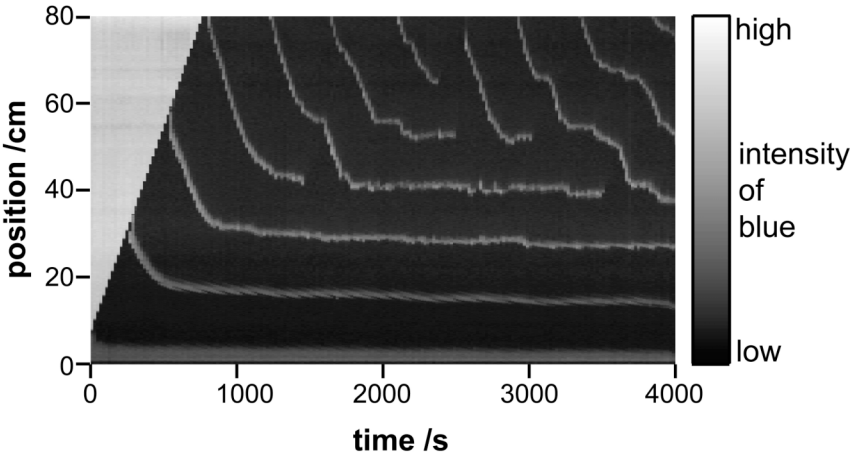

Figure 4.11 A space-time plot of FDO patterns in a VFR. The inner rotation rate was 2.3 Hz.

The annihilation of FDO bands has been modelled previously for the BZ reaction in a plug flow reactor by Bamforth *et al*[3]. They describe a situation in which a stationary pattern, below a settling pattern, moves upwards slightly prior to the settling of the wave. As a result of the jump, the settling band overshoots the equilibrium position. Because of this overshoot, the fluid packet where the band was settling to, is still in the refractory state of oscillation and is therefore unable to switch state[22]. With the fluid packet unable to switch state, the settling band disappears.

The extinguishing of settling patterns can possibly be explained in the same terms as those explained in the Bamforth paper[3]. As explained above, and shown in Figure 4.9, the FDO bands in the VFR have a positional variance of ± 1 cm. This variance could lead to a wavelength that is significantly different than the steady-state wavelength. Consider a hypothetical situation, where the steady-state wavelength of the FDO patterns is 13 cm. If a lower band moves 1 cm up and the band above moves 1 cm down, the wavelength would be 11 cm, 2 cm shorter than the steady-state

wavelength. This reduction in wavelength could result in the extinguishing of the above band as the reaction solution would still be in the refractory state of oscillation and would be unable to switch state. This phenomenon would be enhanced at higher inner rotation rates where the wavelength is shorter (section 4.3.4). Multiple experiments have been conducted at different flow and rotation rates which show the stability of the patterns decreased when the wavelength is shorter. This indicated FDO patterns with a shorter wavelength were perturbed more than ones with a longer wavelength.

When a pattern fails to stabilise into a stationary pattern, the system responds to compensate. The wave directly above, travels downwards to replace the extinguished pattern. This process occurs rapidly so the steady-state wavelength is maintained.

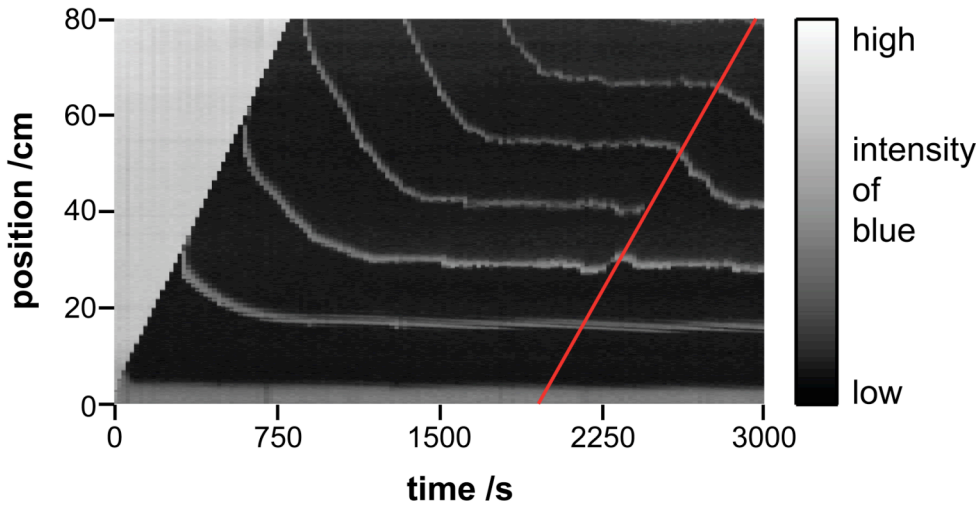

Figure 4.12 A space-time plot of FDO patterns in a VFR. The section from 0 to 800 seconds shows the VFR filling up with reactants. The inner rotation rate was 1.75 Hz. The plot has been annotated with a red line indicating the linear velocity of one fluid moving up the reaction tube.

An example of the annihilation of a pattern is shown in the space-time plot in Figure 4.12. The plot has been annotated with a single diagonal red line to show the velocity of one fluid packet (conceptual not a Taylor vortex) translating up the VFR. The third pattern, positioned at 28 cm, inexplicably moved down slightly down at 2100 s for 60 s. This pattern proceeded to rapidly jump 2 cm above the steady-state position at 2250 s. Following the jump in position, the fluid packet travelled up the tube. When this fluid packet reached the next wave, the band disappeared. The above pattern had previously responded to the drop in position of the lower band by moving lower than the steady-state position. This annihilation occurred because the fluid packet was still in the refractory state and was unable to switch state. The response of the system to the spontaneous disappearance of the pattern was also a function of the fluid packet velocity. At 2750 s, the fifth pattern responded to the disappearance of the fourth by descending to the steady-state position previously occupied by the fourth. This band moved downwards because the reaction solution below was no longer in the refractory state and could propagate down unhindered.

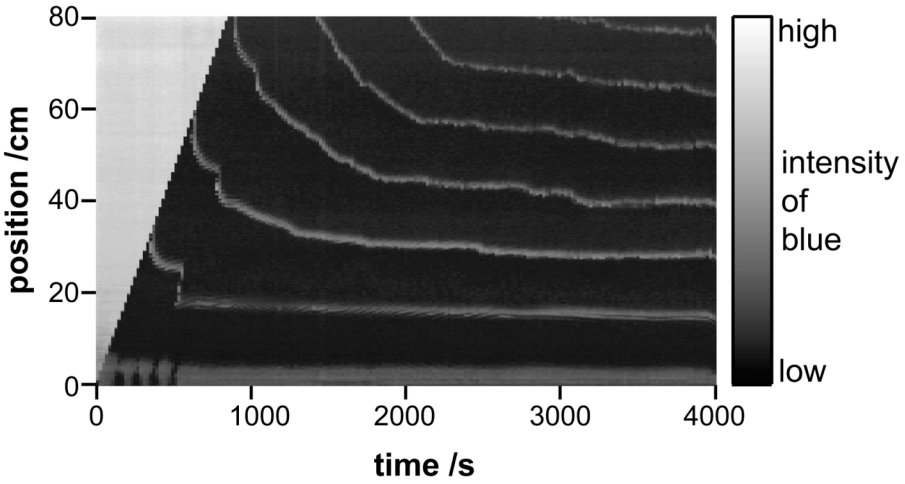

Figure 4.13 A space-time plot for the ferroin-catalysed BZ reaction in a VFR. The rotation rate of the inner cylinder was 1.25 Hz.

Chemical bands in a VFR at a rotation rate of 1.25 Hz are shown in Figure 4.13. The FDO patterns at this rotation rate did not attain a steady-state position. NMR velocity and diffusion images showed that Taylor vortices could be produced at an inner rotation rate of 1.25 Hz. However, the superimposed axial flow increases the critical inner rotation rate required for the onset of steady Taylor vortex flow[5]. Therefore, the non-settling bands at 1.25 Hz may have been due to vortices that have not fully formed. Vortices that are not fully formed could result in increased by-pass flow. This axial mixing (non plug flow) could result in bands which do not settle on the timescale of the experiment. No literature on the VFR flow prior to the onset of steady Taylor vortices in the VFR could be found.

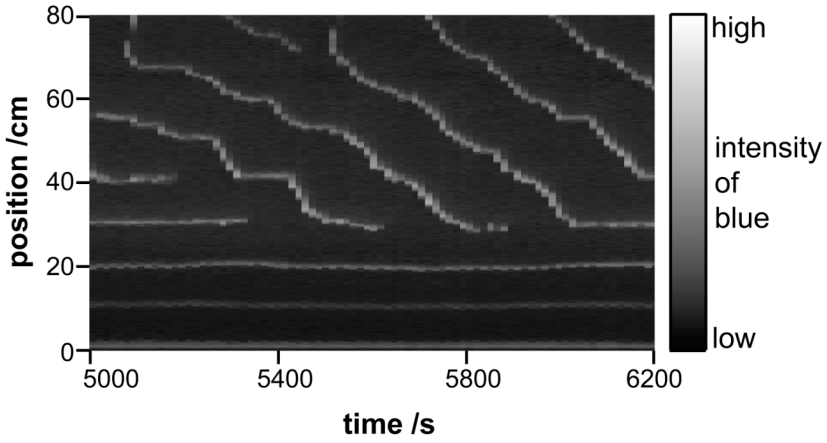

Figure 4.14 A space-time plot for the ferroin-catalysed BZ reaction in a VFR. The rotation rate of the inner cylinder was 2.3 Hz. The flow rate was 10 cm^3 min^{-1}.

At a rotation rate of 2.3 Hz and a volume flow rate of 10 cm^3 min^{-1}, a mixture of stationary and travelling waves were produced. A space-time plot for the flow-distributed structures produced under these conditions is shown in Figure 4.14. These patterns can be explained by increased mixing, due to both enhanced diffusion coefficients and fluid velocity. By-pass flow would also increase at higher inner rotation rates, again increasing the degree of axial mixing. Behaviour of this type has been shown previously in the packed bed reactor at low fluid flow rates, where axial diffuse effects become comparable to the linear velocity of the fluid[21].

4.3.7. The Manganese-Catalysed BZ Reaction in a VFR

Optical imaging is unable to probe the propagation of waves through the Taylor vortices in the VFR flow. However, MRI is able to produce images of propagating waves though Taylor vortices using the manganese-catalysed BZ reaction[17]. The development of a suitable manganese-catalysed system

would enable further investigation into the structure and dynamics of FDO patterns in a VFR using MRI.

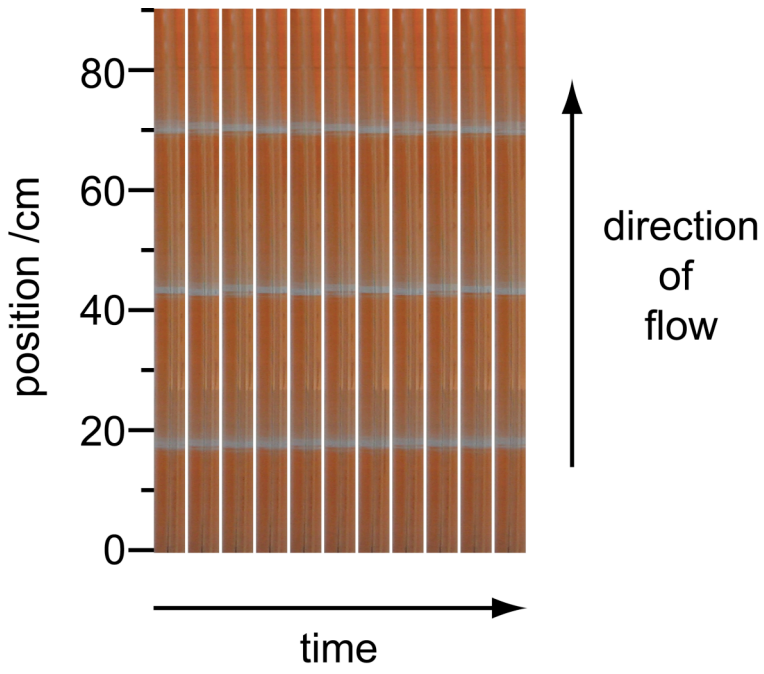

Figure 4.15 A series of optical images showing chemical bands in a VFR using the manganese-catalysed BZ reaction. Images were acquired sequentially with a delay of twenty seconds between acquisitions. A small amount of ferroin has been added to the reaction to enhance the colour contrast. The rotation rate of the inner cylinder was 1.5 Hz.

Figure 4.15 shows a series of optical images of chemical bands in a VFR produced with the manganese-catalysed BZ reaction[23]. The patterns could not be visualised using optical imaging. This is due to the poor optical contrast associated with the manganese-catalysed BZ reaction. To combat this, a small amount of ferroin was been added to the reaction to enhance the optical contrast. Strictly speaking it is not a pure manganese-catalysed reaction but provides a reasonable approximation of the wavelength of the patterns. The optical images show three distinct concentration bands in the

VFR. The lowest is found at 18 cm with two more found at 43 and 70 cm. The images show that the bands are periodic through space and remain stationary through time. This showed that stationary concentration bands could be produced in the VFR using the manganese-catalysed BZ reaction.

For the manganese-catalysed reaction, phosphate-containing compounds have previously been added to the reaction[24] in order to improve MRI contrast [2, 24, 25]. The phosphate compounds act to stabilise the oxidation states of the manganese catalyst. However, because of the complexation, the addition of phosphates to the reaction mixture is potentially detrimental for FDO pattern production. This is due to a lengthening of the induction and oscillation periods[24]. For example, the period with no phosphate compound was 250 s, with 0.001 M was 450 s and with 0.01 M was 900 s. Due to the increased period between oscillations, the manganese-catalysed BZ reaction used in Figure 4.15 was run at a significantly lower volume flow rate than the ferroin-catalysed BZ reaction (12 cm^3 min^{-1} for ferroin and 4 cm^3 min^{-1} for manganese).

4.4. Conclusions

Chemical patterns were investigated in a vortex flow reactor (VFR) in the steady vortex regime for the first time. Optical images of these patterns were acquired over time to investigate the structure and dynamics of the patterns. Within a certain range of inner rotation rates (1.5 - 2.3 Hz), stationary FDO patterns were produced. The overall position of the bands was stationary over time. However, the position of the band was shown to fluctuate over time. This deviation was due to the propagation of the bands

through the translating vortices, which was in stark contrast to the agar system where a reaction diffusion wave propagates against a plug flow.

The wavelength of the patterns could be controlled by the inner rotation rate, which is an additional control parameter compared to the agar or packed bed systems. It was found that the wavelength of the FDO patterns decreased with increased inner rotation rate. This was due to the flow and dispersion, which was shown by velocity and diffusion imaging to increase at higher inner rotation rates. This result implied greater axial mixing between the vortices. Enhanced inter-vortex mixing may also occur at higher rotation rates due to increased by-pass flow through or around the vortices. This could possibly to be shown by a suitable NMR velocity imaging experiment.

Outside the range of stable FDO patterns, travelling and unstable waves were produced. At a rotation rate of 1.25 Hz, the FDO patterns did not settle, which was hypothesised to be a result of unstable vortices. Unstable vortices could increase axial mixing, but this needs to be investigated further. Unstable and travelling waves were observed at higher rotation rates, particularly at 2.3 Hz, where the reduced wavelength made patterns more susceptible to annihilation.

A manganese-catalysed FDO system was developed for the investigation of chemical patterns in the VFR. It was found that stationary FDO patterns could be produced, which provide a starting point for future magnetic resonance investigations of the patterns within the system.

4.5. References

[1] M. Kaern, M. Menzinger, *Physical Review E* **1999**, *60*, R3471.

[2] M. M. Britton, A. J. Sederman, A. F. Taylor, S. K. Scott, L. F. Gladden, *Journal Of Physical Chemistry A* **2005**, *109*, 8306.

[3] J. R. Bamforth, R. Toth, V. Gaspar, S. K. Scott, *Physical Chemistry Chemical Physics* **2002**, *4*, 1299.

[4] K. Kataoka, Doi, H., Komai, T., Futagawa, M., *Journal of Chemical Engineering Japan* **1975**, *8*, 472.

[5] R. C. Giordano, R. L. C. Giordano, D. M. F. Prazeres, C. L. Cooney, *Chemical Engineering Science* **1998**, *53*, 3635.

[6] R. L. C. Giordano, R. C. Giordano, D. M. F. Prazeres, C. L. Cooney, *Chemical Engineering Science* **2000**, *55*, 3611.

[7] S. T. Wereley, R. M. Lueptow, *Physics of Fluids* **1999**, *11*, 3637.

[8] R. M. Lueptow, A. Docter, K. Y. Min, *Physics of Fluids a-Fluid Dynamics* **1992**, *4*, 2446.

[9] N. Ohmura, K. Kataoka, M. Utsunomiya, D. Shindo, T. Mukaida, S. Deki, *Journal of Chemical Engineering of Japan* **1997**, *30*, 388.

[10] P. N. McGraw, M. Menzinger, *Physical Review E* **2003**, *68*.

[11] A. Taylor, *Advances In Complex Systems* **2003**, *6*, 155.

[12] J. A. Pojman, H. Dedeaux, D. Fortenberry, *Journal of Physical Chemistry* **1992**, *96*, 7331.

[13] O. Steinbock, C. T. Hamik, B. Steinbock, *Journal of Physical Chemistry A* **2000**, *104*, 6411.

[14] P. Ruoff, *Chemical Physics Letters* **1982**, *92*, 239.

[15] M. M. Britton, *Journal Of Physical Chemistry A* **2006**, *110*, 5075.

[16] O. Richter, H. Hoffmann, B. Kraushaar-Czarnetzki, *Chemical Engineering Science* **2008**, *63*, 3504.

[17] B. W. Thompson, J. Novak, M. C. T. Wilson, M. M. Britton, A. F. Taylor, *Physical Review E* **2010**, *81*.

[18] M. S. Paoletti, T. H. Solomon, *Physical Review E* **2005**, *72*.

[19] A. Pocheau, F. Harambat, *Physical Review E* **2008**, *77*.

[20] P. Andresen, E. Mosekilde, G. Dewel, P. Borckmans, *Physical Review E* **2000**, *62*, 2992.

[21] A. F. Taylor, J. R. Bamforth, P. Bardsley, *Physical Chemistry Chemical Physics* **2002**, *4*, 5640.

[22] P. Ball, *The self-made tapestry : pattern formation in nature*, Oxford University Press, Oxford [England] ; New York, **1999**.

[23] E. W. Hansen, P. Ruoff, *Journal of Physical Chemistry* **1989**, *93*, 264.

[24] A. Cross, The University of New Brunswick (New Brunswick), **1998**.

[25] A. R. Cross, R. L. Armstrong, A. Reid, S. Y. Su, M. Menzinger, *Journal of Physical Chemistry* **1995**, *99*, 16616.

5. Chapter 5 Concluding Remarks

5.1. Conclusions

The research presented in this thesis used a combination of optical and magnetic resonance imaging techniques to characterise novel reaction-diffusion-advection systems. The results presented here have provided greater insight into the coupling between the BZ reaction and flow.

Flow-distributed oscillation (FDO) patterns were investigated in pipe flow and two alternative plug-like flow fields for the first time. A system was developed where agar gel was added to the ferroin-catalysed BZ reaction. This mixture was passed into a pipe reactor and subsequently formed a gel. The addition of agar induced a plug-like flow, which was verified using magnetic resonance velocity imaging. Stationary FDO patterns were produced in this system via the wavesplitting mechanism previously observed in the packed bed reactor. The optical transparency of the agar allowed the structure of the waves to be determined, which was not possible in the packed bed system. However, unlike bands in the packed bed reactor, the intensity of the bands decreased further up the tube which was attributed to agar adhering to the inside of the reaction tube.

It was found that temperature could be used as a forcing parameter for FDO patterns in the agar system. Synchronous behaviour was observed between the position of the chemical waves and the periodic change in reaction tube temperature. In contrast to previous systems, for example periodic illumination, it was found that the temperature forcing produced

synchronisation in space-time but not time. The lack of entrainment in space-time was attributed to the complicated kinetics of the BZ reaction, where the rate constants and activation energies of all reaction steps are affected by temperature.

The requirement of plug flow for the formation of FDO patterns was tested in experiments using no packing material or gelling agent. A single pattern was observed in this Poiseuille flow system at the bottom of the reactor and an unstable second pattern was observed further up the reaction tube. Kaern and Menzinger had previously reported the pattern at the bottom of the reactor but there was no mention of the second band in the study.

Stationary FDO patterns were produced in a vortex flow reactor (VFR) for the first time. A superimposed axial flow in this system forces Taylor vortices to translate up the reaction tube in an approximation of plug flow. The production of stationary bands in the VFR system demonstrated the robustness of FDO patterns to complex flow fields. The bands in the VFR were formed via a non-wavesplitting mechanism, which can possibly be explained by oxygen inhibition, not found in the packed bed reactor or the agar system. A unique control parameter for this system was the rotation rate of the inner cylinder, which was able to control both the stability and wavelength of the patterns. Stationary FDO patterns were formed within a certain range of inner rotation rates (1.5 - 2.3 Hz), outside of which travelling and unstable waves were produced. It was found at an inner rotation rate of 1.25 Hz, bands did not settle to a steady-state wavelength which could possibly be explained by unstable vortices produced at this rotation rate. The

patterns were also less stable at the higher inner rotation rates which was explained by an increase in axial mixing.

Travelling chemical waves in Taylor vortices were investigated for the first time using the manganese and ferroin-catalysed BZ reaction. Optical imaging of the ferroin-catalysed BZ reaction was able to probe the macroscopic behaviour but was unable visualise the microscopic structure of the waves. Magnetic Resonance imaging (MRI) was able to excite a vertical slice through the Couette cell in order to visualise waves in the manganese-catalysed BZ reaction through the torroidal vortices. Distributed reaction fronts were the most commonly observed propagation behaviour. This involved the rapid propagation of reaction waves around the perimeter of a vortex followed by a slower diffusion of the autocatalytic species across the boundary between the vortices. Different propagation behaviour was also observed in the system including wrinkled fronts and flamelets which have been shown previously for modelled systems. This work represents the first investigation of propagating waves through a three-dimensional vortex system.

5.2. Future Work

There has been increased interest between the coupling of reaction-diffusion chemistry to flow. A combination of magnetic resonance and optical imaging techniques provide the opportunity to quantitatively study both processes in order gain further control over pattern formation.

There remain many questions with regards to the study of travelling waves through Taylor vortices. The first lies in the mechanisms that

determine the way BZ waves propagate through the vortices. Wave propagation velocities can be altered by changes in the initial chemical concentrations, which would provide greater insight into the coupling between reaction-diffusion and flow. Altering the size ratio between the inner and outer cylinders would change both the aspect ratio and flow within the vortices.

Stationary FDO patterns were produced in a VFR for the first time. At first this may seem surprising due to the complexity of the flow within the VFR which is still poorly understood. The patterns produced were sensitive to both volume flow rates and inner rotation rates. Understanding how these parameters change the flow environment is key to understanding FDO formation in the VFR. More work is required to probe the flow within the VFR. It has been shown in previous studies that the drift velocity of the vortices can be reduced at higher inner rotation rates. A suitable NMR velocity imaging technique could possibly quantify the precise mechanism through which the fluid passes through or around the vortices when the drift velocity is reduced. A more complete knowledge of the flow field would allow the axial dispersion to be related to the stability of the FDO patterns produced in the VFR.

The further development of a suitable manganese-catalysed BZ reaction for the production of stationary FDO patterns in the VFR would enable more detailed visualisation of patterns using magnetic resonance imaging. These experiments would provide further insight into the mechanism through which the FDO patterns remain stationary, which cannot be confirmed by optical imaging. A study involving the change in the volume flow rate, inner rotation rates and different vortex sizes (with different VFRs) could then

be conducted to further understand the coupling of the FDO system to the flow.

The study of non-linear chemical systems within the VFR could be further expanded due to the wide range of flow regimes are accessible e.g. helical and stationary vortices. The coupling of pattern-producing chemistry to flow fields of this type could produce interesting and possibly novel pattern formation.

The development of a second pattern further up the tube in the Poiseuille flow experiments asks the question: is it possible to produce stationary patterns in the absence of plug flow? This second pattern was highly unstable and was destroyed almost immediately. However, it may be possible to stabilise this band somehow. A perturbation to the flow field at the point where the second pattern is produced could possibly create a flow field, which may result in greater longevity of the second band.

5.3. Posters, Talks, Publications and Prizes

5.3.1. Posters

1. *Temperature Forcing of Flow-Distributed Oscillations*, Postgraduate Symposium 2008, School of Chemistry, University of Birmingham, UK.

2. *Temperature Forcing of Flow-Distributed Oscillations*, Oscillations and Dynamic Instabilities in Chemical Systems 2008, Gordon Research Conferences, Colby College, Waterville, Maine, USA.

3. *Visualisation of Chemistry in Flow*, Graduate School Poster Competition 2008, University of Birmingham, UK.

4. *Magnetic Resonance Imaging of Chemistry in Flow*, College Research Conference, College of Engineering and Physical Sciences 2009, University of Birmingham, UK.

5. *Magnetic Resonance Imaging of Chemistry in Flow*, International Conference on Magnetic Resonance Microscopy 2009, University of Montana, Yellowstone Park, Montana, USA.

5.3.2. Talks

1. *Visualisation of Chemistry in Flow*, Postgraduate Symposium 2009, School of Chemistry, University of Birmingham, Birmingham, UK.

2. Magnetic Resonance Imaging of Chemistry in Flow, NMR Discussion Group Postgraduate Meeting 2010, University of Leeds, UK.

5.3.3. Publications

1. B. W. Thompson, J. Novak, M. C. T. Wilson, M. M. Britton, A. F. Taylor, *Physical Review E* **2010**, *81*.

2. 'Temperature Forcing of Flow-Distributed Oscillations', Novak J.; Thompson B.W.; Wilson M.C.T.; Taylor A.F.; Britton M.M., *In preparation.*

3. 'Flow Distributed Oscillations in a Vortex-Flow Reactor', Novak J.; Thompson B.W.; Wilson M.C.T.; Taylor A.F.; Britton M.M., *In preparation.*

4. 'Chemical Waves Propagating Through Taylor Vortices', Novak J.; Thompson B.W.; Wilson M.C.T.; Taylor A.F.; Britton M.M., *In preparation.*

5.3.4. Prizes Awarded

1. First Prize in the postgraduate poster competition, College of Engineering and Physical Sciences Conference 2009, University of Birmingham, Birmingham, UK.

2. Third prize in the postgraduate symposium talk competition, 2009, School of Chemistry, University of Birmingham, Birmingham, UK.

3. Best oral presentation, NMR Discussion Group Postgraduate Meeting 2010, University of Leeds, UK.